Architecture of the neutrophil compartment

https://doi.org/10.1038/s41586-025-09807-0

Received: 16 August 2024

Accepted: 24 October 2025

Published online: 3 December 2025

Open access

Check for updates

Daniela Cerezo-Wallis[1,2,29], Andrea Rubio-Ponce[1,2,29], Mathis Richter[3], Emanuele Pitino[4], Immanuel Kwok[5], Giovanni Marteletto[1], Ana Cristina Guanolema-Coba[2], Changming Shih[6], Run-Kai Huang[6], Ana Moraga[2,7], Natalia Borbaran Bravo[8], Samuel Doré[9], Sergio Callejas[2], David G. Aragonés[10], Daniel Jiménez-Carretero[2], Daniel Martin[2], Samuel Ovadia[1], Tommaso Vicanolo[2], Georgiana Crainiciuc[2], Jon Sicilia[2], Tong Deng[1], Anjelica Martin[1], Jing Zhang[11], Maria Isabel Cuartero[2,12], Diego Moncada Giraldo[13], Alicia Garcia-Culebras[2,7], Alejandra Aroca-Crevillen[2], Sandra Martín-Salamanca[2], Carlos Torroja[2], Max Ruiz[4], Irene Ruano[4], Melissa S. F. Ng[5], Jian Hou[14], You Wang[15,16], Ming Zhang[17], Jun Pu[18], Ana Herruzo[19], David Chang van Oordt[20], Seokyoon Chang[20], Alexander E. Downie[20], Fei Chen[21], Andrea L. Graham[20], William C. Gause[21], Pierre O. Fiset[22], Jonathan D. Spicer[23], Holger Heyn[4,24], Maria A. Zuriaga[2], Juan A. Bernal[2], Irina A. Udalova[25], Maria A. Moro[2], Katrien de Bock[11], Ana Dopazo[2], Jose J. Fuster[2,26], Fátima Sánchez-Cabo[2], Juan C. Nieto[4], Gabriel F. Calvo[10], Julia Skokowa[8], Oliver Soehnlein[3], Daniela F. Quail[9], Logan A. Walsh[8], Lai Guan Ng[6,27,30] ✉, Andrés Hidalgo[1,2,30] ✉ & Iván Ballesteros[2,28,30] ✉

Neutrophils exhibit remarkable phenotypic and functional diversity across tissues and diseases[1,2], yet the lack of understanding of how this immune compartment is globally organized challenges translation to the clinic. Here we performed single-cell transcriptional profiling of neutrophils spanning 47 anatomical, physiological and pathological scenarios to generate an integrated map of the global neutrophil compartment in mice, which we refer to as NeuMap. NeuMap integrates and expands existing models[3,4] to generate fundamental new insights; it reveals that neutrophils organize in a finite number of functional hubs that distribute sequentially during maturation to then branch out into interferon-responsive and immunosuppressive states, as well as a functionally silent state that dominates in the healthy circulation. Computational modelling and timestamp analyses identify prototypical trajectories that connect these hubs, and reveal that the dynamics and preferred paths vary during health, inflammation and cancer. We show that TGFβ, IFNβ and GM-CSF push neutrophils along the different trajectories, and projection of chromatin accessibility sites onto NeuMap reveals that the transcription factor JUNB controls angiogenic and immunosuppressive states and promotes tissue revascularization. The architecture of NeuMap appears to be conserved across sex, environmental and genetic backgrounds, as well as in humans. Finally, we show that NeuMap enables inference of the pathophysiological state of the host by profiling blood neutrophils. Our study delineates the global architecture of the neutrophil compartment and establishes a framework for exploration and exploitation of neutrophil biology.

Millions of neutrophils are produced every day by the bone marrow through a well-defined series of differentiation steps before their release into the circulation as terminally differentiated, non-proliferative cells that eventually infiltrate most tissues[5,6]. Work over the past decade has unveiled substantial heterogeneity of neutrophils and delineated a vast array of transcriptional and phenotypic states, of which only a few have been assigned functional roles[2]. Paradoxically, the fundamental organization of the neutrophil compartment remains uncharacterized, a limitation that hinders their functional classification, knowledge of their physiological relevance, and clinical value.

Previous efforts to define the transcriptional organization of this compartment has reported linear trajectories when profiling neutrophils from the bone marrow, spleen, blood and inflamed tissues, and suggested active reprogramming of granulopoiesis by disease[7,8]. It is unlikely, however, that these profiles encompass the entire transcriptional diversity of neutrophils, given the vast variety of microenvironments, infectious agents and malignant cells that inhabit or invade mammalian tissues, their transcriptional plasticity, and the wealth of functional states already identified across healthy and disease conditions[2]. Thus, fundamental questions remain about the following: (1) the actual number of possible transcriptional and functional states that neutrophils can acquire; (2) how these phenotypic states relate to each other; (3) the specific stage(s) that are reprogrammed by disease; and (4) the signalling and transcriptional programmes that instruct the diversity of neutrophils in living tissues. We posited that understanding the global architecture of the neutrophil compartment might provide

---

A list of affiliations appears at the end of the paper.

insights into these unknowns and facilitate the conversion of this phenomenal army of cells into therapeutic allies.

Transcriptional cartography of neutrophils

To generate a comprehensive transcriptional map of neutrophil diversity in C57BL/6J mice, we conducted single-cell RNA sequencing (scRNA-seq) of lineage-negative (B220, CD3, CD19, NK1.1, Ter119) cells isolated from the bone marrow and CD11b$^+$LY6G$^+$ cells obtained from 13 tissues of C57BL/6J mice housed in specific pathogen-free conditions at different developmental stages, sex, age and pathological perturbations (Fig. 1a, Extended Data Fig. 1a, Supplementary Fig. 1 and Supplementary Table 1). We used the BD Rhapsody platform[9] and included blood from healthy adult male mice as an internal reference to assess integration quality and control for batch effects across datasets (Methods). We then applied dimensionality reduction techniques to visualize the transcriptional diversity of 129,829 neutrophils collected across 47 biological conditions (Fig. 1a and Extended Data Fig. 1b).

The resulting transcriptome embedding, which we refer to as a NeuMap (Fig. 1a,b), enabled visualization of the transcriptional space of the entire neutrophil compartment and revealed general properties by examining its topology. For example, granulopoiesis was identifiable as a linear structure spanning genes associated with proliferation, maturation and granule formation[3,10] (Fig. 1c and Extended Data Fig. 1c,d) that was enriched in neutrophils from the bone marrow and spleen (Fig. 1b and Extended Data Fig. 1e). The transcriptional map expanded and lost its linear topology as we incorporated neutrophils from healthy peripheral tissues (blood, lung, liver and intestine) and a broad set of pathological conditions (Extended Data Fig. 1b). Finally, this map converged in a defined end structure featuring programmes associated with hypoxia and cancer (Fig. 1c), without generating transcriptional areas that are separated from the main body of the map. NeuMap also revealed a separate path connecting the initial and end states that was independent of the main granulopoietic path and was abundant in the lungs and inflamed tissues (Fig. 1b and Extended Data Fig. 1e). The integration of all neutrophils in a single, interconnected structure is consistent with the constant production and maturation of neutrophils[11] and suggests that most transcriptional programmes are accessible by neutrophils emanating from the granulopoietic programme.

We found that the anatomical and pathophysiological context (including age and sex) dictated the distribution of cells in different regions of NeuMap (Fig. 1b,d and Extended Data Fig. 1e–g). These distributions were also consistent with those obtained by mapping neutrophils from existing datasets of healthy and tumour-bearing mice onto NeuMap[3,4,12] (Extended Data Fig. 1h). Finally, this 'cartographic' inspection of NeuMap revealed that neutrophils from healthy individuals were sufficiently diverse to build the general scaffold of NeuMap, whereas those from inflammatory or tumoural conditions extend from these homeostatic states rather than creating new programmes (Extended Data Fig. 1b).

By scoring NeuMap cells against various gene signatures, we identified physiologically relevant regions within the NeuMap embedding (Fig. 1c, Extended Data Fig. 2a and Supplementary Table 2), including the proliferative and granule-synthesis regions described above, distinct metabolic states (oxidative phosphorylation, hypoxia and glycolysis), chemotactic and antimicrobial functions, antiviral responses and signatures associated with cancer, which overlapped with areas of predicted immunosuppression and angiogenesis (Fig. 1c and Extended Data Fig. 2a).

To define functional regions more precisely, we performed unbiased clustering (Extended Data Fig. 2b–e) and optimal grouping of clusters and functional signatures. We identified seven distinct transcriptional regions, or hubs, distributed in NeuMap (Fig. 1e and Extended Data Fig. 2f), which we interpreted as predictive of the main functional states of neutrophils in health, inflammation, infection and cancer. These hubs included the following: (1) pre-neutrophil (PreNeu)-like neutrophils[10,13], defined by expression of *mKi67* and *Ltf*, and oxidative respiration[14,15] (Supplementary Table 3); (2) an 'immature hub' undergoing active maturation and granule synthesis that was positive for *Mmp8* and *Cebpe*, a regulator of granule synthesis[10,16]; (3) *Cd52*+ neutrophils that lacked a distinct transcriptional signature, had low mRNA content (Extended Data Fig. 2a), and were enriched in blood (immuno-silent hub); (4) a conspicuous interferon-response signature (IFN-response hub) marked by expression of *Ifit1* and *Cd274*, which featured signatures of antiviral response (Fig. 1c) and was similar to the G5b state reported in mice and humans during infection[3] (Extended Data Fig. 1h); (5) and (6) hubs that shared signatures associated with immunosuppression and angiogenesis—one featured expression of *Cd14* and *Ptgs2* and was typical of lung and liver neutrophils[1] (immunosuppression I hub (IS-I)), and the other expressed high levels of *Vegfa* and *Cd274* and was prominent in tumoural neutrophils (immunosuppression II hub (IS-II)); and (7) a final hub (antigen (Ag) presentation hub) featuring increased expression of genes associated with MHCII (*H2* and *Cd74*), reminiscent of neutrophils reported to mediate antigen presentation[1,17,18], connected the PreNeu and IS-I hubs (Fig. 1e), and is not explored further here. Neutrophils from different tissues or pathophysiological conditions were associated with the different functional hubs (Fig. 1f). For example, *Cd14*+*Ptgs2*+ IS-I neutrophils were abundant in the gut, liver and lungs, interferon-responsive neutrophils dominated in infected, inflamed and ischaemic conditions irrespective of the tissue, and *Cd274*+ and *Vegfa*+ IS-II neutrophils were prominent in tumours but were largely absent from healthy tissues (Fig. 1e,f and Extended Data Fig. 2f–h).

By analysing multiple other conditions, we found that the basic structure of NeuMap in defined hubs was conserved across relevant biological variables, including sex, housing conditions and genetic strains (Balb/c), and in the presence of *Tet2*-associated clonal haematopoiesis[19], both at baseline and during atherosclerosis (Extended Data Fig. 3a–e). Profiling of neutrophils from 10 human tissues, including samples from healthy individuals, colorectal cancer and blood from a patient with systemic lupus (Supplementary Table 4 and Supplementary Fig. 2), also revealed substantial conservation of the transcriptional structure of the neutrophil compartment in humans (Extended Data Fig. 4a,b). We could identify six hubs (H1–H6; Extended Data Fig. 4c,d), each enriched in neutrophils from the different tissues and conditions (Extended Data Fig. 4e). Notably, cross-species comparison revealed strong conservation between the six human and seven mouse hubs. The main difference was that the human hub 6 combined features of mouse IS-II and APC hubs and was enriched in human lung and tumour tissues (Extended Data Fig. 4f, g).

In summary, NeuMap offers insights into the transcriptional structure of the neutrophil compartment across multiple tissues and physiological conditions at single-cell resolution, enables the integration of profiles and signatures from existing datasets, and uncovers a conserved and limited set of transcriptional states across different anatomical sites, disease conditions, genetic backgrounds, microbiome statuses and species.

Molecular, functional and spatial profiling

We next explored the potential of this integrative map to uncover new biological properties of neutrophils. NeuMap indicated that most neutrophils from the lungs, liver and intestine localized within the *Cd14*+ *Ptgs2*+ IS-I hub, predicting immunosuppressive and angiogenic functions in these organs (Fig. 1f, Extended Data Fig. 1e and Fig. 2a). To validate this prediction, we isolated neutrophils from the lung and compared their angiogenic and immunosuppressive properties with neutrophils from the blood, bone marrow and spleen, which localized in different hubs (Fig. 1e). Using an in vivo Matrigel plug model, we found that co-injection of lung neutrophils potently induced

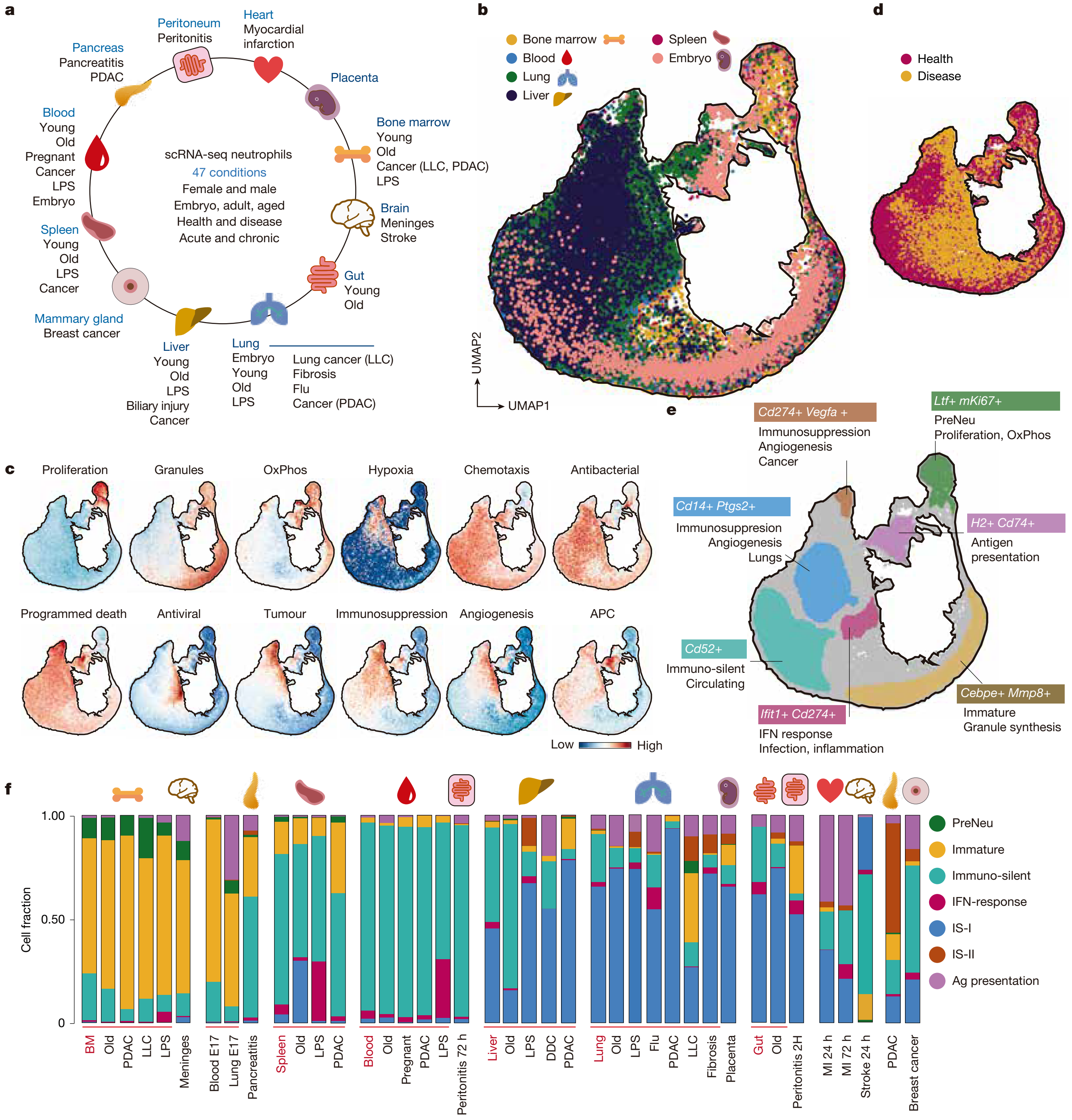

Fig. 1 | NeuMap, an integrative map of the neutrophil transcriptome. **a**, Scheme of the tissues and biological conditions used to generate NeuMap using scRNA-seq. Further details in Supplementary Table 1. **b**, UMAP visualization by tissue of origin. **c**, Score value of gene sets for specific biological processes. Complete gene lists in Supplementary Table 2. APC, antigen-presenting cell; OxPhos, oxidative phosphorylation. **d**, UMAP visualization of neutrophils extracted from health or diseased conditions. **e**, Scheme of the functional compartmentalization of NeuMap. Each hub is defined by areas containing the top 85% K-mass score. **f**, Stacked bars showing the proportion of cells from different organs and conditions in each transcriptional hub. Please note that not all 47 conditions are included in the panel. Tissues from healthy young male and female mice are labelled in red, and treatments or disease for each tissue are indicated at the bottom of each bar.

neovascularization compared with neutrophils from the other tissues (Fig. 2b). Similarly, co-incubation of lung neutrophils with activated CD8+ OT-I T cells had the most potent suppressive activity in a cytotoxicity assay against ovalbumin (OVA)-expressing B16 melanoma target cells (Fig. 2c), together confirming the predicted functional properties of neutrophils on the basis of their distribution in NeuMap.

To gain insights into transcriptional regulators of the IS-I hub, we performed single-cell assay for transposase-accessible chromatin (ATAC) sequencing combined with RNA sequencing (Dogma-seq)[20] of neutrophils from the same four tissues at steady-state or during conditions of inflammation and cancer. A genome-wide search for transcription factor binding sites revealed that the IS-I hub was enriched in

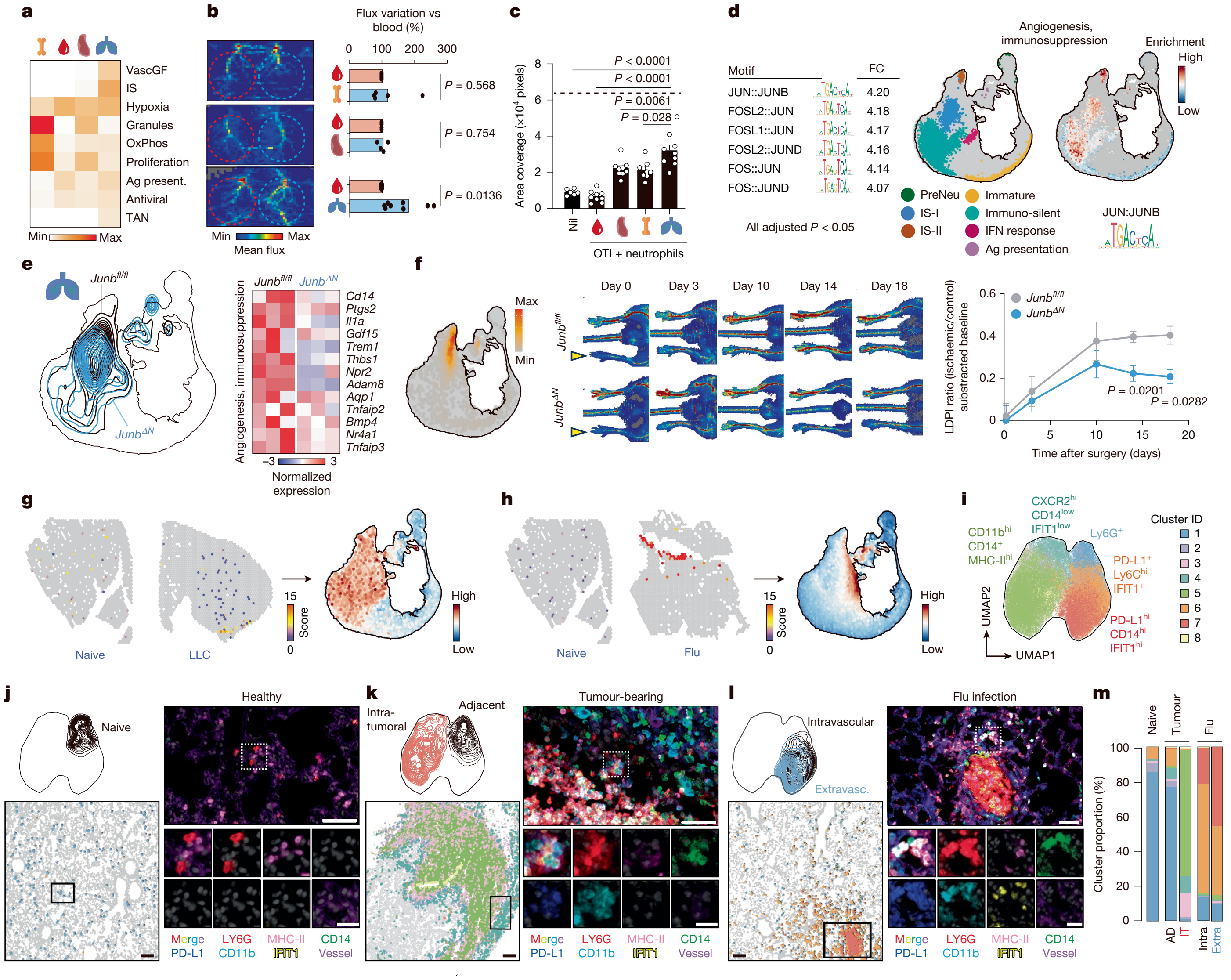

Fig. 2 | NeuMap illuminates molecular and functional properties of lung neutrophils. **a**, Heat map showing contribution of bone marrow, spleen, blood and lung neutrophils to the top 5% of cells for the indicated functional gene signatures. Cell number was downsampled to 1,000 per tissue. Ag present., Ag presentation; IS, immunosuppression; max, maximum; min, minimum; TAN, tumour-associated neutrophils; VascGF, vascular growth factors. **b**, In vivo Matrigel plug assay assessing angiogenic potential of neutrophils from indicated tissues. Left, representative Doppler imaging; right, quantification. Data are mean ± s.e.m. from $n = 8$ (lung) and $n = 4$ (spleens and bone marrow) biologically independent mice. Two-tailed t-test. **c**, OT-I T cell killing of B16OVA cells in the presence of tissue neutrophils. Dashed line, OT-I only; nil, untreated OT-I. Data are mean ± s.e.m. from $n = 6$ control and 9 independent experiments. One-way ANOVA with Dunnett's multiple comparisons. **d**, Dogma-seq analysis mapping neutrophils onto NeuMap. Left, top transcription factor motifs that are enriched in the IS-I hub. Right, enrichment score for JUNB binding sites. **e**, Left, contour plots of control *Junb*$^{fl/fl}$ and *Junb*$^{\Delta N}$ lung neutrophils mapped onto NeuMap. Right, heat map of differentially expressed genes (DEGs) (Supplementary Table 6). **f**, K-mass projection of neutrophils from ischaemic hindlimbs and kinetics of revascularization in control and *Junb*$^{\Delta N}$ mice. Data are mean ± s.e.m. from $n = 7$–9 biologically independent mice per group. Two-way ANOVA with Tukey correction. LDPI, laser doppler perfusion imaging. **g**,**h**, Spatial transcriptomics of immunosuppression scores (**g**) and interferon-response scores (**h**) in neutrophils from naive, LLC and flu-infected lungs. **i**, UMAP clustering of lung neutrophils from tumour-bearing, flu-infected and healthy mice by multiparametric staining. **j**–**l**, UMAP and representative immunofluorescence of lung sections from naive mice (**j**), tumour-bearing mice (**k**) and flu-infected mice (**l**), showing cluster-defining markers. Data are from $n = 3$ biologically independent mice per condition (one section per mouse). Scale bars: 50 μm (main image (top)); 20 μm (expanded view (middle and bottom)). **m**, Distribution of neutrophil clusters from **i** in intratumoural (IT), tumour-adjacent (AD), intravascular (intra) and extravascular (extra) tissue.

motifs bound by the AP-1 complex, SMAD and NF-κB isoforms (Fig. 2d and Extended Data Fig. 5a, b), suggesting control of the angiogenic and immunosuppressive properties of lung neutrophils by these factors. By contrast, the immature and immuno-silent hubs were enriched in motifs for members of the CEBP and KLF families, consistent with their roles in neutrophil maturation[13,21]. IRF- and STAT-related binding sites were largely restricted to the IFN-response hub, AP-1 and Bhlhe sites dominated in IS-II neutrophils, and SMAD and AP-1 binding motifs in the antigen-presenting hub. Finally, CEBP, NF-κB and SMAD binding sites were accessible in most hubs of NeuMap (Extended Data Fig. 5a,b), suggesting broad control of neutrophil transcription by these factors.

To investigate the predicted role of AP-1 in regulating the properties of neutrophils in the IS-I hub, we generated mice with neutrophil-specific deletion of *Junb* (MRP8^{cre};*Junb*$^{fl/fl}$ or *Junb*$^{\Delta N}$ mice), a component of the AP-1 complex. Bulk transcriptome analysis of lung neutrophils from control versus *Junb*$^{\Delta N}$ mice revealed enrichment in genes associated with immunosuppression, angiogenesis and cancer, and this signature projected over the IS-I and IS-II hubs of NeuMap (Extended Data Fig. 5c), and scRNA-seq analyses revealed altered distribution of lung and liver neutrophils onto NeuMap, as predicted (Fig. 2e and Extended Data Fig. 5d). These alterations, however, were partial, suggesting the contribution of other transcriptional regulators in the IS-I hub. These alterations were cell-intrinsic because transfer of bone marrow neutrophils to the lungs of wild-type mice induced expression of genes involved in immunosuppression and angiogenesis only in control, but not in JUNB-deficient neutrophils (Extended Data Fig. 5e). Of note, although *Junb*$^{\Delta N}$ neutrophils differentiated normally (Extended Data Fig. 5f), their capacity to suppress T cell activity in vitro and to promote Matrigel vascularization in vivo was lost (Extended Data Fig. 5g,h). Consistently, lungs from *Junb*$^{\Delta N}$ mice showed reduced endothelial cell proliferation and numbers (Extended Data Fig. 5i,j) during young age or after irradiation[1], and subcutaneous Lewis lung carcinoma (LLC) tumours in these mice recruited neutrophils with reduced expression of cancer-associated markers, including CD14, Sca1 and PD-L1 (Extended Data Fig. 5k,l). This correlated with blunted endothelial cell proliferation and increased T cell infiltration in the tumours, and reduction in tumour growth in *Junb*$^{\Delta N}$ mice (Extended Data Fig. 5m–o), indicating that neutrophils also require active JUNB signalling to acquire a pro-tumoural state (IS-II hub).

We used a model of hindlimb ischaemia to examine JUNB-dependent reprogramming of neutrophils during neovascularization in a different tissue. scRNA-seq of neutrophils from ischaemic limbs showed that they distributed between the IS-I and IS-II hubs (Fig. 2f) and *Junb*$^{\Delta N}$ mice showed impaired restoration of blood flow in the ischaemic limb compared with littermate controls (Fig. 2f), together demonstrating that AP-1 regulates the regenerative properties of neutrophils across tissues.

To further explore the idea that NeuMap classifies neutrophils by functional state, rather than only by anatomical location, we profiled neutrophils from the same tissue subjected to different challenges. Indeed, whereas neutrophils from naive lungs localized mainly in the IS-I hub, those from influenza virus (flu)-infected lungs shifted towards the IFN-response and Ag presentation hubs, and those exposed to LLC tumours moved towards the IS-II hub (Extended Data Fig. 6a), indicating that both tissue and physiological context shape the phenotype and function of neutrophils. We then used spatial transcriptomics of lung sections from naive, flu-infected and tumour-bearing mice to directly associate the distribution of neutrophils in different transcriptional hubs with their microanatomical localization. We annotated cell types and functional signatures in different regions of the lung samples (Extended Data Fig. 6b–d) and identified the spots that contained neutrophils. Using similarity scores for the IFN-response and IS-I hubs (Fig. 2g,h), we found a high immunosuppression signature in neutrophils from border tumour areas compared with those from the tumour core, adjacent tissue or naive lungs. By contrast, the interferon-response score was high in neutrophils around infected bronchioles but was almost undetectable in naive lungs (Fig. 2g,h and Extended Data Fig. 6c). Conversely, projection of the signature of the spatially identified neutrophils onto NeuMap revealed that neutrophils from tumours distributed in areas that included the IS-I and IS-II hubs, whereas those from the flu-infected lungs overlapped with the IFN-response hub (Fig. 2g,h). The association between the IS-II hub and neutrophils in border areas of tumours may explain the aggressive nature of the invasive tumour front[22], and we confirmed these spatial associations in a pancreatic ductal adenocarcinoma (PDAC) spatial dataset[7] (Extended Data Fig. 6e). Notably, IFN-response, IS-I and IS-II neutrophil signatures could also be detected in the border zone of infarcted areas of the myocardium (dataset from ref. 23; Extended Data Fig. 6e), suggesting that different stresses can elicit similar responses in neutrophils. These analyses also revealed that neutrophils from different hubs have distinct spatial associations with various types of T cells, macrophages and fibroblasts (Extended Data Fig. 6f), providing insights into where these neutrophils are educated in the tissue and their potential effect on other immune and non-immune cells.

To examine the association of the hubs in NeuMap with protein expression and spatial distribution, we performed cyclic labelling of lung sections under the same conditions of infection and cancer. We selected a panel of eight antibodies that were predicted to identify neutrophils from the different hubs present in the lungs (Extended Data Fig. 6g, h) and performed unbiased clustering and uniform manifold approximation and projection (UMAP) embedding to identify eight patterns of neutrophils by protein content (clusters 1–8 in Fig. 2i–l). Each phenotypic cluster identified neutrophils associated with different perturbations and regions of the tissue (Fig. 2m and Extended Data Fig. 6h,i). For example, cluster 1 lacked specific markers and was typical of neutrophils from naive lungs and non-affected tissue adjacent to tumours (Fig. 2j,k), MHCII^{+}CD14^{+}CD11b$^{\mathrm{hi}}$ neutrophils (cluster 5) were intratumoural, and PD-L1^{+}IFIT1^{+} neutrophils (clusters 6 and 7) were abundant in flu-infected sites (Fig. 2k,l and Extended Data Fig. 6i,j).

Overall, these findings highlight the potential of NeuMap to integrate transcriptional, phenotypic, anatomical and functional profiles of neutrophils across tissue microenvironments and physiological states.

Transcriptional trajectories in NeuMap

To explore the transcriptional dynamics in NeuMap, we examined the distribution of neutrophils from several tissues across the different transcriptional hubs in conditions of health, cancer (PDAC) and acute inflammation (from lipopolysaccharide (LPS) injection) (Fig. 3a–c). The distribution of the neutrophils in NeuMap varied for each condition; neutrophils from healthy mice distributed through the immature, immuno-silent, IS-I and IFN-response hubs (Fig. 3a). By contrast, tumour-bearing mice had few neutrophils in the immuno-silent and IFN-response hubs, and instead shifted towards the IS-I and IS-II hubs (Fig. 3b). Finally, most neutrophils from LPS-treated mice localized in the IFN-response hub (Fig. 3c). Of note, the distribution of neutrophils in NeuMap remained relatively constant for each tissue across all conditions (Extended Data Fig. 7a), suggesting that both tissue and physiological state determine the transcriptional diversity of neutrophils.

We utilized RNA velocity analysis[24] to infer the transcriptional trajectories of neutrophils in NeuMap in conditions of health, cancer and inflammation. Whereas the transition vectors from the PreNeu to the immature hub were present in all groups, the downstream trajectories varied across conditions. Healthy mice favoured the transition from the immature to the immuno-silent hub, tumour-bearing mice transitioned towards the IS-I and IS-II hubs, and inflamed mice transitioned towards the IFN-response hub (Fig. 3a–c). We validated these predicted trajectories by genetic-tracing experiments using iLy6G$^{\mathrm{tdTomato}}$ mice[1] to label neutrophils with tdTomato in the marrow and tracking potential alterations in granulopoiesis and neutrophil fates in tissues[1] (Extended Data Fig. 7b–d). Maturation paths were similar for the three conditions in the bone marrow, but they followed separate trajectories in the other tissues (Fig. 3d and Extended Data Fig. 7c). Notably, neutrophils from LPS-treated mice activated an additional route of maturation directed towards the IFN-response hub (maturation path II; Fig. 3e and Extended Data Fig. 7c). This trajectory was similar to the canonical maturation path I (shown in Fig. 3e) but lacked activation of genes typically associated with homeostatic maturation (*Cd101*, *Cxcr4*, *Sell* or *Csf3r*), whereas the expression of inflammatory genes (*Icam1* and *Cd274*) was increased (Extended Data Fig. 7c), suggesting an accelerated and activated type of granulopoiesis. Consistently, we found reduced frequency and intensity of CD101 expression and increased presence of PD-L1^{+}ICAM1^{+} neutrophils in the bone marrow after LPS treatment (Extended Data Fig. 7e), and accelerated transit of neutrophils across tissues in mice treated with LPS (Extended Data Fig. 7f).

When comparing the trajectories in peripheral tissues, we noticed that tdTomato^{+} neutrophils from all conditions transited between the different transcriptional hubs defined in NeuMap (Fig. 1e) and began branching out into two separate trajectories by 36 h (Fig. 3d). However, the preferred pathways differed between conditions; neutrophils in healthy and tumour-bearing mice favoured the IFN-response

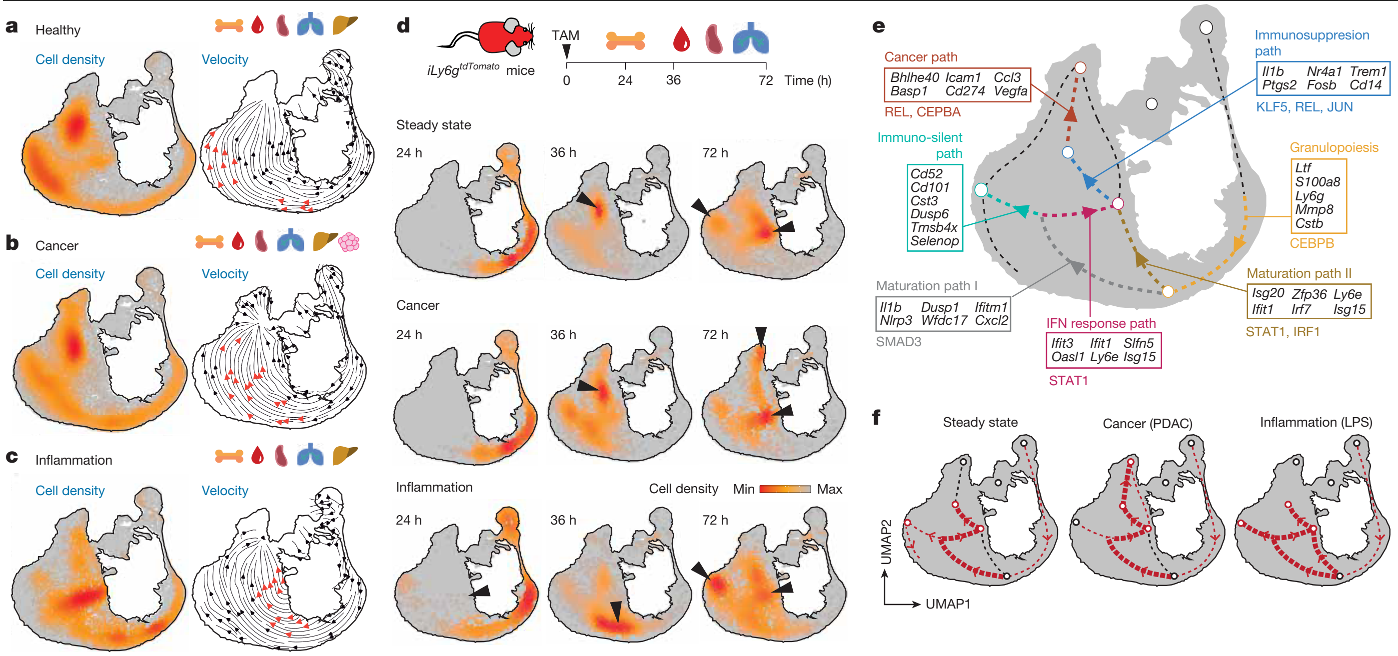

Fig. 3 | Transcriptional trajectories in NeuMap. a–c, K-mass score (representing cell density) of neutrophils from the bone marrow, blood, spleen, lungs and livers of naive mice (**a**), tumour-bearing mice (PDAC tumours) (**b**) and LPS-treated mice (**c**), projected onto NeuMap. RNA velocity analyses were performed for each of the conditions and the main developmental trajectories are highlighted with red arrowheads. **d**, K-mass score of the mapped time-stamped neutrophils from steady-state, inflammation (LPS) and tumour-bearing (LLC) mice onto NeuMAP. Neutrophils were tracked at 24 h (bone marrow, black dots), 36 h and 72 h (blood, spleen and lung, orange-red scale) after tamoxifen-induced labelling of *Ly6g*-tdTomato cells. **e**, Network model highlighting the trajectories identified in **a**–**d**, showing genes and transcription factors enriched for each trajectory. Transcription factors were selected when identified by both EnrichR and chromatin accessibility analyses. Note that we did not find any transcription factor enriched in the immuno-silent path. For a complete list see Supplementary Table 7. **f**, Inference of preferred trajectories for neutrophils from healthy, tumour-bearing and inflamed mice from the data in **a**–**d**.

hub by 72 h, whereas inflammation favoured their transition to the immuno-silent hub. We confirmed this pattern in a model of zymosan-induced peritonitis (Extended Data Fig. 7g). Notably, only neutrophils from tumour-bearing mice transited from the IS-I hub to the IS-II hub (Fig. 3d and Extended Data Fig. 7d).

We modelled these findings in a network of transcriptional transitions and hubs in NeuMap, and used pseudotime analysis to identify genes that were specifically activated in those transitions (Fig. 3e and Extended Data Fig. 7h). We found, for example, that the canonical maturation programme (path I) involved the simultaneous activation of inflammatory, anti-inflammatory and interferon-regulated genes (for example, *Dusp1*, *Nlrp3* and *Ifitm1*; Fig. 3e). This profile was consistent with this path splitting into at least two trajectories, one leading to the immuno-silent hub and the other leading to the IFN-response hub, suggesting that at this early stage, neutrophils activate broad genetic programmes without committing to only one. Representation of the preferred trajectories of neutrophils onto NeuMap suggested that, although the global structure of this network of trajectories is conserved, each condition has preferred transcriptional paths that are followed by neutrophils (Fig. 3f). Thus, mapping of temporal series onto NeuMap infers transcriptional dynamics of neutrophils as they mature in the bone marrow and transition into peripheral tissues to acquire new properties.

Deterministic signalling drives NeuMap trajectories

We sought to identify cues that controlled the transition of immature neutrophils to the main hubs. We first took advantage of a dataset containing the single-cell transcriptomes of lymph node leukocytes exposed to 86 different cytokines[25] and performed in silico screening by mapping the neutrophils from this dataset onto NeuMap (Fig. 4a). Most cytokines induced profiles associated with a single hub; for example, interferons and IL-36 directed neutrophils to the IFN-response hub, GM-CSF and APRIL directed them to the IS-II hub, and IL-1β, IL-1α and TNF directed them to a region between the IS-I and IS-II hubs (Fig. 4a,b).

We validated these observations by exposing bone marrow neutrophils to eight different cytokines or conditioned media from two cancer cell lines (LLC and FC1242). We profiled the cells using a custom panel of 21 targeting markers associated with different areas of NeuMap (Fig. 4c) to categorize neutrophils into 5 possible profiles (Fig. 4c and Extended Data Fig. 8a–c). We found that TGFβ favoured maturation (CD101^{hi}LY6G^{hi}); IFNβ induced an inflammatory-like phenotype (PD-L1^{hi}CD14^{low}CX3CR1^{hi}); and GM-CSF induced a cancer-associated profile (CD101^{low}PD-L1^{hi}CD14^{hi} dcTRAIL-R1^{hi}MHC-II^{+}). Finally, tumour-conditioned media induced phenotypes that resembled GM-CSF treatment but were milder and more biased towards the immunosuppressive phenotype (Fig. 4c–e and Extended Data Fig. 8a–d). Notably, we confirmed that these phenotypes mirrored the predicted transcriptional states in NeuMap by scRNA-seq of the cultured bone marrow neutrophils and projection onto NeuMap (Fig. 4f), suggesting that these cytokines drive the different transcriptional trajectories identified in NeuMap (Fig. 3e).

To formally demonstrate this, we generated mice with neutrophil-specific deficiency in receptors for TGFβ (*Tgfbr*$^{\Delta N}$ mice), type I interferon (*Ifnar*$^{\Delta N}$) and GM-CSF (*Csf2r*$^{\Delta N}$). In vitro treatment of bone marrow neutrophils from these mutant mice prevented the phenotypic changes elicited by their respective cytokines, resulting in reduced maturation-, inflammation- and cancer-associated phenotypes (Fig. 4g and Extended Data Fig. 8e). We then performed scRNA-seq of neutrophils from the relevant tissues of *Tgfbr*$^{\Delta N}$ (bone marrow), *Ifnar*$^{\Delta N}$ (blood) and *Csfr2*$^{\Delta N}$ (LLC tumour) mice and their respective controls and mapped their distribution in NeuMap. Neutrophils from *Tgfbr*$^{\Delta N}$ mice showed delayed maturation, loss of the IFN-response hub in *Ifnar*$^{\Delta N}$ mice and a shift away from the IS-II hub in *Csf2r*$^{\Delta N}$ mice (Fig. 4h and Extended Data Fig. 8f), confirming that these cytokines reprogramme neutrophils to defined transcriptional states in vivo.

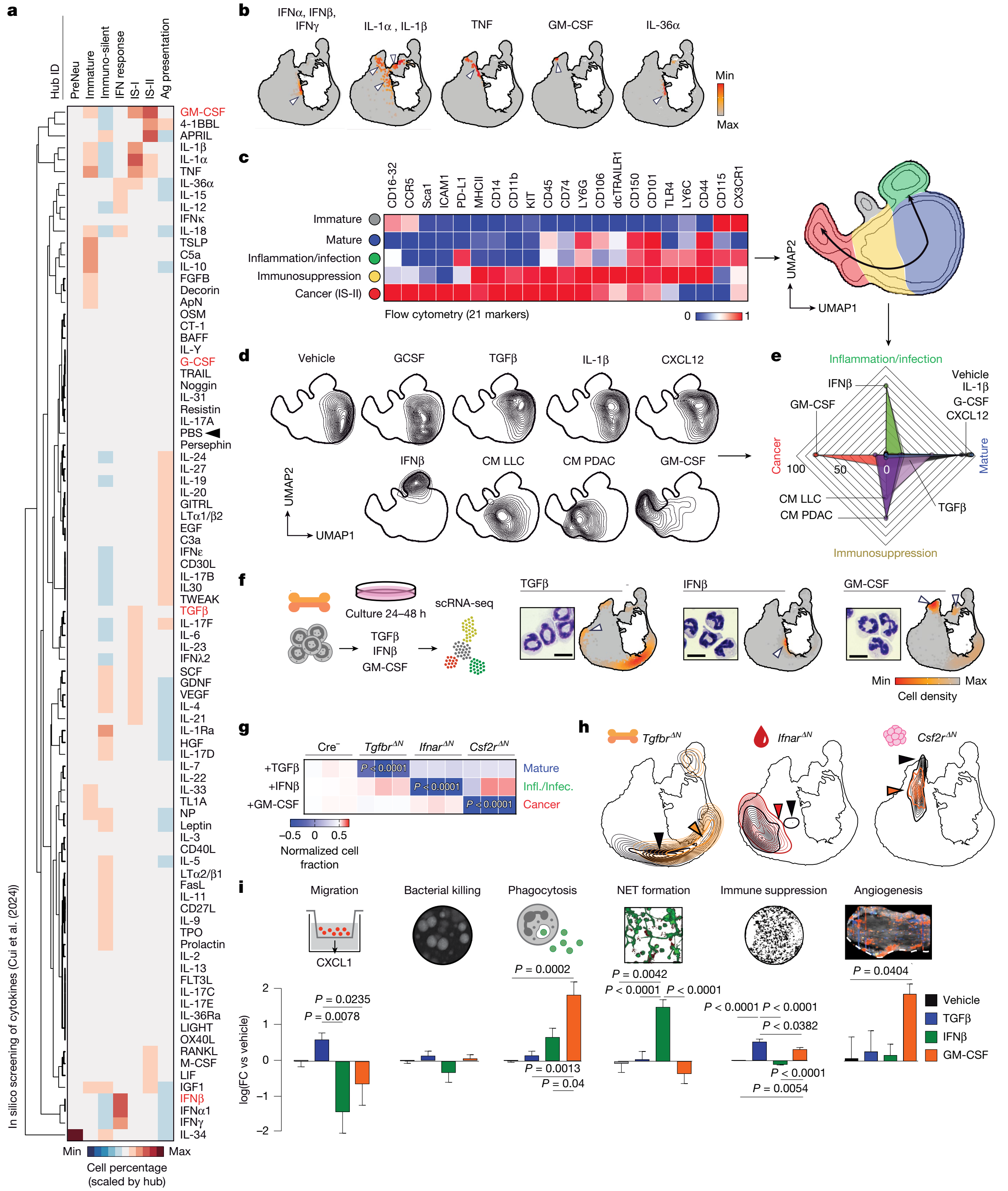

Fig. 4 | Signals that drive neutrophil maturation along the different paths. **a**, In silico screening of cytokine induction of transcriptional profiles[25]. Heat map shows lymph node-derived neutrophils treated in vivo with cytokines or PBS (arrowhead). Cells were classified into NeuMap hubs using Seurat LabelTransfer; proportions are colour-coded by hub. **b**, Distribution of transcriptomes from cytokine-treated neutrophils projected onto NeuMAP. **c**, Heat map of 21 markers in bone marrow-derived neutrophils (left) and UMAP projection (right) defining five states (immature, mature, inflammation/infection, IS-I and IS-II). Data from $n = 4$ independent experiments. **d**, Contour plots of neutrophils from **c** after 24 h treatment with cytokines or conditioned media from LLC (CM LLC) and PDAC (CM PDAC). **e**, Radar chart summarizing neutrophil distributions from **d**. **f**, Scheme, haematoxylin and eosin (H&E) staining and NeuMAP projection (K-mass) of bone marrow neutrophils cultured with TGFβ, IFNβ or GM-CSF. Micrographs show representative nuclear morphologies (immature ringed versus multilobulated). Scale bars, 10 μm. **g**, Heat map visualization of the proportion of bone marrow neutrophils from *Tgfbr*$^{\Delta N}$, *Ifnar*$^{\Delta N}$ and *Csf2r*$^{\Delta N}$ mutants and Cre^{-} controls in the mature, inflammation/infection (infl./infect.) and cancer phenotypic clusters after treatment with the indicated cytokines for 24 h, determined by flow cytometry. Data are mean ± s.e.m. from $n = 3$ biologically independent mice per group. One-way ANOVA followed by Dunnett's multiple comparison test. **h**, Contour plots showing distribution of neutrophils from indicated genotypes in NeuMAP; shifts (arrowheads) are quantified in Extended Data Fig. 8f. **i**, Functional assays of neutrophils treated with vehicle or cytokines, measuring migration ($n = 3$–4), bacterial killing ($n = 6$–7), phagocytosis ($n = 4$), NET formation ($n = 10$–13), immunosuppression ($n = 4$–6) and angiogenesis ($n = 7$–8). Data are mean ± s.e.m. from $n = 2$ independent experiments. One-way ANOVA followed by Dunnett's multiple comparison test. FC, fold change.

We then used multimodal profiling of chromatin accessibility and gene expression at single-cell resolution[20] to identify transcription factors that are potentially involved in the induction of these programmes, which we validated using the HOXB8 system with CRISPR-mediated deletion of selected transcription factors[21] (Extended Data Fig. 8g,h). Deletion of *Cebpb*, *Rfx2* and *Runx1* impaired neutrophil maturation and subsequent cytokine-driven polarization. By contrast, *Irf5* was required for the infection/inflammation profile, and *Relb* was required for the acquisition of the cancer/immunosuppressive phenotype in response to GM-CSF or PDAC-conditioned medium. Finally, *Junb* deletion had broad effects on differentiation, including the IS-I/IS-II phenotype (Extended Data Fig. 8g,h), and this could be rescued by its enforced expression in *Junb*$^{-/-}$ HOXB8 cells (Extended Data Fig. 8i–k).

We finally used this in vitro strategy to enrich for neutrophils in transcriptional states associated with different regions of NeuMap and assess their core functional properties, including chemotaxis, phagocytosis and neutrophil extracellular trap (NET) formation, as well as bactericidal, immunosuppressive, or angiogenic activities (Fig. 4i and Supplementary Fig. 3a–f). TGFβ induced moderate migratory and immunosuppressive activities. IFNβ, by contrast, impaired migration but activated phagocytosis and NET formation, suggesting activation of an antimicrobial programme. Finally, GM-CSF impaired migration and enhanced phagocytosis, but additionally activated immunosuppressive and angiogenic properties (Fig. 4i and Supplementary Fig. 3e,f), consistent with scenarios of tissue repair and cancer[1,26,27].

Thus, these data suggest that the transcriptional transitions and functional states (hubs) defined in NeuMap are elicited by defined signals and transcription factors.

Conservation and predictive properties of NeuMap

We speculated that the rich transcriptional resolution of NeuMap could be harnessed to visualize neutrophil states across species, pathophysiological conditions and response to therapies. We first examined signatures associated with a favourable response to immunotherapy in a mouse model of lung cancer[27]. Visualization of these signatures onto NeuMap revealed altered trajectories and a shift from the IS-II hub towards the IFN-response hub in the responding group (Fig. 5a).

We then explored whether the transcriptional hubs defined in NeuMap persisted across species and pathological states, as suggested by our profiling of the human neutrophil compartment (Extended Data Fig. 4). Projection of neutrophil signatures extracted from published human datasets of infection, autoimmunity and cancer[12,28–30] (Fig. 5b and Extended Data Fig. 9a) onto the mouse NeuMap revealed that severe COVID-19 was associated with the PreNeu hub (Fig. 5b), in line with previous reports[31]. By contrast, active flu infection or systemic lupus localized in the IFN-response hub, and neutrophils from lung tumours localized in the IS-II hub (Fig. 5b and Extended Data Fig. 9a), in agreement with studies in humans[28,32,33]. Integration of neutrophil signatures from multiple human and mouse cancer types revealed a preferential association with the IS-II, Ag-presenting and IFN-response hubs (Extended Data Fig. 9a–c). Validating this finding, we found that exposure of human neutrophils differentiated from CD34$^+$ progenitors to IFNβ- and GM-CSF-elicited responses that strongly mirrored those in mice (Extended Data Fig. 9d).

We then examined human neutrophils in situ by high-resolution spatial transcriptomic analysis of 12 human lung specimens from healthy and lung adenocarcinoma samples (Fig. 5c). We identified five neutrophil transcriptomic profiles (clusters 1–5) that matched with the various hubs in the mouse NeuMap (Fig. 5d). For example, the healthy lung tissue was enriched in cluster 1 and cluster 2 neutrophils, which associated with the IS-I and Ag-presenting hubs, respectively, reflecting the findings in mice (Fig. 1f). By contrast, tumoural regions were enriched in cluster 4 and cluster 5, which shared features with the IS-II and Ag-presenting hubs (Fig. 5c,d). Neighbourhood analyses revealed differential associations of neutrophils from each cluster with distinct cell lineages (Extended Data Fig. 9e), together supporting the transcriptional, phenotypic and functional conservation of the mouse and human neutrophil compartments (Extended Data Fig. 4).

Finally, we investigated whether the precise distribution of blood neutrophils in NeuMap could help predict the pathophysiological state of the host. We performed scRNA-seq analysis of neutrophils from the blood of mice exposed to 18 different conditions, including cancer, microbial infections (viral and bacterial), sterile inflammation and physiological states (pregnancy, embryos and old age) (Fig. 5f). We found that projecting these neutrophils onto the full NeuMap markedly reduced their transcriptional overlap, as quantified using the Bhattacharyya index (Fig. 5g and Extended Data Fig. 10a,b). Thus, we used NeuMap as a scaffold to project the distributions of blood neutrophils and generated ten 'diagnostic regions' to enhance the spatial resolution and separability of the samples (Extended Data Fig. 10c). Using the overlap of blood neutrophils over these ten regions (Extended Data Fig. 10d), measured by their Bhattacharyya indices, we generated distribution 'barcodes' for each sample (Fig. 5h). Notably, these barcodes could discriminate between young and old male mice, pregnant female mice, atherosclerosis-prone *Apoe*$^{-/-}$ mice and those with early stages of cancer. Similarly, we could discriminate between different types of tumours or infections, as well as mice with active liver cholestasis versus those in remission (Fig. 5h and Extended Data Fig. 10c). Thus, NeuMap captures the transcriptional diversity of neutrophils with sufficient resolution to enable inference of host physiology by assessing the distribution of blood neutrophils, a feature with considerable diagnostic potential.

Discussion

NeuMap provides a transcriptional and functional map of the neutrophil compartment across organs, developmental stages and pathophysiological conditions. It reveals that, despite the wealth of transcriptional states reported in the literature[1–3,9,18,31,34], the neutrophil compartment is organized as a finite collection of transcriptional states—or hubs—that can be associated with recognizable biological properties and appears to be conserved between mice and humans (Supplementary Fig. 4). Further expansion and exploration of NeuMap should be a collective effort for the field.

We highlight three salient features of our study. First, the transcriptome of the neutrophil compartment is organized as a single structure without obvious branching or separated clusters, both in mice and humans, possibly reflecting the short lifespan of neutrophils and the continuous replenishment of the entire compartment[1,7]. Second, NeuMap reveals several functional hubs, mirroring the heterogeneity of neutrophil states reported in multiple studies[1,3,7,9,18,33,34]. The relatively small number of hubs, however, contrasts with the remarkable diversity of scenarios in which neutrophils have important roles. It aligns, however, with the observation that many of the populations reported in different studies converge into similar signatures and functions, as shown, for example, in the context of cancer[1,7,12,26,35,36]. Thus, NeuMap can be used as a reference platform to uncover core properties of neutrophils across environments and diseases. Third, we emphasize the transcriptional dynamism of the neutrophil compartment, as captured by NeuMap and validated in the timestamp analyses that illuminate trajectories connecting the different hubs. This suggests that interfering with these trajectories may be more effective than targeting terminally differentiated neutrophils, a strategy that still dominates neutrophil-based therapies[5].

Our study is limited by the relatively small number of pathophysiological conditions analysed. Perturbations associated with allergy, autoimmunity, mucosal inflammation or diseases associated with old age[32,37–40], as well as developmental processes remain uncharted in our NeuMap. It is also likely that additional cues not explored here (including cytokines, chemokines, signalling lipids, metabolites or mechanical

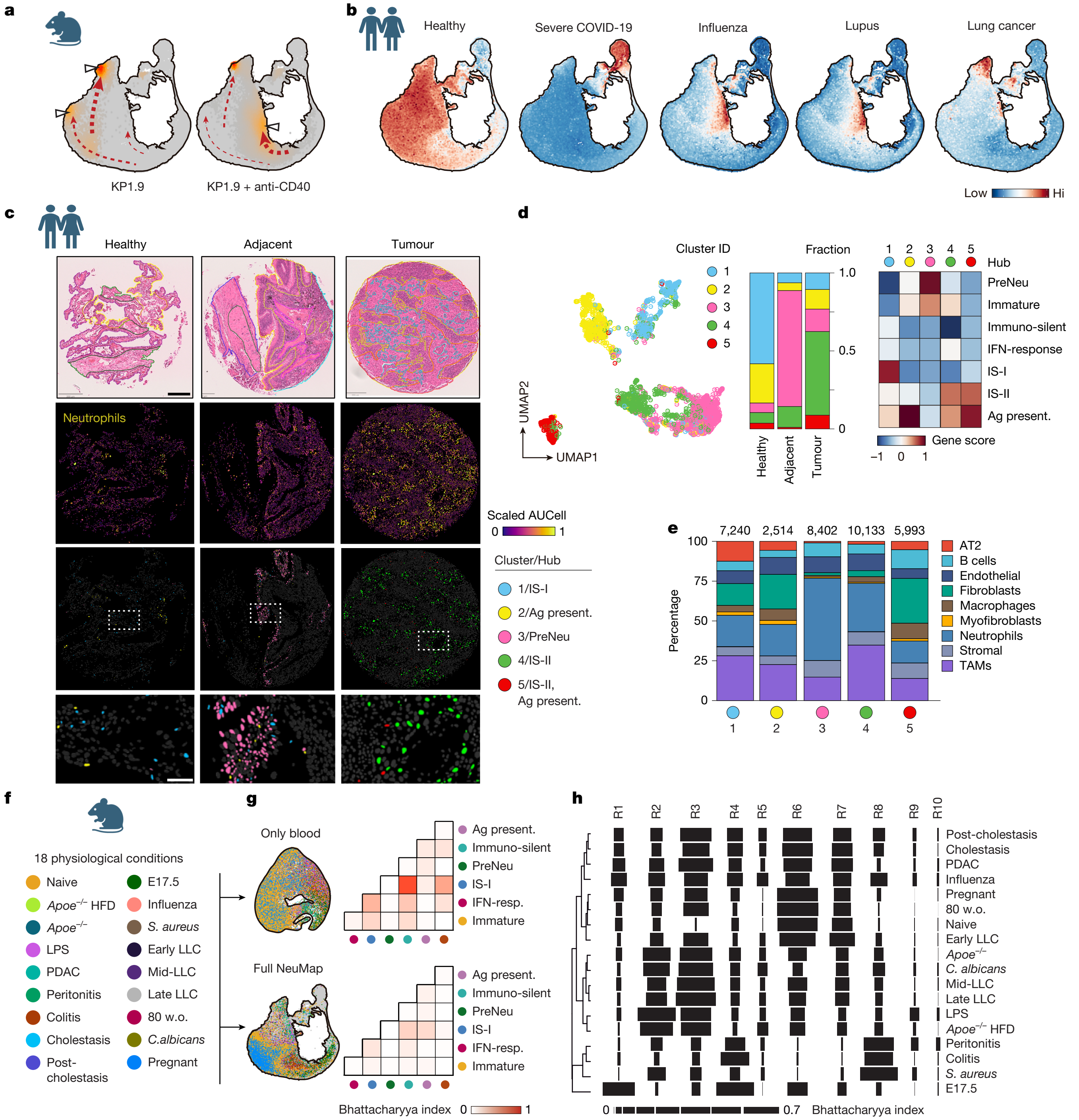

Fig. 5 | Predictive potential of NeuMAP. a, K-mass score of neutrophils from mouse lung cancer with or without with anti-CD40 immunotherapy[27], mapped onto NeuMAP. **b**, Signature scores from human neutrophils isolated from blood of healthy individuals or patients with severe COVID-19 (ref. 31, influenza A[28] or systemic lupus[29], or from lungs of patients with cancer[12]. **c**, Representative images from spatial transcriptomics of lung sections from patients with lung adenocarcinoma, with healthy tissue, adjacent tissue and tumour lesion from the same individual. Top, H&E-stained sections. Middle, spatial distribution of neutrophil gene signature scores. Bottom, enlarged views of indicated regions showing neutrophils from different clusters or hubs. Data are from $n = 8$ patients, with 2 formalin-fixed paraffin-embedded (FFPE) tumour sections and 1 adjacent non-tumorous section per patient. Representative images are shown. Scale bar: 200 µm (main image); 50 µm (expanded view). **d**, Left, UMAP embedding of neutrophil transcriptomes from the spatial transcriptomic dataset across all regions, identifying transcriptional clusters shown in **c**. Middle, bar plot showing relative abundance of each neutrophil state in healthy, adjacent and tumour areas. Right, heat map showing mean score per hub for each human cluster gene set (scaled by signature). Kruskal–Wallis test, $P < 0.001$ for all hubs. **e**, Percentage of nearest neighbouring cells to neutrophils from different clusters or hubs. Numbers indicate cells scored per group. AT2, alveolar type 2 cell; TAM, tumour-associated macrophage. **f**, Overview of 18 physiological and pathological conditions from which single-cell blood neutrophil transcriptomes were obtained. 80 w.o., 80 weeks old. **g**, Top, UMAP analysis of blood neutrophils from **f**, coloured by sample origin. Overlap across samples and NeuMap hubs (defined in Fig. 1) measured by Bhattacharyya index. Bottom, projection of blood neutrophil transcriptomes onto reference NeuMAP embedding; overlap is quantified in a correlation matrix. **h**, Bhattacharyya indices showing overlap of each sample with NeuMap regions (Extended Data Fig. 10C), represented as a barcode for each condition in a hierarchical tree. Drawings in **a**–**c**,**f** were created in BioRender. Cerezo Wallis, D. (2025) https://BioRender.com/pfm336w.

cues) and other transcriptional regulators contribute to the specification of neutrophils. Finally, our study highlights the collective nature of the compartment and hints that some properties of the collective differ from the sum of its individual components, a notion that may have a major impact on understanding its evolutionary logic and defining how neutrophils contribute to health and disease.

Online content

Any methods, additional references, Nature Portfolio reporting summaries, source data, extended data, supplementary information, acknowledgements, peer review information; details of author contributions and competing interests; and statements of data and code availability are available at https://doi.org/10.1038/s41586-025-09807-0.

1. Ballesteros, I. et al. Co-option of neutrophil fates by tissue environments. *Cell* **183**, 1282–1297.e18 (2020).
2. Ng, L. G., Ostuni, R. & Hidalgo, A. Heterogeneity of neutrophils. *Nat. Rev. Immunol.* **19**, 255–265 (2019).
3. Xie, X. Single-cell transcriptome profiling reveals neutrophil heterogeneity in homeostasis and infection. *Nat. Immunol.* **21**, 1119–1133 (2020).
4. Grieshaber-Bouyer, R. et al. The neutrotime transcriptional signature defines a single continuum of neutrophils across biological compartments. *Nat. Commun.* **12**, 2856 (2021).
5. Aroca-crevillén, A., Vicanolo, T., Ovadia, S. & Hidalgo, A. Neutrophils in physiology and pathology. *Annu. Rev. Pathol. Mech. Dis.* **19**, 227–259 (2024).
6. Casanova-Acebes, M. et al. Neutrophils instruct homeostatic and pathological states in naive tissues. *J. Exp. Med.* **215**, 2778–2795 (2018).
7. Ng, M. S. F. et al. Deterministic reprogramming of neutrophils within tumors. *Science* **383**, eadf6493 (2024).
8. Quail, D. F. et al. Neutrophil phenotypes and functions in cancer: a consensus statement. *J. Exp. Med.* **219**, 1–23 (2022).
9. Salcher, S. et al. High-resolution single-cell atlas reveals diversity and plasticity of tissue-resident neutrophils in non-small cell lung cancer. *Cancer Cell* **40**, 1503–1520.e8 (2022).
10. Kwok, I. et al. Combinatorial single-cell analyses of granulocyte-monocyte progenitor heterogeneity reveals an early uni-potent neutrophil progenitor. *Immunity* **53**, 303–318.e5 (2020).
11. Hidalgo, A., Chilvers, E. R., Summers, C. & Koenderman, L. The neutrophil life cycle. *Trends Immunol.* **40**, 584–597 (2019).
12. Zilionis, R. et al. Single-cell transcriptomics of human and mouse lung cancers reveals conserved myeloid populations across individuals and species. *Immunity* **50**, 1317–1334.e10 (2019).
13. Evrard, M. et al. Developmental analysis of bone marrow neutrophils reveals populations specialized in expansion, trafficking, and effector functions. *Immunity* **48**, 364–379.e8 (2018).
14. Grassi, L. et al. Dynamics of transcription regulation in human bone marrow myeloid differentiation to mature blood neutrophils. *Cell Rep.* **24**, 2784–2794 (2018).
15. Morrison, T., Watts, E. R., Sadiku, P. & Walmsley, S. R. The emerging role for metabolism in fueling neutrophilic inflammation. *Immunol. Rev.* **314**, 427–441 (2023).
16. Morosetti, R. et al. A novel, myeloid transcription factor, C/EBPε, is upregulated during granulocytic, but not monocytic, differentiation. *Blood* **90**, 2591–2600 (1997).
17. Singhal, S. et al. Origin and role of a subset of tumor-associated neutrophils with antigen-presenting cell features in early-stage human lung cancer. *Cancer Cell* **30**, 120–135 (2016).
18. Wu, Y. et al. Neutrophil profiling illuminates anti-tumor antigen-presenting potency. *Cell* **187**, 1422–1439.e24 (2024).
19. Fuster, J. J. et al. Clonal hematopoiesis associated with TET2 deficiency accelerates atherosclerosis development in mice. *Science* **355**, 842–847 (2017).
20. Mimitou, E. P. et al. Scalable, multimodal profiling of chromatin accessibility, gene expression and protein levels in single cells. *Nat. Biotechnol.* **39**, 1246–1258 (2021).
21. Khoyratty, T. E. et al. Distinct transcription factor networks control neutrophil-driven inflammation. *Nat. Immunol.* **22**, 1093–1106 (2021).
22. Horrée, N., van Diest, P. J., Sie-Go, D. M. D. S. & Heintz, A. P. M. The invasive front in endometrial carcinoma: higher proliferation and associated derailment of cell cycle regulators. *Hum. Pathol.* **38**, 1232–1238 (2007).
23. Yamada, S. et al. Spatiotemporal transcriptome analysis reveals critical roles for mechano-sensing genes at the border zone in remodeling after myocardial infarction. *Nat. Cardiovasc. Res.* **1**, 1072–1083 (2022).
24. La Manno, G. et al. RNA velocity of single cells. *Nature* **560**, 494–498 (2018).
25. Cui, A. et al. Dictionary of immune responses to cytokines at single-cell resolution. *Nature* **625**, 377–384 (2024).
26. Veglia, F. et al. Analysis of classical neutrophils and polymorphonuclear myeloid-derived suppressor cells in cancer patients and tumor-bearing mice. *J. Exp. Med.* **218**, e20201803 (2021).
27. Gungabeesoon, J. et al. A neutrophil response linked to tumor control in immunotherapy. *Cell* **186**, 1448–1464.e20 (2023).
28. Zhang, Y. et al. A single-cell atlas of the peripheral immune response in patients with influenza A virus infection. *iScience* **26**, 108507 (2023).
29. Wither, J. E. et al. Identification of a neutrophil-related gene expression signature that is enriched in adult systemic lupus erythematosus patients with active nephritis: clinical/pathologic associations and etiologic mechanisms. *PLoS ONE* **13**, e0196117 (2018).
30. Espinet, E. et al. Aggressive PDACs show hypomethylation of repetitive elements and the execution of an intrinsic IFN program linked to a ductal cell of origin. *Cancer Discov.* **11**, 638–659 (2021).
31. Schulte-Schrepping, J. et al. Severe COVID-19 is marked by a dysregulated myeloid cell compartment. *Cell* **182**, 1419–1440.e23 (2020).
32. Bennett, L. et al. Interferon and granulopoiesis signatures in systemic lupus erythematosus blood. *J. Exp. Med.* **197**, 711–723 (2003).
33. Wang, L. et al. Single-cell RNA-seq analysis reveals BHLHE40-driven pro-tumour neutrophils with hyperactivated glycolysis in pancreatic tumour microenvironment. *Gut* **72**, 958–971 (2023).
34. Xue, R. et al. Liver tumour immune microenvironment subtypes and neutrophil heterogeneity. *Nature* **612**, 141–147 (2022).
35. Veglia, F. et al. Fatty acid transport protein 2 reprograms neutrophils in cancer. *Nature* **569**, 73–78 (2019).
36. Fridlender, Z. G. et al. Polarization of Tumor-Associated Neutrophil Phenotype by TGF-β: "N1" versus "N2" TAN. *Cancer Cell* **16**, 183–194 (2009).
37. Van Avondt, K. et al. Neutrophils in aging and aging-related pathologies. *Immunol. Rev.* **314**, 357–375 (2023).
38. Gupta, S. & Kaplan, M. J. The role of neutrophils and NETosis in autoimmune and renal diseases. *Nat. Rev. Nephrol.* **12**, 402–413 (2016).
39. Woytschak, J. et al. Type 2 interleukin-4 receptor signaling in neutrophils antagonizes their expansion and migration during infection and inflammation. *Immunity* **45**, 172–184 (2016).
40. Özcan, A. & Boyman, O. Mechanisms regulating neutrophil responses in immunity, allergy, and autoimmunity. *Allergy* **77**, 3567–3583 (2022).

Publisher's note Springer Nature remains neutral with regard to jurisdictional claims in published maps and institutional affiliations.

Open Access This article is licensed under a Creative Commons Attribution-NonCommercial-NoDerivatives 4.0 International License, which permits any non-commercial use, sharing, distribution and reproduction in any medium or format, as long as you give appropriate credit to the original author(s) and the source, provide a link to the Creative Commons licence, and indicate if you modified the licensed material. You do not have permission under this licence to share adapted material derived from this article or parts of it. The images or other third party material in this article are included in the article's Creative Commons licence, unless indicated otherwise in a credit line to the material. If material is not included in the article's Creative Commons licence and your intended use is not permitted by statutory regulation or exceeds the permitted use, you will need to obtain permission directly from the copyright holder. To view a copy of this licence, visit http://creativecommons.org/licenses/by-nc-nd/4.0/.

© The Author(s) 2025, modified publication 2026

[1]Vascular Biology and Therapeutics Program and Department of Immunobiology, Yale University, New Haven, CT, USA. [2]Centro Nacional de Investigaciones Cardiovasculares Carlos III, Madrid, Spain. [3]Institute for Experimental Pathology (ExPat), Centre for Molecular Biology of Inflammation (ZMBE), University of Münster, Münster, Germany. [4]Centre Nacional d'Anàlisi Genòmica, Barcelona, Spain. [5]Singapore Immunology Network (SIgN), Agency for Science, Technology and Research (A*STAR), 8 A Biomedical Grove, Immunos, Singapore, Singapore. [6]Shanghai Immune Therapy Institute, Shanghai Jiao Tong University School of Medicine Affiliated Renji Hospital, Shanghai, China. [7]Departamento de Biología Celular e Histología, Facultad de Medicina, Universidad Complutense de Madrid, Madrid, Spain. [8]Department of Oncology, Haematology, Clinical Immunology and Rheumatology, University Hospital, Tübingen, Germany. [9]Rosalind and Morris Goodman Cancer Institute, McGill University, Montreal, Quebec, Canada. [10]Department of Mathematics and MOLAB-Mathematical Oncology Laboratory, Universidad de Castilla-La Mancha, Ciudad Real, Spain. [11]Department of Health Sciences and Technology, Laboratory of Exercise and Health, ETH Zürich, Zurich, Switzerland. [12]Unidad de Investigación Neurovascular, Departamento de Farmacología y Toxicología, Facultad de Medicina, Universidad Complutense and Instituto de Investigación Hospital 12 de Octubre, Madrid, Spain. [13]Department of Pediatrics, Emory University School of Medicine, Atlanta, GA, USA. [14]Department of Hematology, Renji Hospital, Shanghai Jiao Tong University School of Medicine, Shanghai, China. [15]Department of Obstetrics and Gynecology, Renji Hospital, School of Medicine, Shanghai Jiao Tong University, Shanghai, China. [16]Shanghai Key Laboratory of Gynecologic Oncology, Renji Hospital, School of Medicine, Shanghai Jiao Tong University, Shanghai, China. [17]Department of Urology, Renji Hospital, School of Medicine, Shanghai Jiao Tong University, Shanghai, China. [18]State Key Laboratory for Systems Medicine for Cancer, Division of Cardiology, Shanghai Cancer Institute, Renji Hospital, School of Medicine, Shanghai Jiao Tong University, Shanghai, China. [19]Media and Immersive Experience Center, The Design School, Arizona State University, Arizona State University, Temple, AZ, USA. [20]Ecology and Evolutionary Biology, Princeton University, Princeton, NJ, USA. [21]Department of Medicine, Center for Immunity and Inflammation, New Jersey Medical School, Rutgers, The State University of New Jersey, Newark, NJ, USA. [22]Department of Pathology, McGill University, Montreal, Quebec, Canada. [23]Department of Surgery, McGill University Health Center, Montreal, Quebec, Canada. [24]Universitat de Barcelona (UB), Barcelona, Spain. [25]Kennedy Institute of Rheumatology, University of Oxford, Oxford, UK. [26]CIBER en Enfermedades Cardiovasculares (CIBER-CV), Madrid, Spain. [27]School of Medicine, Westlake University, Hangzhou, China. [28]Department of Neuroscience and Biomedical Sciences, Universidad Carlos III de Madrid, Madrid, Spain. [29]These authors contributed equally: Daniela Cerezo-Wallis, Andrea Rubio-Ponce. [30]These authors jointly supervised this work: Lai Guan Ng, Andrés Hidalgo, Iván Ballesteros. ✉e-mail: nglaiguan@renji.com; andres.hidalgo@yale.edu; ivballes@salud.uc3m.es

Methods

Mice

All experiments were performed on 6-to-24-week-old C57BL/6 male and female mice. Young mice were defined as 8 to 12 weeks old, and old mice were defined as 22 to 24 months old at the time of analysis. Mice were maintained under specific pathogen-free conditions with chow and water provided ad libitum. mouse lines used were on the C57B1/6 J background and housed under specific pathogen-free conditions at the Centro Nacional de Investigaciones Cardiovasculares Carlos III, Singapore Immunology Network or Yale University. All mouse husbandry and experimentation was conducted using protocols approved by local animal ethics committees and authorities. Mice (*Mus musculus*) were maintained in racks with individual ventilation cages according to current Spanish, Singapore and US legislation (RD 53/2013 and EU Directive 63/2010, respectively). Mice have access to dust- and pathogen-free bedding, as well as sufficient nesting and environmental enrichment materials, to facilitate nesting. All mice were kept in environmental conditions of 45–65% of relative humidity, temperature of 21–24 °C, and a light:dark cycle of 12 h:12 h. Mice with neutrophil-specific deficiency in *Tgfbr2* (*Tgfbr*$^{\Delta N}$) were generated by crossing MRP8$^{\mathrm{CRE}}$ mice with *Tgfbr2*$^{fl/fl}$ mice[41]. Similarly, we generated neutrophil-specific mutants by crossing *Junb*-floxed[42], *Csf2r*-floxed[43] and *Ifnar1*-floxed mice[44] with the MRP8$^{\mathrm{CRE}}$ driver. *Apoe*$^{-/-}$ mice (B6.129P2-Apoetm1Unc; Taconic M&B). *Ly6g*^{creERT2} mice were crossed with *Rosa26*^{Tdtomato} mice as in ref. 1, resulting in the iLy6g$^{\mathrm{tdTom}}$ mice used in our fate mapping experiments. Gavage administration of tamoxifen (2 mg per mouse) was performed to induce CRE recombinase activity in 6-to-12-week-old male iLy6g$^{\mathrm{tdTom}}$ mice. JAXBoy (*Ptprc*^{K302E}) from Jackson laboratories and *Tet2*$^{-/-}$ mice[19] were used for adoptive bone marrow cell transfer. Eight-week-old male Germ-free mice (C57Bl/6) were kindly provided by the laboratory of N. Palm. In brief, Germ-free C57BL/6 mice were bred and maintained under sterile conditions in flexible film isolators (Class Biologically Clean) in the Palm laboratory Gnotobiotic Facility at Yale School of Medicine. Mice were housed in a temperature- and humidity-controlled room under a dark:light cycle of 12 h:12 h. All animal protocols were approved by the Yale University Institutional Animal Care and Use Committee (protocol 11513).

For the rewilding experiments, litters of mice were generated from multiple breeding pairs and randomly assigned to either remain in the institutional vivarium (laboratory mice) or be released into the outdoor enclosures (rewilded mice) to control for the microbiota at the onset of the experiment. Outdoor enclosures were previously described[45] and the protocols for releasing laboratory mice into the outdoor enclosure facility and then returning them to vivaria were approved by Princeton University (protocol 1982) and Rutgers University (protocol PROTO999900794). All protocols were approved by the corresponding local authorities of Madrid, Singapore, Rutgers, Princeton and Yale University.

Mouse models of disease

Stroke. Thrombotic occlusion of the middle cerebral artery was induced by the ferric chloride ($FeCl_3$) stroke model. In brief, mice were anaesthetized and maintained at 2% sevoflurane in a mixture of 0.2 l min^{-1} O_2:0.8 l min^{-1} air and temperature was kept at 36.5–37 °C using a heating blanket. The scalp was opened, and the middle cerebral artery was visualized with a stereomicroscope (PZMIV, World Precision Instruments). A piece of Whatman filter paper strip soaked in freshly prepared $FeCl_3$ (20%) was placed over the intact dura mater on the artery for 10 min and then removed to allow the formation of a thrombus. Following surgery, individual mice were returned to their cages with free access to water and food. Brains were collected 24 h after surgery to perform transcriptomics analysis.

Liver cholestasis. For the liver injury model, mice were fed a 0.1% of 3,5-diethoxycarbonyl-1,4-dihydrocollidine (DDC)-supplemented diet for 3 weeks before sample collection, housed with a 12 h:12 h light:dark cycle, and permitted ad libitum consumption of water as described[46]. An additional group of mice was fed a 0.1% DDC-supplemented diet for three weeks and afterward allowed to recover for three days under standard mouse diet to study the reversibility of the cholestatic phenotype.

Influenza A infection. A stock of the virus strain A/PR8/34 (H1N1) was diluted, and 100 plaque-forming units were administered intranasally to isoflurane-anaesthetized 8-to-12-week-old male mice in 50 µl of PBS. Mouse weight was monitored daily after infection and mice that presented weight loss of more than 20% of their initial body weight were euthanized and considered deceased. For transcriptomic studies, blood and lungs were collected on day 4 after infection.

Pancreatitis. Acute pancreatitis was induced by intraperitoneal injections of 50 µg kg^{-1} of cerulein (Sigma-Aldrich), every hour, for a total of 7 administrations. Mice were euthanized 24 h after the first injection.

Orthotopic pancreatic tumour model. Mice were anaesthetized with ketamine/xylazine, and had their abdomen shaved and swabbed with antiseptic. A 5 mm vertical incision was made in the skin and abdominal layer at a point 1 cm down from the xiphoid process of the sternum, and 1 cm to the right of the midline. The pancreas was exposed, 10^5 FC1242 cells were resuspended in phosphate-buffered saline (PBS) and mixed with Matrigel (BD) in a 1:1 ratio and were injected as a volume of 50 µl into the body of the pancreas to form a visible bolus using a 30G insulin needle. The pancreas was then returned to the abdominal cavity. The abdominal layer was closed with absorbable 5/0 sutures, while the skin was closed with non-absorbable 5/0 sutures. Superglue was applied over the sutures to ensure that they did not come undone after surgery. Mice were resuscitated with saline and were subcutaneously administered Buprenorphine (10 mg kg^{-1}) and Enrofloxacin (Baytril, 1.5 mg kg^{-1}) for the 2 days following surgery. Mice were euthanized at week 5 following surgery and tissues were collected for transcriptomic analysis.

Orthotopic breast tumour model. Mice were implanted orthotopically with 5×10^5 E0771 breast cancer cells in 50 µl Matrigel into the thoracic mammary gland of C57BL6/J mice. Additionally, the same procedure was followed using the BALB/c-derived 4T1 breast tumour cell cancer in BALB/c mice. Mice were euthanized at week 4 after implantation and tumours were collected for transcriptomic analysis.

Orthotopic lung cancer model. We administered 2×10^5 LLC cells in 100 µl PBS intravenously into the lateral tail vein of 8-week-old C57BL6/J mice. Mice were euthanized at week 1, 2 or 3 after the implantation and bloods and lungs were used for transcriptomics analysis.

Subcutaneous lung cancer model. Mouse LLC1 implants were generated in 8-week-old C57BL/6 mice by subcutaneous implantation of 0.5×10^6 cells (1 injection site per mouse). Tumour growth was followed every 2 days by measuring the 2 orthogonal external diameters using a calliper. Tumour volume was calculated as $V = \pi/6 \times L \times W \times H$, where L, W and H represent length, width, and height, respectively. Tumours were excised and processed for flow cytometry analysis when they reached 0.5 cm^3.

Caecal ligation and puncture-induced sepsis. Caecal ligation and puncture were performed as described[47]. In brief, the peritoneal cavity of ketamine/xylazine-anaesthetized mice was exposed with a small incision and the caecum was exteriorized. 80% of the caecum distal to the ileo-caecal valve was ligated using non-absorbable 7-0 suture. A 23G needle was then used to puncture both walls of the distal end of the caecum, and a small drop of faeces was extruded through the perforation. The ligated and punctured caecum was relocated inside the peritoneal cavity and both peritoneum and skin were closed. Blood was extracted three days after the puncture.

Peritonitis. Male 8-to-12-week-old mice were injected intraperitoneally with zymosan (1 mg, intraperitoneal injection, Sigma). After 2 h and 72 h we performed a peritoneal lavage for transcriptomic studies.

Myocardial infarction. Male 8-to-12-week-old mice were intubated, and temperature controlled throughout the experiment at 36.5 °C to prevent hypothermic cardioprotection. Thoracotomy was then performed, and the left anterior descending artery was ligated with a nylon 8/0 monofilament suture for 45 min. At the end of the ischaemia, the chest was closed, and mice were kept with 100% O_2 and given analgesia with buprenorphine (subcutaneous injection, 0.1 mg kg^{-1}) as described previously[47]. Mice were euthanized 24 h or 72 h h after surgery and the heart was isolated for transcriptomics studies.

Bleomycin-induced fibrosis. We administered 1 mg kg^{-1} of bleomycin sulfate to 8-to-12-week-old mice as previously described[48]. In brief, bleomycin was dissolved in saline and was instilled into the tracheal lumen through a cannula under isoflurane (2.5% in oxygen) anaesthesia. Bleomycin was injected at day 0 and at day 4. Mice were euthanized three weeks after bleomycin injection and lungs were collected for transcriptomics analysis.

***Staphylococcus aureus* Infection.** Mice were intravenously infected with 2.5×10^7 CFU of *S. aureus* (RNU4220 strain) and monitored for weight loss. For single-cell transcriptomic studies, blood was collected five days after infection.

***Candida* infection.** Mice were intravenously infected with 1.5×10^5 *Candida albicans* conidia (SC5314 strain), blood for single-cell transcriptomic studies was extracted at day 6 after infection[47].

LPS-induced inflammation. For transcriptomic studies, 400 ng of LPS (Sigma) were injected intravenously. Blood and tissues were collected 24 h after injection. An intraperitoneal lethal dose of LPS (40 mg kg^{-1}) was used as a model of endotoxic shock. Mice were monitored daily for weight loss. A weight loss of more than 20% of initial body weight was considered a lethal event and mice were euthanized at humane endpoints.

High-fat diet. *Apoe*$^{-/-}$ mice were fed for 6 weeks with a control or high-fat diet (HFD, 10.7% total fat, 0.75% cholesterol; Sniff) before blood extraction.

Dextran sulfate sodium colitis. To induce colitis, mice received for 9 days water with 1.5% dextran sulfate sodium salt (MP Biomedicals) as previously described[49]. Blood was collected on day 9 after dextran sulfate sodium treatment.

Hindlimb ischaemia. Hindlimb ischaemia experiments were performed as described[50]. In brief, mice were anaesthetized with isoflurane, the hindlimb was shaved, and, following a small incision in the skin, both the proximal end of the femoral artery and the distal portion of the saphenous artery were ligated. The artery and all side-branches were dissected free; after this, the femoral artery and attached side-branches were excised. Immediately after surgery, perfusion was measured by laser Doppler imaging of plantar regions of interest (ROIs) (Moor Instruments) and calculated as ratio of left (ligated) versus right (unligated) values. Ischaemic muscle samples for transcriptomics analysis were collected one day after surgery.

Model of clonal haematopoiesis and PCSK9-induced hypercholesterolemia. To model TET2 loss-of-function-driven clonal haematopoiesis, we performed an adoptive bone marrow transfer without pre-conditioning. Ten-week-old unirradiated JAXBoy (*Ptprc*^{K302E}) recipient mice were intravenously injected with a total of 1.5×10^7 unfractionated CD45.2$^+$ *Tet2*$^{-/-}$ bone marrow cells, administered as 3 consecutive daily doses of 5×10^6 cells[51]. Donor cells were collected from age-matched littermate *Tet2*$^{-/-}$ mice (8 to 10 weeks old) by flushing femurs and tibias following euthanasia. To induce hypercholesterolaemia, a recombinant AAV vector encoding a gain-of-function form of mouse PCSK9 (pAAV/D377Y-mPCSK9) was delivered via a single tail vein injection[52]. One week later, mice were placed on either a high-cholesterol western diet (Envigo, TD.88137; 42% calories from fat, 0.2% cholesterol) or a matched control diet for 13 weeks. At endpoint, adoptive bone marrow transfer mice were euthanized and *Tet2*$^{-/-}$ (CD45.2$^+$) or wild-type (CD45.1$^+$) neutrophils were isolated from peripheral blood and bone marrow by cell sorting. Cells were processed for scRNA-seq as described below.

Sample preparation and flow cytometry-assisted cell sorting

Mice were euthanized and Blood was taken through cardiac puncture with a 1 ml syringe attached to a 26G needle filled with 50 ml of 0.5 M EDTA. After blood collection, mice were perfused via the right ventricle with 10 ml of PBS to remove circulating blood cells. Tissues, including lung, tumours, muscle, heart, placenta and pancreas, were collected, cut into small pieces, and digested with Liberase TM (Sigma) and DNase I (Sigma) for 30 min at 37 °C. Following digestion, tissues were passed through 70-µm nylon mesh sieves using syringe plungers to obtain single-cell suspensions.

Bone marrow cells were obtained by flushing femurs with PBS containing 2 mM EDTA and 2% FBS using a 23G needle. Spleens were mechanically dissociated through 70-µm mesh filters. For colon isolation, intestines were cleaned, cut longitudinally and washed in PBS. After a 30-min incubation in 100 mM EDTA at 37 °C with shaking to remove epithelial cells, colon tissue was cut and digested in Liberase TM and DNase I for 30 min at 37 °C. Ear (skin) samples were processed by separating the dorsal and ventral sides, cutting them into small pieces, and digesting them in Liberase TM and DNase I for 90 min at 37 °C. The resulting suspensions were filtered as above. Peritoneal lavage was performed by injecting 10 ml of cold PBS into the peritoneal cavity, followed by gentle massage of the abdomen and careful aspiration of the fluid using a syringe and needle. The collected fluid was centrifuged, and the pellet was resuspended in fluorescence-activated cell sorting (FACS) buffer for staining.

For meninges isolation, mice were euthanized and decapitated. The skull was opened along the sagittal midline, and the brain was removed to expose the dura. The meninges were peeled off using fine forceps and placed directly into digestion solution on ice. For the brain, infarcted regions were dissected and digested for 30 min at 37 °C in an enzyme cocktail containing: 50 U ml^{-1} collagenase; 8.5 U ml^{-1} dispase; 100 µg ml^{-1} Nα-tosyl-L-lysine chloromethyl ketone hydrochloride; 5 U ml^{-1} DNase I in 9.64 ml HBSS without calcium, magnesium, or phenol red (Fisher Scientific, 14175-095). After digestion, brains were ground using a 2 ml glass-glass grinder, filtered through a 70-µm filter, and centrifuged. Cell pellets were resuspended in 7 ml of 35% Percoll, overlaid with 5 ml HBSS to form a gradient, and centrifuged at 800*g* for 30 min at 4 °C (no brake). The myelin layer and supernatant were discarded, and the final cell pellet was washed and resuspended in FACS buffer.

All single-cell suspensions were lysed in RBC lysis buffer (eBioscience) for 4 min and stained with the following antibodies: CD11b-PE (Clone M1/70, BioLegend, 1:200); LY6G-AF647 (Clone 1A8, eBioscience, 1:200); DAPI (1:10,000). Neutrophils were sorted as live (DAPI-negative), CD11b$^+$LY6G$^+$ cells using a FACS Aria sorter (BD Biosciences) at the Centro Nacional de Investigaciones Cardiovasculares (CNIC) Cytometry Unit. Bone marrow neutrophils were captured as lineage-negative (B220, CD18, NK.1.1, Ter119, CD3).

Cancer cell culture

The C57BL6/J syngeneic mouse LLC, E0771 breast luminal B and the BALB/c-derived 4T1 breast tumour cell cancer cell lines were from the American Type Culture Collection. The pancreatic adenocarcinoma FC1242 cell line (gift from D. Engle) was derived from *Pdx1*^{cre};*Kras*$^{G12D/+}$; *null/+* (KPC) mice. B16-OVAGFP cells were provided by the laboratory of D. Sancho. All cells were cultured in DMEM (Thermofisher) supplemented with 10% FBS (Thermofisher) and 100 μg ml^{-1} penicillin/streptomycin (Thomas Sci).

In vitro mouse neutrophil culture and analysis

Primary mouse neutrophils were obtained from the femurs and tibias of healthy C57BL/6J mice, or indicated genetically modified mouse model, by centrifugation. Erythrocytes were lysed using Red Blood Cell Lysis Solution (Qiagen; 79217). Cell strainer-filtered single-cell solutions were sorted in BD Aria Cell Sorter as DAPI^{-} CD45^{+}CD11b^{+}LY6G^{+}CD101^{+} mature, and DAPI^{-} CD45^{+}CD11b^{+}LY6G^{+}CD101^{-} immature neutrophils. Cells were seeded in 96-well plates, 50,000 cells per well, and cultured with complemented DMEM medium (vehicle), or with the indicated treatments. G-CSF (574606, BioLegend), TGFβ (7666-MB-005/CF, R&D), IFNβ (581302, BioLegend), CXCL12 (578704, BioLegend), IL-1β (401-ML, R&D Systems), and GM-CSF (315-03-20UG, Thermofisher) were used at a concentration of 10 ng ml^{-1}. Conditioned medium of LLC or KP-PDAC cells was obtained after 24 h culture of 80% confluence cells. Neutrophils were collected after 24 h or 48 h of treatment, and flow cytometry was performed using the following antibodies, all diluted 1:200 unless indicated otherwise: CCR5-BUV615-P (BD Biosciences, 752321, clone C34-3448), CD101-PE-Cy7 (eBioscience, 25-1011-82, clone MOUSHI 101), CD106-BUV563 (BD Biosciences, 741246, clone 429), CD115-BUV737 (BD Biosciences, 750948, clone AFS98), CD11b-BV510 (BioLegend, 101263, clone M1/70), CD11b-PE (BioLegend, 101208, clone M1/70), CD14-APC-Cy7 (BioLegend, 123318, clone Sa14-2), CD150-PE-Cy5 (BioLegend, 115911, clone TC15-12F12.2), CD16/32-PerCP-Cy5.5 (BioLegend, 101324, clone 93), CD274-BV421 (BioLegend, 124315, clone 10F-9G2), CD44-BV570 (BioLegend, 103037, clone IM7), CD45-APC (BioLegend, 103112, clone 30F11), CD74-BUV661 (BD Biosciences, 741572, clone In-1), KIT-BV605 (BioLegend, 135121, clone ACK2), CX3CR1-FITC (BioLegend, 149020, clone SA011F11), DC-Trail-R1-biotinylated (R&D Systems, BAF2378, polyclonal), I-A/I-E-BUV496 (BD Biosciences, 750281, clone M5/114.15.2), ICAM1-PE-Dazzle 594 (BioLegend, 1161130, clone YN1/1.7.4), LY6C-BV711 (BioLegend, 128037, clone HK1.4), LY6G-PE (BioLegend, 127608, clone 1A8), Sca1-BUV395 (BD Biosciences, 563990, clone D7), TLR4-BV786 (BD Biosciences, 741015, clone MTS510). Streptavidin-BV650 (BioLegend, 405231) was included at 1:500.

Secondary staining was performed with Streptavidin-BV650 (Biolegend). Cells were analysed in a SymphonyA4 Flow Cytometer. The data were analysed using FlowJo v.10 software. FlowAI[53] was used for quality control of flow data, followed by dimensionality reduction using the UMAP_R plugin[54]. Initial clusterization was performed with FlowSOM[55] and ClusterExplorerPlugin, and UMAP parameters were embedded in each sample for statistical analysis of neutrophil phenotypes.

RNA isolation, reverse transcription PCR

Total RNA was prepared with the RNA Extraction RNeasy Plus Mini-kit (QIAGEN) and RNA was reverse-transcribed with the High-Capacity cDNA Reverse Transcription kit (Applied Biosystems) according to the manufacturer's protocol. Real-time quantitative PCR (SYBR-green, Applied Biosystems) assays were performed with an Applied Biosystems 7900HT Fast Real-Time PCR System sequencer detector. Expression was normalized to the expression of the *36b4* housekeeping gene. Primer sequences are as follows: *36b4*: forward 5′-ACTGGTCTAGGACCCGAGAAG-3′, reverse 5′- TCCCACCTTGTCTCCAGTCT-3′; *Ptgs2*: forward 5′-TGAGCAACTATTCCAAACCAGC-3′, reverse 5′-GCACGTAGTCTTCGATCACTATC-3′; *Nr4a1*: forward 5′-TTGAGTTCGGCAAGCCTACC-3′, reverse 5′-GTGTACCCGTCCATGAAGGTG-3′; *Il1b*: forward 5′-AGTGAGGAGAATGACCTGTTC-3′, reverse 5′-CGAGATGCTGCTGTGAGATT-3′; *Tnfaip3*: forward 5′-GAACAGCGATCAGGCCAGG-3′, reverse 5′-GGACAGTTGGGTGTCTCACATT-3′; *Cebpe*: forward 5′-GCAGCCACTTGAGTTCTCAGG-3′, reverse 5′GATGTAGGCGGAGAGGTCGAT-3′; *Ltf*: forward 5′-TGAGGCCCTTGGACTCTGT-3′, reverse 5′-ACCCACTTTTCTCATCTCGTTC-3′.

Functional assays

T cell cytotoxicity assay. B16F10–OVA-GFP (10^{4} cells) were seeded in 96-well culture dishes for 24 h, in RMPI medium with glutamine (Thermofisher) containing 10% heat-inactivated FBS (Thermofisher), 100 μg ml^{-1} penicillin/streptomycin (Thomas Sci); 200 nM glutamine, 1% non-essential amino acids (MEM amino acids; Gibco), 1% sodium pyruvate (Gibco) and 0.01% β-mercaptoethanol (Gibco). Neutrophils from sorting or in vitro cultures were co-culture at a 2:1 ratio with SIINFEKL-activated OT-1 T effector cells for 3 h. Neutrophil-OT-I cells were then seeded on top of B16F10-OVAGFP target cells 1:2 ratio. After 24 h, live cells were stained with 0.4 g l^{-1} crystal violet (Sigma-Aldrich, HT90132). The area covered by target cells was quantified from micrographs of the plates using the ImageJ software.

In vivo Matrigel plug assay. Fifty thousand neutrophils sorted from tissues of interest were resuspended in 500 μl of growth-factor-depleted Matrigel (Corning) and injected subcutaneously in the lower back of anaesthetized mice to form plugs. At days 3 and 7 after implantation, the same number of sorted neutrophils was resuspended in 50 μl of PBS and injected directly into the plug respectively. On day 9 after implantation, Doppler laser perfusion imaging was performed at the lower back region that contained the Matrigel plugs. One ROI was defined for each observable Matrigel plug, and the amount of flux variation in each ROI was quantified. Only ROIs that were not obscured by hair regrowth were used.

Chemotaxis assay. Chemotaxis assays were performed as described[47]. In brief, bone marrow neutrophils were plated in 6.5 mm polycarbonate transwells with 5-mm pores (Corning) in RPMI medium 48 h after cytokine treatment. 20 ng ml^{-1} CXCL1 (R&D) was added to the bottom well. Transwells were incubated for 2 h at 37 °C and transmigrated cells were collected from the bottom well and stained for cytometric analysis. The number of transmigrated cells was assessed by the presence of a known number of Truecount beads (BD Biosciences).

3D Doppler imaging of tumour vascularization. Subcutaneous LLC tumour vascularization was imaged using Vevo Imaging Systems once they reached 500 mm^{3}. In brief, mice were anaesthetized in an isoflurane vapourizer chamber, and the backs were thoroughly shaved. The mice were placed in the imaging platform and images were captured using the power colour Doppler-3D mode. A total of 100 images were captured to generate a 3D reconstruction of the vasculature. Vevo LAB software was used to calculate the Volume and per cent vascularization of tumours. Per cent vascularization is determined by calculating the percentage of pixels in the volume that have a power Doppler signal associated with them, the presence of this signal indicates the presence of blood flow.

NET formation assay. Forty-eight hours after cytokine treatment, 5×10^{4} bone marrow neutrophils were plated with RPMI medium on poly-L-lysine-covered 8-well μ-Slides (Ibidi), and left 30 min to adhere. Subsequently, cells were incubated for 2 h with 100 nM PMA or vehicle. Cells were then fixed using 4% PFA for 10 min, permeabilized with PBS with 0.1% Triton X-100, 1% goat serum plus 5% BSA and stained with antibodies against cit-H3, DNA (Sytox-green, Molecular Probes) and MPO. Whole-slide *z*-stack tilescan images were acquired with a Leica

SP5 confocal microscope, and analysed using Imaris software (v.9.5, Bitplane)[47].

Bacterial killing assay. Forty-eight hours after cytokine treatment, bone marrow neutrophils were resuspended in fresh medium along with live *S. aureus* (ATCC) that were grown in tryptic soy broth. For the in vitro assays, neutrophils and bacteria (10^4 CFU in 200 µl) were incubated at 37 °C for 60 min. The cells are then plated onto tryptic soy plates in a serial dilution. Bacterial colonies on the plates were counted the following day.

Phagocytosis assay. Forty-eight hours after cytokine treatment, bone marrow neutrophils were resuspended in fresh medium along with fluorescent latex beads (SIGMA) followed by flow cytometric analyses.

Analysis of human neutrophils

Isolation and expansion of human bone marrow CD34$^+$ HSPCs. Bone marrow samples were obtained from healthy donors under informed consent approved by the ethics committee of the University Hospital Tübingen. CD34$^+$ haematopoietic stem and progenitor cells (HSPCs) were isolated through Ficoll gradient centrifugation followed by magnetic bead-based separation using the EasySep Human CD34$^+$ Cell Selection Kit II (Stem Cell Technologies, 17856). CD34$^+$ cells ($n = 4$; purity 95.4 ± 1.9%) were cultured at a density of 5×10^5 cells per ml in StemSpan SFEM II haematopoietic stem cell medium (Stem Cell Technologies, 09655), supplemented with 1% penicillin/streptomycin, 20 ng ml^{-1} IL-3, 20 ng ml^{-1} IL-6, 20 ng ml^{-1} TPO, 50 ng ml^{-1} SCF and 50 ng ml^{-1} FLT-3L (all cytokines purchased from R&D Systems). Cells were cultured under standard conditions (37 °C, 5% CO_2) and frozen for future use.

For granulocytic differentiation in vitro, cells were seeded at a density of 2×10^5 cells per ml. During the first 8 days of differentiation (days 0–7), cells were maintained in a myeloid cell expansion medium—RPMI 1640 supplemented with 10% FCS, 1% penicillin/streptomycin, 5 ng ml^{-1} SCF, 5 ng ml^{-1} IL-3 and 1 ng ml^{-1} G-CSF. The medium was changed every two days. On day 8 of culture, the medium was replaced with a granulocytic cell differentiation medium (RPMI 1640 supplemented with 10% FCS, 1% penicillin/streptomycin and 1 ng ml^{-1} G-CSF). The medium was changed every 2 days until day 14. On day 13 of differentiation, cells were collected and counted. 800,000 cells were lysed for RNA isolation, 50,000 cells for FACS, and 40,000 cells for cytospins. The remaining cells were resuspended in fresh granulocytic differentiation medium at a seed density of 2×10^5 cells per ml and divided into 4 groups. Group one was maintained in granulocytic differentiation medium, group two was treated with 10 ng ml^{-1} TGFβ, group three was treated with 10 ng ml^{-1} IFNβ (refreshed after 24 h), and group 4 was treated with 10 ng ml^{-1} GM-CSF. RNA-seq analyses were performed 48 h after stimulation.

HOXB8 cell cultures and differentiation. HOXB8-immortalized myeloid progenitors were routinely tested for mycoplasma contamination and cultured in RPMI 1640 medium supplemented with 10% fetal calf serum (FCS), 10 µM β-mercaptoethanol (Thermo Fisher Scientific), 4% supernatant from SCF-producing CHO cells, 1% penicillin/streptomycin and 1 µM β-oestradiol (Sigma-Aldrich) to maintain the progenitor state. Neutrophil differentiation was initiated by β-oestradiol withdrawal and continued culture in medium supplemented with 1% SCF-containing supernatant. Differentiation into neutrophils was achieved by culturing cells in RPMI 1640 medium containing 10% FCS, 30 µM β-mercaptoethanol, 4% SCF supernatant, and 20 ng ml^{-1} granulocyte colony-stimulating factor (G-CSF) under standard tissue culture conditions (37 °C, 5% CO_2).

CRISPR–Cas9-mediated knockout. Knockouts of selected transcription factors in HOXB8 progenitors have been previously described[21]. In brief, HOXB8 progenitors were transduced with lentiCas9-v2 lentiviral vectors encoding guide RNAs (gRNAs) targeting the following genes and exons: *Cebpb* (exon 1; gRNA: AGGCTCACGTAACCGTAGT); *Klf6* (exon 1; gRNA: TCGCTGTCGGGAAAACAGGG); *Runx1* (exon 3; gRNA: TAGCGAGATTCAACGACCTC); *Rfx2* (exon 5; gRNA: CTGCTGGGGGCGTAAAGCTG); *Relb* (exon 4; gRNA: CTGCACGGACGGCGTCTGCA); *Irf5* (exon 2; gRNA: ACCCTGGCGCCATGCCACGAGG); and *Junb* (exon 1; gRNA: GGAACCGCAGACCGTACCGG).

JUNB overexpression. Lentiviral vectors for JUNB overexpression were generated by transient transfection of HEK293T cells using the calcium phosphate precipitation method. Cells were co-transfected with: (1) a transfer plasmid containing the *Junb* cDNA under the control of the human PGK promoter; (2) packaging plasmid psPax2; and (3) envelope plasmid pMD2.G encoding VSV-G. The medium was replaced 24 h after transfection. At 72 h, virus-containing supernatant was collected, clarified by centrifugation (2,000 rpm, 5 min, 4 °C), filtered (0.45 µm), and concentrated via ultracentrifugation (26,000 rpm, 2 h, 4 °C). Viral pellets were resuspended in cold PBS, aliquoted, and stored at −80 °C.

Lentiviral transduction of HOXB8. HOXB8 progenitors were transduced by spinoculation. In brief, 5×10^5 cells were plated per well in 6-well plates with 1 ml of medium. Lentiviral particles were added at a multiplicity of infection (MOI) of 11.24 for the vector pRRL-hPGK-JUNB-IRES-eGFP and MOI = 1.8 for the pRRL-hPGK-IRES-eGFP empty vector, and cells were centrifuged at 1,000*g* for 90 min at 30 °C. Following transduction, cells were collected, washed, and resuspended in fresh culture medium at a final concentration of 5×10^4 cells per ml.

Plasmid construction. To construct the JUNB expression vector, the human PGK (hPGK) promoter was PCR-amplified with ClaI and XbaI restriction sites and cloned into the ClaI/XbaI sites of the pRRL-CMV-IRES-eGFP vector, replacing the CMV promoter. The *Junb* coding sequence was amplified from mouse cDNA using primers containing BglII and XhoI sites and inserted into the BamHI and XhoI sites of the modified vector. Cloning was performed using the following primers: hPGK forward (ClaI): 5′-TTTTTTATCGATGGGTAGGGGAGGCGCTTT-3′; hPGK reverse (XbaI): 5′-TTTTTTTTAGACGAAAGGCCCGGAGATGA-3′; *Junb* forward (BglII): 5′-TTTTTTAGATCTGCCACCATGTGCACGAAAATGGAACA-3′; *Junb* reverse (XhoI): 5′-TTTTTTCTCGAGTCAGAAGGCGTGTCCCTT-3.

Culture of HOXB8 cells. For the flow cytometry and bulk RNA-sequencing experiments, HOXB8 progenitors at day 3.5 of differentiation were seeded in 96-well plates at a density of 50,000 cells per well. Cells were cultured in complete RPMI medium (vehicle) or treated with GM-CSF (10 ng ml^{-1}) for 48 h, following the same conditions described for primary bone marrow neutrophil cultures. Vehicle or GM-CSF treated cells were collected at 48 h after treatment for the analysis.

Bulk RNA sequencing of mice and human-derived neutrophils

RNA from isolated mouse neutrophils was extracted using RNAeasy micro kit (Quiagen). RNA quality was checked using capillary electrophoresis (Agilent). Samples were submitted for whole RNA next generation sequencing in the Genomics Unit of CNIC. Total RNA (200 ng) was used to generate barcoded RNA-sequencing libraries using the NEBNext Ultra RNA Library preparation kit (New England Biolabs). Libraries were sequenced with HiSeq2500 (Illumina) to generate 50-nucleotide single reads, with a minimum of 8 million reads per sample. For RNA-seq of human-derived neutrophils, we isolated RNA from a total of 800,000 differentiated neutrophils collected on day 13 and 15. We used the NucleoSpin RNA Mini Kit (Macherey-Nagel, 740955.50), following the manufacturer's instructions. RNA concentration was assessed with Qubit 2.0 (Thermo Fisher), and a total of 400 ng RNA was sequenced. RNA integrity was assessed using Agilent Bioanalyzer 2100, with RNA integrity number (RIN) between 9.8 and 10.0. RNA samples were processed by Novogene for library preparation and sequencing, and all samples passed the quality control criteria. Strand-specific libraries were generated on the basis of Novogene's standard protocol. Samples were sequenced on an Illumina platform to produce 150 bp pairwise reads (PE150) per sample.

FastQ files for each sample were obtained using CASAVA (v.1.8) software (Illumina). Reads were further processed with RTA (v.1.18.66.3). FastQ files for each sample were obtained using bcl2fastq (v.2.20.0.422) software (Illumina). Sequencing reads were further processed as follows: Illumina adapters were trimmed and low-quality reads removed with Cutadapt (v.4.9)[56] (mismatch rate = 1 mismatch every 10 bp, overlap = 5 bp, minimum read length = 30 bp). Quality control of the processed reads was done with fastQC (v.0.12.1). RSEM (v.1.3.1) was used to quantify expression levels against the mouse genome reference GRCm38 or the human genome reference GRCh38, depending on the analysis[57] (default options). The processing of the counts and differential expression analysis was performed using limma (v.3.32.2)[58] and EdgeR (v.3.20.1)[59]) which were also used to perform pairwise differential expression analyses. To identify genes whose expression significantly varies across conditions, we applied a Likelihood Ratio Test (LRT) using DESeq2 (v.1.30.1)[60], allowing the detection of global effects of a factor without the need to specify individual contrasts. The resulting significant genes were then clustered using the *k*-means algorithm from the stats package (v.4.0.3).

Single-cell transcriptomics on mouse neutrophils

scRNA-seq of sorted tissue neutrophils. For single-cell analysis, all samples were collected between ZT1 and ZT5. Tissues were dissected and dissociated into a single-cell suspension by enzyme digestion. The resulting suspensions were filtered through cell strainers, and sorted in BD Aria Cell Sorter as DAPI$^-$CD11b$^+$LY6G$^+$ cells, and loaded into a BD Rhapsody cartridge. For the generation of single-cell whole-transcriptomes, we used a BD Rhapsody system according to the manufacturer's instructions. In brief, cell suspensions from each condition were incubated with Sample Tags (BD) for 20 min at room temperature. Cells were then washed three times and pooled in a single tube. Cell viability and concentration were assessed using a Countess III cell counter (Thermo Fisher). Sixty thousand cells were loaded into a Rhapsody Single Cell Analysis System cartridge. Cell capture and cDNA synthesis were performed according to manufacturer's instructions; cells were isolated into nanowells by gravity, then cells were lysed and mRNAs together with sample tags oligonucleotides were released and captured by the beads present in the nanowells. Each bead contained a unique oligonucleotide named 'cell label' to identify each individual bead. All beads present in the cartridge were collected and cDNA synthesis took place in a single reaction. At this point, each cDNA and Sample Tag oligonucleotide were attached to its corresponding cell label oligonucleotide. Two separated indexed libraries were prepared for whole-transcriptome analysis and sample tag demultiplexing following the manufacturer's instructions. The average size of the libraries was calculated using the 2100 Bioanalyzer (Agilent), and the concentration was determined using the Qubit fluorometer (Thermofisher). Finally, libraries were combined and sequenced together in a paired-end run (60 × 42) using a NextSeq 2000 system (Illumina) and a P2 flow cell. Output files were processed with NextSeq 1000/2000 Control Software Suite v.1.4.1. FastQ files for each sample were obtained using BCL Convert v.3.6.3 software (Illumina).

Construction of NeuMap and projection of external data. Rhapsody analysis pipeline v.1.9.1 was run locally. This pipeline includes steps for, alignment to mouse genome reference (GRCm38 with the gencodevM19-20181206) quantification and filtering of low-quality cells and tagging of doublets, which were also filtered out of the downstream analyses[61]. After BD Rhapsody's pipeline automatic quality filtering, a second round was performed manually, where cells with a mitochondrial content over 20% or with over 300 total gene counts were discarded. Cell Annotation was performed using R package SingleR and the Immgen database for each dataset individually. All subsequent downstream analyses were implemented using R (v.4.0.3) and the package Seurat (v.4.0.5)[61]. The Seurat suite was used to integrate the neutrophils from all datasets using Seurat's integration implementation. This method uses common sources of variation across the different datasets and aligns the cells so those in similar biological states cluster together. The integrated dataset was used to perform the unbiased cluster analysis and the construction of NeuMap. Additionally, we used the integrated NeuMap to generate a reference which we later used to analyse additional and external datasets by projecting cells onto our reference and annotate the new data using our custom labels using Seurat's MapQuery and TransferData. This method is technology agnostic, so we could reliably project cells from external datasets sequenced in different platforms onto NeuMap[62,63].

Definition of hubs. Functional hubs were selected by performing unbiased clustering at different resolutions using Seurat's function FindClusters(). Resolutions used ranged between 0.05 and 0.3. Clusters from different resolutions were selected because they best represented the expression of functional signatures projected onto NeuMap. Areas shown in the figures correspond to the q15 quantile of the KMASS algorithm, which calculates the density of cells in specific areas. For clarity, hubs in figures are shown as the area with the accumulation of 85% of cells for each selected cluster/hub. Analyses were performed on the complete set of cells for each cluster or hub. The FindAllMarkers() function from Seurat was used to calculate DEGs across the hubs. Only genes detected in a minimum of 25% of the cells and with an average of at least 0.25-fold difference (log scale) between the groups in either of the groups were tested.

Kernel density estimation. The MASS R package (v.7.3.61) was used for two-dimensional kernel density estimation (K-mass score), with $n = 100$ grid points in each direction.

Signature projection. The signatures used for illustration of functional states are contained in Supplementary Table 2. All signatures were calculated by Seurat's AddModuleScore() function. We used two different sources for the functional signatures: (1) previous publications, for which we provide the whole list of genes reported and used in Supplementary Table 2; and (2) public databases such as gene ontology (GO) and gene set enrichment analysis (GSEA). In those cases the whole gene list from the functional category was tested. For signatures from human data, human genes were mapped to their corresponding mouse homologue to calculate the enrichment score using the Mouse Genome Informatics (MGI) database. We used Seurat R package (v.5.2.1) AddModuleScore() function to calculate the scores. To generate visualization heat maps across NeuMap hubs, we first calculated enrichment scores for each cell. Scores were then averaged by hub and scaled per signature for comparison. To assess whether gene signature scores significantly differed across NeuMap hubs, we applied the Kruskal–Wallis test to each signature, testing the null hypothesis that score distributions were identical across hubs. The resulting test statistics were compared to a chi-squared distribution, with degrees of freedom equal to the number of hubs minus one. To correct for multiple comparisons, we adjusted *P* values using the Benjamini–Hochberg false discovery rate method.

Velocyto analysis. The analysis of expression dynamics in scRNA-seq data was performed using velocyto (v.0.17.17)[24], a package that allows estimating RNA velocities distinguishing between spliced and unspliced mRNAs in standard scRNA-seq protocols. The command line tool in Python implementation was adapted to be able to work with BAM files generated by BD Rhapsody, using samtools[64] to format the files, mainly by removing all possible alignments with antibodies and renaming the

UMI barcode tag to 'UB' instead of 'MA'. Velocyto was then executed with default parameters and the GRCm38 reference genome with the gencodevM19-20181206 transcriptome annotation. After concatenation of the spliced and unspliced data from all experiments, the results were merged with the outputs from single-cell analyses performed with Seurat in R, and scVelo[65] was used for further processing. Pre-processing included gene selection by detection (the minimum number of both unspliced and spliced counts was set to 30), and by variability (keep 2,000 highly variable genes (HVGs)), normalization, and log1p transformation. First and second order moments were computed among 50 nearest neighbours in the principal component analysis (PCA) space using 30 components. Cell-based RNA velocities were estimated by modelling the transcriptional dynamics of splicing kinetics using the stochastic model available in scVelo. Finally, these velocities were projected onto the previously computed UMAP and visualized at the cellular level or as velocity vector fields through streamlines.

In some experiments we performed Pseudotime analysis. Samples were pre-processed using the standard Monocle3 pipeline. To address batch effects, samples were integrated using the Batchelor algorithm (v.1.20.0). Dimensionality reduction and clustering were performed within Monocle3 (v.1.3.7), and pseudotime values were computed for the integrated dataset. To evaluate the significance of differences in pseudotime values between Cre$^-$ control and *Tgfbr2*-mutant immature cells, we applied a non-parametric Wilcoxon rank-sum test with continuity correction ($W = 373{,}675$; P value = 0.005548).

Comparison of cell distribution in the different hubs. To test differences in how neutrophils are distributed in the different hubs, we classified cell hubs for both mutant and control samples on the basis of the k-nearest neighbours algorithm ($k = 5$) of the cells projected onto Neumap. The observed hub proportions were calculated for each sample, and differences were determined by subtracting the proportions in control from the proportions in mutant cells. To assess the statistical significance of these differences, we used a bootstrap approach. For this, we generated a null distribution of hub proportion differences by merging each control–mutant pair into a mixed population. From this combined dataset, 10,000 resampled pairs were drawn with replacement, matching the sample sizes of the original control and mutant datasets. The differences in hub proportions between the resampled mutant and control groups were then calculated. The null distributions for each hub were verified to have a mean of 0.0, as expected under the null hypothesis. Finally, P values for the observed differences were computed by determining the fraction of resampled differences that were as extreme as or more extreme than the observed differences. To estimate 95% confidence intervals, the quantiles corresponding to the 0.025 and 0.975 percentiles of the null distributions were calculated.

Single-cell multiome using Dogma-seq. To simultaneously profile chromatin accessibility and gene expression at single-cell resolution, we used the Chromium Next GEM Single Cell Multiome ATAC + Gene Expression platform (10x Genomics). We collected neutrophils from bone marrow, spleen and lung (dataset 1) and LLC and spleen with LPS (dataset 2) from 8-to-12-week-old C57BL/6 mouse healthy blood was sequenced in both datasets as a quality control reference. Single-cell suspensions were prepared as described above. After staining, cells were washed, resuspended in sorting buffer, and incubated with DAPI (NBP2311561, Novus Biologicals) for 15 min prior to sorting.

Live CD11b$^+$LY6G$^+$ neutrophils were sorted in equal proportions from each organ. Cells were then pooled and lysed in 100 µl of cold DIG lysis buffer (20 mM Tris-HCl, 150 mM NaCl, 3 mM $MgCl_2$, 0.005% digitonin, 2 U µl^{-1} RNase inhibitor) for 5 min on ice. Lysis was quenched with 1 ml of cold DIG wash buffer, followed by centrifugation at 500*g* for 5 min. Nuclei were resuspended in 100 µl of 10x Genomics Nuclei Buffer supplemented with 1 mM DTT (Sigma) and 2 U µl^{-1} RNase inhibitor (Roche) to a final concentration of 3,400 nuclei per µl. After additional washes and centrifugation, samples were processed for library preparation at the Yale Center for Genome Analysis.

Library construction was performed following the 10x Genomics protocol (Chromium Next GEM Multiome ATAC + GEX v.1.1, CG000338 rev. E). In brief, nuclei underwent transposition using the ATAC transposition mix and were loaded onto the Chromium Controller for GEM generation, barcoding, and reverse transcription. Separate libraries were constructed for ATAC and gene expression using standard amplification and indexing steps. Libraries were quantified using Bioanalyzer (Agilent) and Qubit (ThermoFisher), pooled, and sequenced on an Illumina NovaSeq 6000 platform (paired-end, 150 bp) with a target depth of 75 million reads per sample.

Data processing

Initial quality control and cell filtering. DNA accessibility and gene expression from each cell were analysed simultaneously using Seurat (v.4.0.5 and v.4.3)[61] and Signac (1.14.0)[66] R packages. Per cell quality control metrics were evaluated using the DNA accessibility, and transcriptional data were obtained. Cells that did not pass the following criteria were removed from downstream analysis: number of counts in the ATAC data 100 < (nCount_ATAC) < 100,000; number of counts in the gene expression data 100 < (nCount_RNA) < 5,000; number of genes in the gene expression data 100 < (nFeature_RNA) < 2,500; ratio of mono-nucleosomal to nucleosome-free fragments (nucleosome_signal) < 2; ratio of fragments centred at the transcription start site (TSS) to fragments in TSS-flanking regions > 1; percentage of mitochondrial gene expression < 5.

ATAC data annotation. R packages Signac (v.1.14.0) and Seurat (v.5.1.0) were used to analyse single-cell chromatin data and gene expression, respectively. Full genome sequences for *M. musculus* (mouse) were used as provided by UCSC (mm10, based on GRCm38.p6), and annotated using Ensembl *M. musculus*annotations v.79.

Cell-type identification and neutrophil subset classification. We used R package SingleR (v.2.8.0)[67] to annotate cell types against the ImmGen database[68]. Cells annotated as 'neutrophils' were subset and re-analysed by running a new round of FindVariableFeatures() in which outlier features were identified and ScaleData() to re-scale the expression of the neutrophil subset.

Mapping onto NeuMap. We used Seurat v.5.1. FindTransferAnchors() function to identify pairwise correspondences (anchors) between the reference and query datasets using the transcriptomics data. This function uses canonical correlation analysis and mutual nearest neighbours to identify cells with similar gene expression profiles across the two datasets. The top 2,000 variable features shared between the reference and query datasets were used for anchor identification.

The query dataset was mapped onto the NeuMap reference using the MapQuery() function. This step projected the query cells from the Dogma-seq into NeuMap embedding space, allowing direct comparison and visualization of the dogma cells relative to NeuMap. Hub annotations from NeuMap were transferred to the query dataset using the TransferData() function. This function predicts cell labels for each query cell on the basis of the similarity scores computed from the anchors. The predicted labels were assigned to the query dataset, enabling downstream analysis of chromatin state in cells from each hub. Additionally, we assessed the confidence scores provided by TransferData() for each predicted label, retaining only high-confidence predictions (predicted.id.score ≥ 0.7) for downstream analysis.

Merging of the datasets and peak calling. We created a common peak set, and quantified this peak set in each experiment using Signac (v.1.14.0) and GenomicRanges (v.1.58.0)[69] prior to merging the objects.

Once both datasets contained an assay with the same set of features, we used Seurat (v.5.2.1) R package to merge the datasets.

We used the Signac R package (v.1.14.0) to call peaks with the CallPeaks() function. The CallPeaks() function used MACS2 (v.2.2.9.1)[70] to run. Peaks were called for cells assigned to each hub separately. Only cells with a predicted.id.score ≥ 0.7 were retained for peak calling. Peaks on nonstandard chromosomes and in genomic blacklist regions were removed. After quality control and predicted score filtering 1,962 for dataset 1 and 8,155 neutrophils remained for dataset 2.

ATAC data processing. R package Signac (v.1.14.0) standard processing pipeline was applied to the combined data: term frequency-inverse document frequency normalization was applied via RunTFIDF(), top features were identified using FindTopFeatures() with a minimum cut-off of 5 and singular value decomposition was performed on the normalized data running RunSVD().

Differential peak analysis. Differential accessibility peaks were identified using FindAllMarkers(), considering only positive markers and a minimum percentage of cells expressing the feature (min.pct = 0.1). The closest genes to the differentially accessible peaks were annotated using the ClosestFeature(). The results were merged and filtered to retain significant peaks and marked for uniqueness.

Motif enrichment analysis. A position frequency matrix set was retrieved from the JASPAR2020 database via the homonim R package (v.0.99.10), filtering for vertebrate transcription factors in the CORE collection. Motif information was added to the dataset with the BSgenome.Mmusculus.UCSC.mm10 genome as reference. Enriched motifs in the differentially accessible peaks per hub were then identified.

Transcription factor activity. Chromatin accessibility variability analysis was performed using R package chromVAR (v.1.28.0)[71], with the BSgenome.Mmusculus.UCSC.mm10 genome as the reference. This step computes motif activity scores for each cell, representing the inferred transcription factor activity based on chromatin accessibility.

Single-cell transcriptomics on human neutrophils

Samples collection and processing. Human samples were collected in Renji Hospital, Shanghai, China, under the Renji Hospital Ethics Committee protocol KY2024-090-B, in accordance with the Declaration of Helsinki, following informed consent from all participants. Samples were collected from healthy donors, patients, or perfused organ donors. Specifically, healthy donor samples (bone marrow, peripheral blood and umbilical cord blood) were randomly collected without self-selection or recruitment bias. Other healthy tissues were obtained from anonymous acute-death donors without chronic inflammation to minimize the confounding effects of death shock on the organs. Systemic lupus erythematosus (SLE) patient samples (umbilical cord and peripheral blood) were randomly selected from pregnant patients with an active disease state (SLEPDAI > 5) and without other chronic inflammatory comorbidities.

Blood and bone marrow were collected in BD vacutainer K2E (EDTA) tubes (BD Healthcare, 367525) to prevent coagulation. Erythrocytes were lysed in 5–10 ml 1× red blood cells (RBC) lysis buffer (diluted from 10× BD Pharm Lyse, 555899) for 5 min for twice to deplete erythrocytes and then washed and re-suspension. Spleen, lung, omentum, mesentary fat, perirenal fat, liver, colon and rectum tissues were minced into small pieces and digested for 30 min at 37 °C in a mixture of collagenase IV (385 U ml^{-1}, Sigma) and DNase I (2.5 mg ml^{-1}, Sigma) and the samples were homogenized into single-cell suspension using syringe plungers and passed through 70-µm cell strainers (15-1070, BIOLOGIX). Then the samples were lysed in 2 ml 1× RBC lysis buffer (diluted from 10× BD Pharm Lyse, 555899) for 3 min to deplete erythrocytes and then washed and resuspended. Endometrium was cut into small pieces and enzymatically digested with the Tumor Dissociation Kit (130-095-929, Miltenyi Biotec). After digestion, the cell suspension was filtered through 70-µm cell strainers and subjected to a 3-min erythrocyte lysis with 2 ml 1× RBC lysis buffer, followed by washing and re-suspension. All single-cell suspensions were incubated with Fc-blocker (Human TruStain FcXTM, 422302, Biolegend) for 30 min on ice, then stained for 30 min at 4 °C in the dark with Fixable Viability Stain 700 (564997, BD Biosciences) (1:1,000), and the following antibodies: Anti-CD19-PE-Cy7 (clone HIB19, BioLegend, 302216; 1:200); anti-CD3-PE-Cy7 (clone HIT3a, BioLegend, 300316; 1:200); anti-CD45-APC-Cy7 (clone HI30, BioLegend, 304014; 1:200); anti-CD56-PE-Cy7 (clone 5.1H11, BioLegend, 362510; 1:200). All antibodies were used at 1:200 dilution unless otherwise indicated. After washing with FACS buffer, cells were sorted on a FACS Aria III cell sorter (BD Biosciences). After washing with FACS buffer, cells were sorted on a FACS Aria III cell sorter (BD Biosciences).

Library preparation. Single-cell suspensions were processed on the BD Rhapsody Express System (BD Biosciences). In brief, cells and beads were loaded onto the BD Rhapsody cartridge. Lysis, reverse transcription and exonuclease I digestion were performed using BD Rhapsody Enhanced Cartridge Reagent Kit (BD Bioscience, 664887) and the BD Rhapsody cDNA Kit (BD Bioscience, 633773). The whole-transcriptome libraries were prepared by following the BD Rhapsody single-cell whole-transcriptome amplification workflow with the BD Rhapsody WTA Amplification Kit (BD Bioscience, 633801), including random priming and extension (RPE), RPE amplification PCR and whole-transcriptome amplification index PCR. Libraries were quantified using a High Sensitivity DNA chip (Agilent) on a Bioanalyzer 2100 and the Qubit High Sensitivity DNA assay (Thermo Fisher Scientific) and then sequenced on a NovaSeq X Plus (Illumina). Raw sequencing data (.fqstq files) were processed with the BD Rhapsody analysis pipeline.

Data processing and cell annotation. Seurat v.5.2.1 package standard pipeline was used for the analysis of the single-cell data. The percentage of mitochondrial content was calculated and cell cycle gene expression scores were obtaned using the cell-cycle gene list by Tirosh et al.[72] and DAM stage genes[73] expression scores. Cells with a percentage of mitochondrial content over 20% were removed from downstream analysis. Likewise cells with a number of detected features below 300 were removed. Cells were manually annotated by selecting the clusters in each dataset with highest expression score for known neutrophil markers in different states as described[12,74].

Data integration. scRNA-seq datasets were integrated using the reciprocal principal component analysis (RPCA) method implemented in Seurat v.5.2.1 package. Data normalization and identification of variable features (n = 2,000) were performed independently for each dataset using variance stabilizing transformation. Integration anchors were identified using RPCA reduction with k.anchor=15, and datasets were integrated with k.weight=50. Principal component analysis was performed on the integrated data using the top 15 components for UMAP dimensionality reduction (seed = 42).

Gene module scoring and hub identification. We used Seurat v.5.2.1 AddScoreModules() to assess the activity of specific gene sets within cell clusters. Gene lists of interest shown here were obtained from public data and repositories (Supplementary Table 2), from ref. 18. For each gene list, we used AddModuleScore() to calculate the aggregated module score against a set of control genes with similar expression, thus ensuring the score was not biased by overall expression levels. To identify human to mouse hub similarities gene lists of interest were obtained from NeuMap hub gene lists. For each gene list, we used AddModuleScore() to calculate the aggregated module score against a set of control genes with similar expression. For all gene module scoring, we reduced the control gene parameter to 80 to ensure sufficient background correction while maintaining computational feasibility within the reduced gene number in the integrated dataset.

Clustering was performed using the Leiden algorithm at several resolution. Clusters with high expression of functional scores were selected as hubs, keeping only cells uniquely assigned to each specific cluster or hub. This approach led to the identification of six human NeuMap regions shown in Supplementary Fig. 4d. For visualization purposes, we used two-dimensional kernel density estimation on UMAP coordinates. For figure visualization, we calculated density values per hub using the kde2d function from the MASS R package ($n = 100$ grid points) (v.7.3.61), selected cells above the 80th percentile of density (top 20% most accumulated cells) to define core regions representative of each defined hub. The FindAllMarkers() function with default parameters from Seurat was used to calculate DEGs shown is Supplementary Table 4 across the human hubs. Spatial boundaries around these high-density regions were computed using the concaveman algorithm (v.1.1.0) to generate concave hull polygons that capture the geometric extent of each cell state cluster. For the stacked bars plots, all samples are downsampled to 1,000 cells for consistency with previous mouse NeuMap bars and comparability among samples with varying sizes.

Spatial transcriptomics using Visium OCT. Visualization of gene expression in naive lung ($n = 1$), tumour-bearing lungs ($n = 2$) and flu-infected lung ($n = 1$) was performed using the 10x Visium Spatial Gene Expression Kit (10x Genomics; PN1000184) following the manufacturer's protocol. The OCT blocks were cut using a cryostat (Leica; PN-CM1520) and first cuts were used for RNA extraction (Qiagen; PN-74034), and RNA quality was assessed using the Agilent RNA 6000 Pico chips (Agilent; PN- 5067-1513), ensuring a minimum RIN number of 7. Second, 10-µm sections were cut on the Visium Spatial Tissue Optimization Slide (PN-1000193) to assess optimal tissue permeabilization time. FInally, a 10-µm section was mounted on a Visium Spatial Gene Expression Slide and then stained for H&E staining and imaged using the NanoZoomer S210 (Hamamatsu; NP-C13239) to assess tissue morphology and quality. Following protocol instructions, the sections were then permeabilized for 18 min, then tissue was lysed, and reverse transcription was performed followed by second strand synthesis and cDNA denaturation. Spatially barcoded, full-length cDNAs were amplified by PCR for 16 and 17 cycles, depending on the initial concentration previously determined by qPCR. Indexed sequencing libraries were generated via end repair, A-tailing, adaptor ligation, and sample index PCR. Size distribution and concentration of full-length GEX libraries were verified on an Agilent Bioanalyzer High Sensitivity chip (Agilent). Finally, sequencing of GEX libraries was carried out on a NovaSeq 6000 sequencer (Illumina) aiming at approximately 40,000 pair-end reads per spot.

Data pre-processing. For the analysis of the spatial transcriptomic data, SpaceRanger software (10x Genomics, v.1.3.0) was used to map the sequenced reads, correct amplification bias and obtain the count matrix. The mouse genome (mm10) was used as the reference. The filtered feature expression matrices generated were then used as input for downstream analysis with Seurat[75] (v.4.4.0) in R (v.4.3.1).

Quality control and data normalization. To ensure quality of the data, spots not overlapping tissue were removed previously to the SpaceRanger mapping with the Loupe Browser software (10X Genomics). Quality metrics were calculated on a per-slide basis to preserve biological variability. Differences in total UMI across spots were adjusted by log-normalization using the NormalizeData() function from Seurat. This function divides the raw gene counts for each cell by the total counts of that cell and multiplies it by the scale factor (10,000), which is then log-normalized as log(1+x). Genes not expressed in any spot overlapping tissue were also removed.

Feature selection and dimensionality reduction. To annotate the distinct lung regions of each Visium slide, we used the FindVariableFeatures() function to extract the top 3,000 HVGs and capture major axes of biological variability. Data were then scaled with ScaleData() to *z*-score. Principal component analysis was performed, and the top 50 principal components were retained for subsequent analysis steps.

Clustering and annotation. To perform clustering, the FindNeighbors() function was applied together with the Leiden[76] community detection algorithm. Sample-specific resolutions were chosen, ranging from 0.2 to 0.6 in the function FindClusters(). Lastly, DEGs for each cluster were identified with FindAllMarkers() function and Wilcoxon rank-sum test. When needed, clusters showing high heterogeneity were sub clustered and markers re-calculated. Each region of the lungs was then annotated considering the DEGs together with the haematoxylin and eosin staining.

Downstream analysis. To estimate cell-type composition in each spatial transcriptomic spot, we performed deconvolution using a single-cell reference dataset from the LungMap project[62], using the seeded non-negative matrix factorization (NMF) regression approach implemented in SPOTlight (v.1.0.3)[77]. Spots with a predicted composition of neutrophils of ≥10% were annotated as neutrophil-enriched.

Signature scoring was performed using decoupleR[78] (v.2.8.0). In brief, the univariate linear model (ulm) approach was applied to compute similarity (enrichment) scores by testing the association between gene expression and the neutrophil hub signatures derived from our single-cell RNA-seq data, thereby quantifying signature activity within each Visium spatial transcriptomics spot.

To map neutrophil signatures from the spatial transcriptomic data onto NeuMap, we first carried out differential expression analysis across healthy, flu-infected, and cancer samples using the FindAllMarkers() function in Seurat (v.4.3), with a logistic regression framework. Genes were included if expressed in at least 25% of cells in one group and showed a minimum log-fold change of 0.25. Significance was defined by adjusted *P* values (Benjamini–Hochberg correction) with a threshold of $P \leq 0.05$.

The top 50 significantly DEGs (ranked by $\log_2$ fold change) were selected for module scoring using Seurat's AddModuleScore() function. For each gene set, a module score was computed by averaging expression levels and comparing against a background of control genes with matched expression, thereby controlling for overall expression bias.

Analyses of PDAC and myocardial infarction (MI) models. Spatial transcriptomic data were analysed for the PDAC and MI mouse datasets[7,23] and used the Seurat package (v.5.1.0) in R, with three biological replicates included for each condition. Raw count matrices were first filtered to remove unexpressed genes. Low-quality spots were excluded on the basis of thresholds for the number of detected genes, total UMI counts, and mitochondrial gene content. Spots with abnormally low or high total counts, low gene detection, or mitochondrial percentages exceeding dataset-specific thresholds were considered low quality and discarded. We normalized using SCTransform[79,80]. Highly variable features were identified using the FindVariableFeatures() function, selecting the top 10% of genes by variability within each dataset. Data were then scaled using ScaleData() to centre gene expression values and apply *z*-score transformation. Dimensionality reduction was performed using PCA via RunPCA() on the selected HVGs. Neighbourhood graphs were constructed with FindNeighbors() on the basis of the first 20 principal components, followed by clustering with the Leiden algorithm and a resolution parameter set to 0.5 using FindClusters(). Low-quality clusters lacking underlying tissue structure were identified and removed. UMAP embeddings were computed on the same 20 principal components using RunUMAP() for visualization.

For single-cell referencing, we used a publicly available dataset (GSE141017and GSE176092)[23,80]. Quality control was applied by removing unexpressed genes and low-quality cells on the basis of gene counts, UMI counts, and mitochondrial gene content. The dataset was normalized using SCTransform, followed by identification of HVGs (top 10%), scaling, and PCA using 30 (MI) to 40 (PDAC) components. Batch correction across samples was performed using FindIntegrationAnchors() and IntegrateData(). Clustering was performed with the Leiden algorithm (resolution = 0.5) after computing neighbours using the top 30–40 principal components. UMAP was used for visualization. We annotated cell-type identities using SingleR (v.2.6.0) with reference profiles from the MouseRNAseq ImmGen databases via the celldex package (v.1.14.0) and curated marker genes from the dataset's own clustering results. Marker genes for each cell type were extracted using FindAllMarkers(). Cell-type-specific markers were used in subsequent annotation and deconvolution steps. Cell-type deconvolution of spatial transcriptomic data were conducted using the SPOTlight package (v.1.0.3), using a seeded NMF regression approach. Spots with neutrophil compositions of 10% or higher were labelled accordingly.

For neutrophil hub signature scoring and subtype analysis, we identified the top 15 marker genes for each hub, and module scores were calculated using AddModuleScore(). Seeded K-means clustering ($K = 7$) was performed on neutrophil-labelled spots using the hub marker signatures. Clusters were annotated on the basis of the most specific and abundant signature. Clusters with no dominant signature were left unclassified. This procedure was repeated for macrophage and T cell subtype signatures[81,82]. For MI-associated fibroblasts[83], a different strategy was used by classifying the cell subtypes in the reference single-cell dataset and predicting their respective abundances directly via deconvolution. Spatial annotations were derived by integrating information from the Leiden clusters, cell-type deconvolution, histological inspection, and expression of cancer-specific signatures. GSEA and over-representation analyses were used to characterize and differentiate distinct tumour cores. Finally, to investigate spatial relationships between spots, we constructed a graph using the igraph::graph() function (v.2.1.4) on the basis of a distance matrix computed from spot coordinates (stats::dist()). The graph was tuned to include only immediate neighbours on the basis of the 2D spatial grid structure.

Spatial analysis of human lung specimens using Visium HD. Human tissue microarray samples were used under protocol 2019-5253, which was reviewed and approved by the McGill University Health Centre (MUHC) Research Ethics Board, specifically by the MUHC co-Chair of the Comité d'éthique de la recherche du CTGQ panel. Human lung tissue specimens were obtained through protocols approved by the McGill University Health Centre Institutional Review Board (IRB 2014-1119). From these samples, tissue microarrays were constructed by a pathologist on the basis of intratumoural neutrophil abundance, using 1-mm cores sampled from FFPE pulmonary invasive adenocarcinomas with high-grade predominant solid architecture and adjacent non-tumorous lung tissue. Samples were derived from eight patients. Sections (5 μm) were mounted onto Visium CytAssist HD slides (10x Genomics) and processed following the manufacturer's protocol. In brief, FFPE tissue sections underwent deparaffinization, decrosslinking, probe hybridization, ligation and extension, followed by spatial barcoding and sample indexing. Final library quality and fragment size were assessed using an Agilent Bioanalyzer High Sensitivity chip. Libraries were sequenced at the McGill University Genome Centre on an Illumina NovaSeq X Plus platform (1.5B reads, PE100 per lane). Spatial gene expression data were processed using Space Ranger (10x Genomics), and high-resolution spatial transcriptomic profiles were generated for downstream analysis.

FASTQ files from the Visium HD experiment were mapped to the GRCh38-2020-A reference genome using the Visium_Human_Transcriptome_Probe_Set_v2.0_GRCh38-2020-A probe set with Space Ranger (v.3.1.1, 10x Genomics). Sample areas were manually selected using Loupe Browser, and the registration file H1-RTF6MBB-A1-fiducials-image-registration.json was provided to spaceranger count via the --loupe-alignment argument. High-resolution H&E and CytAssist images were passed with the --image and --cytaimage arguments, respectively.

Cell-level transcriptomic profiles were reconstructed using the Bin2cell package[84] (v.0.3.2). First, an AnnData object was created with b2c.read_visium, then filtered to retain bins with at least one count and genes expressed in at least three spots (min_counts = 1, min_cells = 3). The H&E image was scaled using b2c.scaled_he_image with mpp = 0.38. Due to variability in bin sizing across the array, 2 μm bins exhibit slight differences in width/height, leading to a striped appearance. To correct this artefact, the b2c.destripe function was applied. Nuclei segmentation was then performed on the H&E using b2c.stardist with parameters: stardist_model = "2D_versatile_he", prob_thresh = 0.1, and nms_thresh = 0.1. Segmented nuclei were expanded using b2c.expand_labels with algorithm = "volume_ratio". To recover additional cells not segmented via H&E, the Stardist fluorescence model was applied to a σ-smoothed gene expression image generated using b2c.grid_image (mpp = 0.38, sigma = 5). b2c.stardist was re-run with stardist_model = "2D_versatile_fluo" and the same thresholds. Cells not segmented with the H&E-based model were assigned secondary labels from the fluorescence model. Finally, bins were grouped into cells with the b2c.bin_to_cell function. To reconstruct the Segmentation Polygon Mask we converted the.npz mask output from Bin2cell into a data frame using pd.DataFrame.from_dict (pandas v.2.2.3). This file was then processed in R (v.4.4.1) using the concaveman package (v.1.1.0) to generate cell polygons for visualization.

SingleCellExperiment[85] objects were created in R by importing the Bin2cell.h5ad files with the h5ad2sce function from the schard package (v.0.0.1). Low-quality cells were removed if they met any of the following criteria: fewer than 10 counts, fewer than 10 unique genes, area <8 μm^2, or >15% mitochondrial reads. Additionally, cells labelled only through gene expression segmentation (secondary labels) were excluded upon manual inspection for falling outside tissue boundaries. In a second quality control step, the isOutlier function from the scuttle package (v.1.16.0) was used to flag outliers in transcript count and transcript density ($\log_2$(counts/area)) using parameters nmads = 2.5, type = "both", and log = FALSE. Identified outliers were excluded from downstream analysis. For pre-processing, quality-filtered SingleCellExperiment objects were normalized using logNormCounts from scuttle. HVGs were identified with modelGeneVar (scran[6] v.1.34.0), blocking by patient ID (block = sce$patient). HVGs were selected using getTopHVGs (fdr.threshold = 0.05). PCA was performed using runPCA (scater v.1.34.0)[86] on the HVGs (subset_row = hvgs), and the first 15 principal components were retained on the basis of elbow plot inspection. UMAP dimensionality reduction was computed using runUMAP (scater).

To cluster cells, we built a shared nearest-neighbour graph using buildSNNGraph from scran with type = "jaccard" and use.dimred = "PCA". Louvain community detection was performed using cluster_louvain (igraph[7] v.2.1.1) at multiple resolutions. DEGs between clusters were identified using findMarkers (scran) with direction = "up". Top-ranked markers for each cluster were selected from the 'Top' column of the results and inspected manually to guide spatial annotation. Hallmark gene sets (for example, angiogenesis, hypoxia) were obtained from MSigDB using the msigdbr package (v.7.5.1) with species = "Homo sapiens" and category = "H". Immune cell-type signatures[87] were retrieved using category = "C8" and filtered to retain adult lung signatures while excluding fetal profiles. Signature scoring was performed using AUCell (v.1.28.0). Gene expression rankings per cell were computed with AUCell_buildRankings, followed by AUC calculation with AUCell_calcAUC. For visualization, cluster-level mean AUC scores were obtained using aggregateAcrossCells (scuttle[86]) with statistics = "mean" and use.assay.type = "AUC".

To assign neutrophil clusters to NeuMap hubs, human gene signatures corresponding to spatial clusters C1–C5 were first converted to mouse orthologs using homology data from the Mouse Genome Informatics (MGI) database (https://informatics.jax.org). We then computed gene module scores for each hub using the AddModuleScore() function in Seurat. Module scores were calculated by averaging the expression of hub-associated genes and comparing them to control gene sets with similar expression levels, thereby normalizing for baseline expression and minimizing bias. For visualization, enrichment scores were averaged by hub across clusters and scaled per signature to enable comparison in the resulting heat map.

Neighbourhood analysis. Spatial transcriptomic data were analysed using Seurat (v.4.3) in R (v.4.2). A spatial proximity graph was constructed by computing the *k*-nearest neighbours ($k = 6$) from each spot's *x*,*y* coordinates using the RANN package (v.2.6.2). Edges exceeding 250 units in Euclidean distance were excluded to account for realistic cell–cell interaction radii. An undirected graph was generated using the igraph package, with edge weights corresponding to physical distances. We implemented two complementary functions to quantify spatial cell-type context: (1) neighbourhood frequency analysis. For a given set of target spots (for example, neutrophils), their first-order neighbours were identified within the spatial graph. For each neighbour, the cell-type label was extracted, the number of neighbouring cells of each type was counted per target spot and aggregated across all targets to calculate the mean and 95% confidence interval for each cell type. This allowed identification of the most frequently co-localized cell types around a given population. (2) neighbourhood composition by Hub: In a separate analysis, both the target spot and its neighbours were pooled to represent a local "neighbourhood." Cell types within each neighbourhood were classified using a curated cell-type annotation. For each neutrophil hub, cell-type counts were summed and normalized to percentages, excluding spots annotated as 'unassigned' to avoid skewing proportion estimates. This enabled comparative analysis of cellular composition across microenvironments.

MACSima imaging cyclic staining

Sample preparation and image acquisition. Multiplex immunohistochemistry of lungs from naive, flu-infected, or tumour-induced mice was performed using a MACSima imaging system (Miltenyi Biotec). In brief, cyclic immunofluorescence imaging consisting of repetitive cycles of immunofluorescent staining, sample washing, multi-field imaging, and signal erasure by photobleaching was performed. Cryosectioned fixated lungs from the 3 groups were placed on microscopy slides and MACSwell sample carriers were mounted and blocked using a blocking buffer containing 10% BSA and 2% goat serum for 1 h at room temperature before lungs were preincubated with an antibody to IFIT1 (ab236256, Abcam, 1:100) overnight at 4 °C. Thereafter, nuclei were counterstained with DAPI before samples were placed in the MACSima imaging system. Neutrophil subsets were identified using the following antibodies: anti-CD11b-APC (clone M1/70.15.11.5, Miltenyi Biotec, 130-113-239; 1:50); anti-CD45-FITC (clone REA737, Miltenyi Biotec, 130-110-658; 1:50); anti-CXCR2-PE (clone SA044G4, BioLegend, 149303; 1:50); anti-Ly6C-PE (clone REA796, Miltenyi Biotec, 130-111-916; 1:50); anti–MHC-II-APC (clone REA813, Miltenyi Biotec, 130-112-388; 1:50); anti-PD-L1-APC (clone 10 F.9G2, BioLegend, 124312; 1:50); anti-CD14-PE (clone Sa14-2, BioLegend, 150106; 1:50) Anti-IFIT1 (Polyclonal, Abcam, Ab70023; 1:50). Additionally, a conjugated anti-rabbit antibody (polyclonal, Sigma-Aldrich, F9887; 1:100) in the first cycle to identify IFIT1. The tissue location was characterized using anti-Podoplanin-PE (clone 8.1.1, BioLegend, 127408; 1:50).

Data analysis and visualization. Images were stitched and pre-processed using MACS iQ View Analysis Software (Miltenyi Biotec, v.1.3.2) and representative overlay pictures were displayed. For downstream analysis, cells were segmented on the basis of the DAPI signal using the StarDist plugin in ImageJ (US National Institutes of Health) and the donut algorithm in MACS iQ View. The segmented data were then exported for further analysis to FlowJo (BD Biosciences), where neutrophils were identified as LY6G$^{\mathrm{hi}}$ cells using a threshold value. In flu-infected lungs, neutrophils were characterized as intravascular or extravasated on the basis of the podoplanin signal in the segmented neutrophils. Neutrophils from all ROIs were concatenated and phenotypically analysed by dimensional reduction using the UMAP plugin and unsupervised clustering using the FlowSOM plugin. FlowJo and R were used for visualization.

Mathematical modelling for blood neutrophil diagnosis

To model the predictive value of the distribution of blood neutrophils in NeuMap, we used the density overlap represented by the Bhattacharyya index. We favoured density versus spatial overlap to reduce the impact of outliers in our calculations. We also favoured using ten selected regions of NeuMap over the seven hubs delineated in Fig. 1e to gain spatial resolution of cell distribution over the specific areas of NeuMap where blood neutrophils from the tested conditions tended to concentrate. In separate analyses, we found that the spatial overlap was not based on densities, and the use of seven hubs provided significantly less resolution in the overlap barcodes (not shown).

Density state estimation. The UMAP coordinates $\{x_j, y_j\}$ of the neutrophils collected from the tissue hubs and blood samples were pipelined into a computational approach to estimate the probability density functions (PDFs) over the Neumap transcriptomic space associated with these datasets. The kernel density estimators $\hat{f}(x,y)$ were of the form[88],

$$\hat{f}(x,y) = \frac{1}{nh_x h_y}\sum_{j=1}^{n} K\left(\frac{x_j - x}{h_x}\right) K\left(\frac{y_j - y}{h_y}\right),$$

where K is the Epanechnikov kernel

$$K(u) = \left\{\frac{3}{4}(1-u^2),\quad \text{for } |u| \le 1,\quad 0,\ \text{otherwise},\right.$$

with n, h_x and h_y denoting the number of points and the bandwidths along two orthogonal directions, respectively. This kernel choice, which is symmetric and normalized along each orthogonal direction, ensures a smooth, bounded and efficient computation of the density estimates. The determination of each kernel's bandwidths, which influences the smoothness and accuracy of the resulting PDF estimate, was made via the Sheather–Jones method[65]. This technique uses a data-driven approach that minimizes the mean integrated square error of the estimated density function. By iteratively adjusting the bandwidths h_x and h_y and evaluating their performance, Sheather–Jones effectively balances bias and variance, resulting in accurate density estimates, particularly for tissue hubs and blood samples that present non-Gaussian distributions or multimodality.

Overlap integration. Upon estimating the PDFs of our datasets, we assessed the degree of overlap between pairs of these functions. For this purpose, we used the Bhattacharyya index, which yields a measure of the amount of overlap between two PDFs $f(x,y)$ and $g(x,y)$. The Bhattacharyya index was defined by the integral expression

$$\mathrm{BC}(f,g) = \iint \sqrt{f(x,y)g(x,y)}\,\mathrm{d}x\mathrm{d}y,$$

where the double integral runs over the entire domain defined by NeuMap. The Bhattacharyya index gives a scalar value in the interval $[0,1]$, enabling a direct interpretation of the overlap: values near 1 suggest a high degree of similarity, or almost perfect overlap, between the two distributions, indicating that the neutrophil states are nearly indistinguishable within the dimensionally reduced transcriptomic space. Conversely, values near 0 denote little to no overlap, pointing to distinct neutrophil states with minimal similarity in their respective distributions within the dimensionally reduced transcriptomic space.

To calculate the Bhattacharyya index, we used an adaptive Monte Carlo method[89] that combines adaptive importance and stratified samplings over multiple iterations, thus optimizing the sample distribution around the peaks of the PDFs and thereby reducing the standard deviation in the estimates. This approach yielded accurate values of the multidimensional integrals and hence offered robust measures of the overlap between the PDFs. While the Bhattacharyya index does not constitute a true probability measure, its bounded nature makes it a valuable score for comparing the similarity of data distributions in a normalized manner. From the computed Bhattacharyya indexes, the resulting barcodes were generated. To perform our calculations, we used the R programming language to analyse all datasets. Specifically, we used the MASS, graphics, stats and vegas R packages.

Estimation of neutrophil lifetimes

To quantify the neutrophil half-lives and transit times, we used an age-structured mathematical model as previously proposed[1]. This model effectively captures the temporal variation in the proportion of labelled neutrophils following the administration of the BrdU pulse. Let $u = u(t, a)$ denote the density of neutrophils, which at time t, have an age a. We assume that their age ranges in the interval $a \in [0, a_{\max}]$, where $a_{\max}$ is the maximum age (or the maximum lifespan) a neutrophil can achieve in the different examined tissues. In practice, this age can be taken sufficiently large without appreciably altering the numerical results for the entire neutrophil population. To describe the temporal dynamics of the age distribution in neutrophils, we considered the following first-order linear transport partial differential equation

$$\frac{\partial u}{\partial t} + \frac{\partial u}{\partial a} = -\frac{u(t, a)}{\tau(a)} + \phi(t, a). \tag{1}$$

The left-hand side of equation (1) represents the temporal change in the number of neutrophils along with their corresponding age. The first term on the right-hand side accounts for neutrophil death. The death time, $\tau(a)$, generally depends on the age of the neutrophil. The introduction of a flux function, $\phi(t, a)$, encapsulates the net recruitment of neutrophils entering or leaving the target tissue. Assuming that at time $t = 0$ no BrdU$^+$-labelled neutrophils of any age have yet arrived at tissue i, the initial condition is $u(0, a) = 0$. Therefore, the exact solution to (1), obtained using the method of characteristics for first-order partial differential equations, is

$$u_i(t, a) = \mathrm{e}^{-\int_0^t \frac{\mathrm{d}\xi}{\tau_i(a-\xi)}} \int_0^t \phi_i(\xi, a - t + \xi)\mathrm{e}^{\int_0^\xi \frac{\mathrm{d}\eta}{\tau_i(a-t+\eta)}} \mathrm{d}\xi. \tag{2}$$

Equipped with equation (2), we computed the total number of neutrophils at time t and tissue i, irrespective of their age, via the following integral

$$n_i(t) = \int_0^{a_{\max}} u_i(t, a)\mathrm{d}a. \tag{3}$$

To connect equation (2) with the different scenarios addressed in the experiments, the net flux $\phi_i(t, a)$ corresponded to one synchronous wave of neutrophils after administration of the BrdU labelling. The chosen functional forms for $\tau_i(a)$ and $\phi_i(t, a)$ in our modelling were

$$\tau_i(a) = \tau_i, \quad \phi_i(t, a) = \alpha_i \mathrm{e}^{-\frac{(t-t_i)^2}{2\sigma_i^2}}, \tag{4}$$

where τ_i, α_i, t_i, and σ_i are constant parameters. Inserting equations (2) and (4) into equation (3), we arrive at the following exact formula for the total number of neutrophils at a given tissue i at time t

$$n_i(t) = m_i \mathrm{e}^{-\frac{t}{\tau_i}} \left[\mathrm{Erf}\left(\frac{\sigma_i^2 + t_i\tau_i}{\sqrt{2}\,\sigma_i\tau_i} \right) - \mathrm{Erf}\left(\frac{\sigma_i^2 + (t_i - t)\tau_i}{\sqrt{2}\,\sigma_i\tau_i} \right) \right], \tag{5}$$

where

$$m_i = \sqrt{\frac{\pi}{2}}\,\alpha_i\sigma_i a_{\max} \mathrm{e}^{\frac{\sigma_i^2 + 2t_i\tau_i}{2\tau_i^2}}, \tag{6}$$

is a normalization parameter for tissue i, and $\mathrm{Erf}(x) = \frac{2}{\sqrt{\pi}} \int_0^x \mathrm{e}^{-\xi^2} \mathrm{d}\xi$ is the error function. The parameters τ_i, m_i, t_i, and σ_i for blood, bone marrow and spleen were computed via a nonlinear regression analysis using the corresponding time series measured from day 1 to day 7 for each tissue compartment. Once these four parameters were found for each tissue i, the mean half-life time $t_{1/2}^{(i)}$ and transit time $t_{\mathrm{tran}}^{(i)}$ were estimated from the normalized profile (equation (5)). To do that, the transit time was identified as the time at which this unimodal profile achieves its maximum (100% of the BrdU-labelled neutrophils in tissue i). Subsequently, the 50% level was set as a reference for the mean half-life time $t_{1/2}^{(i)}$. The approach for calculating these two lifetimes is illustrated in Extended Data Fig. 7f. The bands shown in this figure correspond to a confidence level of 0.75.

To carry out the density state estimation and overlap integration, we used the R programming language to analyse all datasets. Specifically, we used the *MASS* v.7.3.61, graphics v.4.4.3, stats v.4.0.3 and v.4.4.3., and vegas v.2.1.4 R packages. The nonlinear regression and statistical analysis were performed with Matlab (R2024a) using the functions fitnlm and coefCI.

Quantification and statistical analysis

Data from experiments are represented as mean values ± s.e.m. All parameters analysed followed normal distribution as tested by D'Agostino–Pearson test unless indicated in the figure legend. Unpaired two-tailed *t*-test was used when two groups were compared, and comparison of more than two datasets was done using one-way analysis of variance (ANOVA) with Tukey's post-test or two-way ANOVA. Log-rank analysis was used for Kaplan–Meier survival curves. Statistical analysis was performed using GraphPad software. Statistics on the RNA sequencing are indicated in the analysis section. A *P* value below 0.05 (*) was considered statistically significant; $P \leq 0.01$ (**) and $P \leq 0.001$ (***), as well as nonsignificant differences (NS), are indicated accordingly.

Reporting summary

Further information on research design is available in the Nature Portfolio Reporting Summary linked to this article.

Data availability

All the transcriptomics data are available in Gene Expression Omnibus (GEO) as a Super-series GSE266680. Data used for the hNeuMap are available at the Chinese Academy of Sciences (https://ngdc.cncb.ac.cn/gsa-human/), with accession number HRA013413. The raw sequence data used to build the human NeuMap (Extended Data Fig. 4) have been deposited in the Genome Sequence Archive[90] in the National Genomics Data Center[91], China National Center for Bioinformation/Beijing Institute of Genomics, Chinese Academy of Sciences (GSA-Human: HRA013413). Source data are provided with this paper.

Code availability

Visualization and analysis of NeuMAP is available at the single-cell Data Analysis and Visualization (scDAVIS) web-based tool: https://bioinfo.cnic.es/scdavisr/.

41. Levéen, P. et al. Induced disruption of the transforming growth factor beta type II receptor gene in mice causes a lethal inflammatory disorder that is transplantable. *Blood*. **100**, 560–568 (2002).
42. Kenner, L. et al. Mice lacking JunB are osteopenic due to cell-autonomous osteoblast and osteoclast defects. *J. Cell Biol*. **164**, 613–623 (2004).
43. Croxford, A. L. et al. The cytokine GM-CSF drives the inflammatory signature of CCR2$^+$ monocytes and licenses autoimmunity. *Immunity* **43**, 502–514 (2015).
44. Prigge, J. R. et al. Type I IFNs act upon hematopoietic progenitors to protect and maintain hematopoiesis during pneumocystis lung infection in mice. *J. Immunol*. **195**, 5347–5357 (2015).
45. Leung, J. M. et al. Rapid environmental effects on gut nematode susceptibility in rewilded mice. *PLoS Biol*. **16**, e2004108 (2018).
46. Ariño, S. et al. Ductular reaction-associated neutrophils promote biliary epithelium proliferation in chronic liver disease. *J. Hepatol*. **79**, 1025–1036 (2023).
47. Adrover, J. M. et al. A neutrophil timer coordinates immune defense and vascular protection. *Immunity* **50**, 390–402.e10 (2019).
48. Ruscitti, F. et al. Longitudinal assessment of bleomycin-induced lung fibrosis by micro-CT correlates with histological evaluation in mice. *Multidiscip. Respir. Med*. **12**, 8 (2017).
49. Chassaing, B., Aitken, J. D., Malleshappa, M. & Vijay-Kumar, M. Dextran sulfate sodium (DSS)-induced colitis in mice. *Curr. Protoc. Immunol*. https://doi.org/10.1002/0471142735.im1525s104 (2014).
50. Zhang, J. et al. Endothelial lactate controls muscle regeneration from ischemia by inducing M2-like macrophage polarization. *Cell Metab*. **31**, 1136–1153.e7 (2020).
51. Fuster, J. J. et al. TET2-loss-of-function-driven clonal hematopoiesis exacerbates experimental insulin resistance in aging and obesity. *Cell Rep*. **33**, 108326 (2020).
52. Bjørklund, M. M. et al. Induction of atherosclerosis in mice and hamsters without germline genetic engineering. *Circ. Res*. **114**, 1684–1689 (2014).
53. Monaco, G., Chen, H., Poidinger, M., Chen, J., de Magalhães, J. P. & Larbi, A. flowAI: automatic and interactive anomaly discerning tools for flow cytometry data. *Bioinformatics* **32**, 2473–2480 (2016).
54. McInnes, L., Healy, J. & Melville, J. UMAP: uniform manifold approximation and projection for dimension reduction. *J. Open Source Softw*. **3**, 861 (2018).
55. Van Gassen, S. et al. FlowSOM: using self-organizing maps for visualization and interpretation of cytometry data. *Cytom. A* **87**, 636–645 (2015).
56. Martin, M. Cutadapt removes adapter sequences from high-throughput sequencing reads. *EMBnet J*. **17**, 10 (2011).
57. Li, B. & Dewey, C. N. RSEM: accurate transcript quantification from RNA-Seq data with or without a reference genome. *BMC Bioinformatics* **12**, 323 (2011).
58. Ritchie, M. E. et al. limma powers differential expression analyses for RNA-sequencing and microarray studies. *Nucleic Acids Res*. **43**, e47–e47 (2015).
59. Robinson, M. D., McCarthy, D. J. & Smyth, G. K. edgeR: a Bioconductor package for differential expression analysis of digital gene expression data. *Bioinformatics*. **26**, 139–140 (2010).
60. Love, M. I., Huber, W. & Anders, S. Moderated estimation of fold change and dispersion for RNA-seq data with DESeq2. *Genome Biol*. **15**, 550 (2014).
61. Hao, Y. et al. Integrated analysis of multimodal single-cell data. *Cell* **184**, 3573–3587.e29 (2021).
62. Guo, M. et al. Guided construction of single cell reference for human and mouse lung. *Nat. Commun*. **14**, 4566 (2023).
63. Waltman, L. & van Eck, N. J. A smart local moving algorithm for large-scale modularity-based community detection. *Eur. Phys. J. B* **86**, 471 (2013).
64. Danecek, P. Twelve years of SAMtools and BCFtools. *Gigascience* **10**, giab008 (2021).
65. Köhler, M., Schindler, A. & Sperlich, S. A review and comparison of bandwidth selection methods for kernel regression. *Int. Stat. Rev*. **82**, 243–274 (2014).
66. Stuart, T., Srivastava, A., Madad, S., Lareau, C. A. & Satija, R. Single-cell chromatin state analysis with Signac. *Nat. Methods* **18**, 1333–1341 (2021).
67. Aran, D. et al. Reference-based analysis of lung single-cell sequencing reveals a transitional profibrotic macrophage. *Nat. Immunol*. **20**, 163–172 (2019).
68. Heng, T. S. P. et al. The Immunological Genome Project: networks of gene expression in immune cells. *Nat. Immunol*. **9**, 1091–1094 (2008).
69. Lawrence, M. et al. Software for computing and annotating genomic ranges. *PLoS Comput. Biol*. **9**, e1003118 (2013).
70. Zhang, Y. et al. Model-based Analysis of ChIP–seq (MACS). *Genome Biol*. **9**, R137 (2008).
71. Schep, A. N., Wu, B., Buenrostro, J. D. & Greenleaf, W. J. chromVAR: inferring transcription-factor-associated accessibility from single-cell epigenomic data. *Nat. Methods* **14**, 975–978 (2017).
72. Tirosh, I. et al. Dissecting the multicellular ecosystem of metastatic melanoma by single-cell RNA-seq. *Science* **352**, 189–196 (2016).
73. Keren-Shaul, H. et al. A unique microglia type associated with restricting development of Alzheimer's disease. *Cell* **169**, 1276–1290.e17 (2017).
74. Montaldo, E. et al. Cellular and transcriptional dynamics of human neutrophils at steady state and upon stress. *Nat. Immunol*. **23**, 1470–1483 (2022).
75. Butler, A., Hoffman, P., Smibert, P., Papalexi, E. & Satija, R. Integrating single-cell transcriptomic data across different conditions, technologies, and species. *Nat. Biotechnol*. **36**, 411–420 (2018).
76. Traag, V. A., Waltman, L. & van Eck, N. J. From Louvain to Leiden: guaranteeing well-connected communities. *Sci. Rep*. **9**, 5233 (2019).
77. Elosua-Bayes, M., Nieto, P., Mereu, E., Gut, I. & Heyn, H. SPOTlight: seeded NMF regression to deconvolute spatial transcriptomics spots with single-cell transcriptomes. *Nucleic Acids Res*. **49**, e50–e50 (2021).
78. Badia-i-Mompel, P. et al. decoupleR: ensemble of computational methods to infer biological activities from omics data. *Bioinformatics Adv*. **2** vbac016 (2022).
79. Hafemeister, C. & Satija, R. Normalization and variance stabilization of single-cell RNA-seq data using regularized negative binomial regression. *Genome Biol*. **20**, 296 (2019).
80. Schlesinger, Y. et al. Single-cell transcriptomes of pancreatic preinvasive lesions and cancer reveal acinar metaplastic cells' heterogeneity. *Nat. Commun*. **11**, 4516 (2020).
81. Caronni, N. et al. IL-1β+ macrophages fuel pathogenic inflammation in pancreatic cancer. *Nature* **623**, 415–422 (2023).
82. Chu, Y. et al. Pan-cancer T cell atlas links a cellular stress response state to immunotherapy resistance. *Nat. Med*. **29**, 1550–1562 (2023).
83. Amrute, J. M. et al. Targeting immune–fibroblast cell communication in heart failure. *Nature* **635**, 423–433 (2024).
84. Polański, K. et al. Bin2cell reconstructs cells from high resolution visium HD data. *Bioinformatics* **40**, btae546 (2024).
85. Amezquita, R. A. et al. Orchestrating single-cell analysis with Bioconductor. *Nat. Methods* **17**, 137–145 (2020).
86. McCarthy, D. J., Campbell, K. R., Lun, A. T. L. & Wills, Q. F. Scater: pre-processing, quality control, normalization and visualization of single-cell RNA-seq data in R. *Bioinformatics* **33**, 1179–1186 (2017).
87. Travaglini, K. J. et al. A molecular cell atlas of the human lung from single-cell RNA sequencing. *Nature* **587**, 619–625 (2020).
88. Wilcox, R. R. *Introduction to Robust Estimation and Hypothesis* 5th edn (Academic Press, 2022).
89. Dunn, W. L. & Shultis, J. K. *Exploring Monte Carlo Methods* (Elsevier, 2022).
90. Chen, T. et al. The genome sequence archive family: toward explosive data growth and diverse data types. *Genomics Proteomics Bioinformatics* **19**, 578–583 (2021).
91. Xue, Y. et al. Database resources of the National Genomics Data Center, China National Center for Bioinformation in 2022. *Nucleic Acids Res*. **50**, D27–D38 (2022).
92. Hirschhorn, D. et al. T cell immunotherapies engage neutrophils to eliminate tumor antigen escape variants. *Cell* **186**, 1432–1447.e17 (2023).

Acknowledgements We thank all members of our laboratories for insightful feedback; E. Menet, Z. Zhao, E. Prieto, N.A Muñoz, R. Nieto and M. Vitón for help with sorting and cytometric analyses; L. Cabezuela and E. Santos for animal husbandry; V. Labrador, E. Arza and the Microscopy Unit of the CNIC for help with microscopy; L. Carramolino and J. Bentzon for providing plasmids encoding PCSK9; J. Li and H. Beach for help with data visualization; E. Wagner and N. Palm for the generous gift of mice; and The Thoracic Oncology Clinical Database and Biobank at the McGill University Health Centre for access to tissue and clinical data. L.G.N is supported by Chinese Ministry of Science and Technology grant 2023YFC2306300 and National Natural Science Fund of China grant 92374205, W2431020. D.C.-W. was supported by the Cancer Research Institute/Irvington Postdoctoral Fellowship (CRI CRI3511) and A.G.-C. was supported by a predoctoral grant from MCIN (PREP2022-000391). I.B. was supported by grants from MICIN (RYC2020-029563-I and PID2022-140534NB-I00) and the BBVA Foundation (Leonardo fellowship; LEO22-2-2596). A. Hidalgo was supported by the Worldwide Cancer Research foundation (Grant 23-0115) and 1RO1AI165661 from the US National Institutes of Health. D.G.A. is supported by contract 2023-CDT-11616 from a project with grant number TED2021-132296B-C55 funded by the Spanish MCIN/AEI/10.13039/501100011033. G.F.C. is supported by grants PID2022-142341OB-I00 funded by the Spanish MCIN/AEI/10.13039/501100011033 and European Union "NextGenerationEU/PRTR", and SBPLY/23/180225/000041 funded by Junta de Comunidades de Castilla-La Mancha, Spain, and European Regional Development Fund. O.S. receives support from the Deutsche Forschungsgemeinschaft (CRC TRR332 A2 & Z1, CRC1009 A13, CRC1123 A6, 502158695), the Leducq Foundation, and IZKF and the IMF of the Medical Faculty Münster. L.A.W. acknowledges funding from the Bachynski Family Foundation and D.F.Q. receives support from Canada Foundation for Innovation (CFI 42884). The CNIC is supported by the MCIN, the Instituto de Salud Carlos III, and the Pro-CNIC Foundation and is a Severo Ochoa Center of Excellence (grant number CEX2020-001041-S funded by MCIN/AEI/10.13039/501100011033). M.S.F.N. is supported by the National Medical Research Council Young Individual Research Grant (MOH-OFYIRG24jan-0012). I.K. receives funding from the National Medical Research Council Young Individual Research Grant (MOH-OFYIRG24jan-0032) and the Skin Research Institute of Singapore Joint ReseaRch Grant (SRIS_JRG_2003). C.S. is supported by National Natural Science Foundation of China (grant 32300756), J.H. is supported by Noncommunicable Chronic Diseases-National Science and Technology Major Project (2023ZD0501300), M.Z. is supported by National Natural Science Foundation of China (grant 82370751) and J.P. is supported by National Natural Science Foundation of China (grant 82421001).

Author contributions Conceptualization: I.B., A. Hidalgo and L.G.N. Data curation: D.C.-W., A.R.-P., M. Richter, E.P., J.C.N., I.K., G.M., D.G.A., D.J.-C., C.T., D.M.G., C.S., R.K.-H., J. Sicilia and I.B. Formal analysis: D.C.-W., A.R.-P., M.R., E.P., J.C.N., I.K., D.G.A., D.J.-C., D.M.G., G.F.-C., J. Sicilia and I.B. Funding acquisition: A. Moraga, M.A.M., K.d.B., A.D., H.H., G.F.C., F.S.-C., O.S., D.F.Q., L.A.W., L.G.N., A. Hidalgo and I.B. Investigation: D.C.-W., A.R.-P., M. Richter, I.K., A.C.G.-C., N.B.B., S.D., S. Callejas, A.A.-C., M.A.Z., D.M., S.M.-S., T.D., S.O., T.V., G.C., A.M., J.Z., M.I.C., I.R., M.Z., M.S.F.N., D.C.v.O., A.E.D., F.C., S. Chang, A. Martin and I.B. Methodology: D.C.-W., A.R.-P., E.P., G.M., G.F.C., A. Hidalgo and I.B. Project administration and supervision: A. Hidalgo. Resources: A. Moraga, M.A.M., K.d.B., A.L.G., W.C.G., J.D.S., H.H., G.F.C., F.S.-C., A.D., I.A.U., J.J.F., J.A.B., O.S., D.F.Q., L.A.W., J.H., Y.W., M.Z., J. Skokowa, A. Martin, J.P., L.G.N., A. Hidalgo and I.B. Software: A.R.-P., E.P., G.M., D.G.A. and D.J.-C. Validation: D.C.-W., A.R.-P., A.C.G.-C., P.O.F. and I.B. Visualization: D.C.-W., A.R.-P., A. Hidalgo and I.B. Writing: A. Hidalgo and I.B.

Competing interests J.C.N. is a scientific advisor of Omniscope. The other authors declare no competing interests.

Additional information

Supplementary information The online version contains supplementary material available at https://doi.org/10.1038/s41586-025-09807-0.

Correspondence and requests for materials should be addressed to Lai Guan Ng, Andrés Hidalgo or Iván Ballesteros.

Peer review information *Nature* thanks Ash Alizadeh, Paul Kubes and the other, anonymous, reviewer(s) for their contribution to the peer review of this work.

Reprints and permissions information is available at http://www.nature.com/reprints.

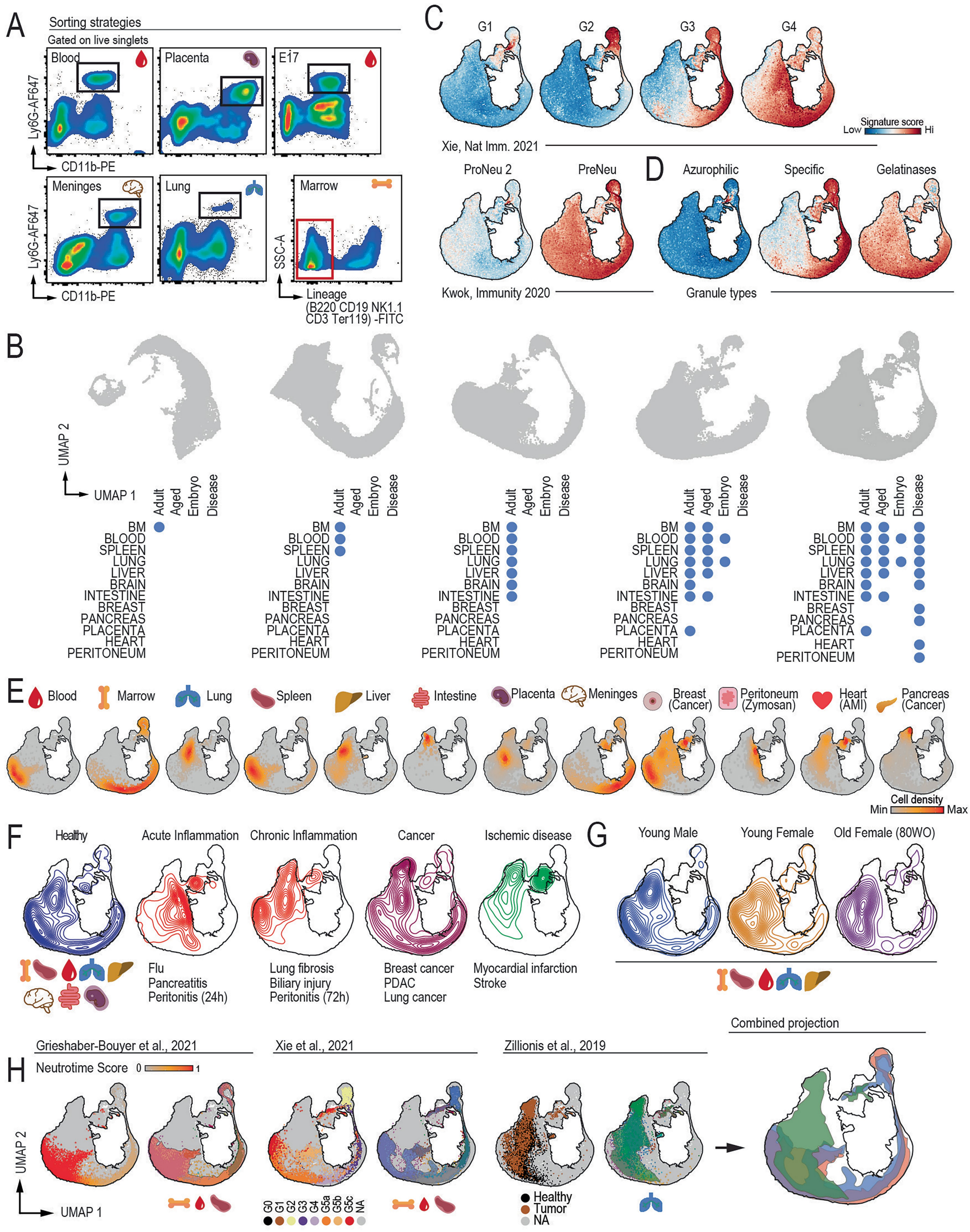

Extended Data Fig. 1 | See next page for caption.

Extended Data Fig. 1 | NeuMAP, a map of the neutrophil transcriptome. (**A**) Plots showing the sorting strategy to isolate neutrophils from the indicated tissues. Note the different gating for the bone marrow. (**B**) Evolution of the NeuMAP by the cumulative addition of neutrophils from the indicated tissues. (**C**) Score expression on the NeuMap of published gene sets associated with neutrophil differentiation and maturation. (**D**) Score values of genes expressed in primary, secondary, and specific granules onto the NeuMAP. (**E**) K-mass score of neutrophils by the indicated tissue of origin in the NeuMAP. (**F**) Contour plots of the combined neutrophils from the indicated tissues in various conditions of disease. (**G**) Contour plots of the combined neutrophils from the indicated tissues of males, females, and old (80 week-old) individuals. (**H**) Mapping of neutrophils from the indicated studies, showing their distribution in the NeuMap.

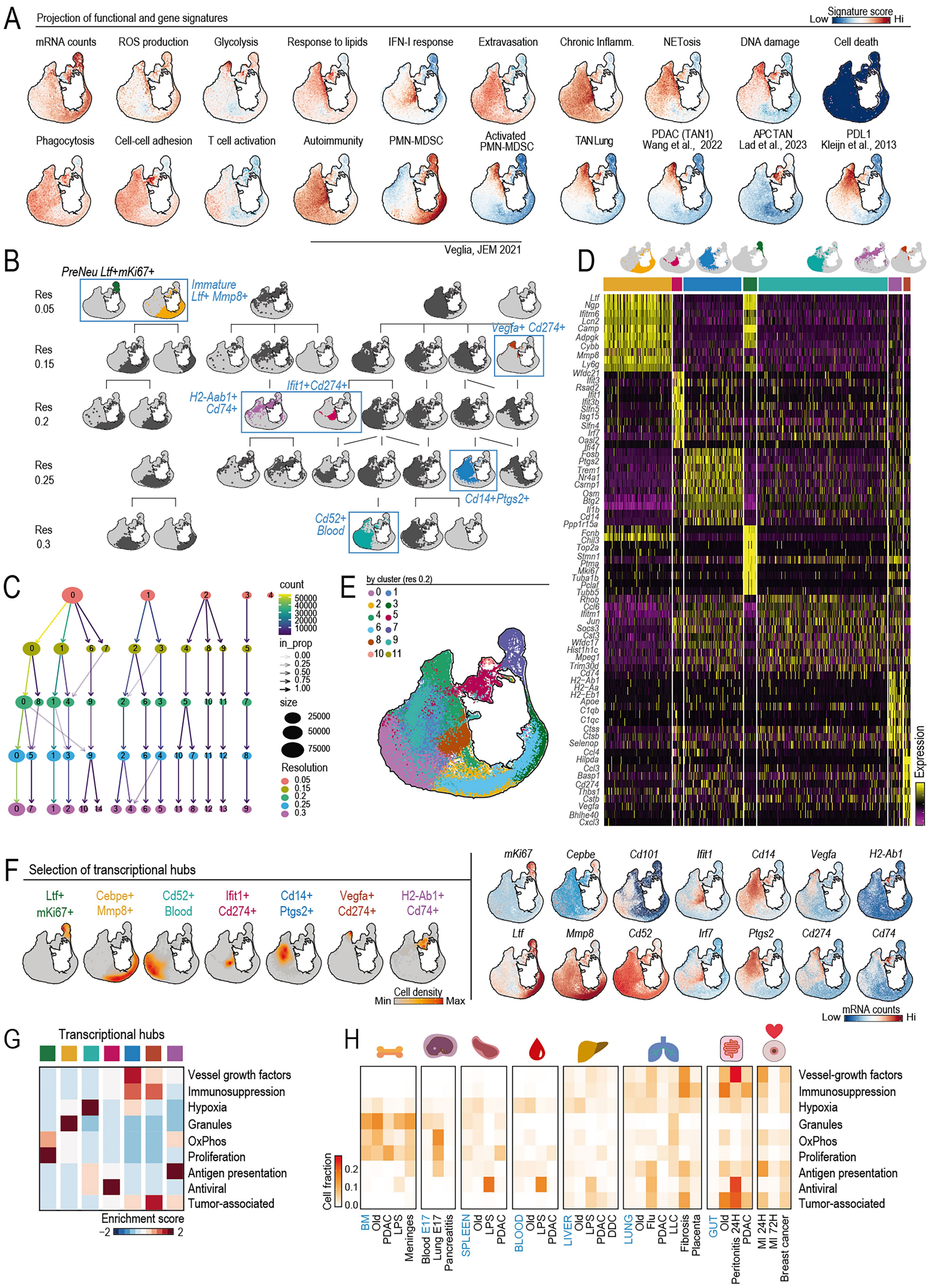

Extended Data Fig. 2 | See next page for caption.

Extended Data Fig. 2 | Identification of clusters and transcriptional hubs in the NeuMap. (**A**) Score expression of gene sets from specific biological processes. See Supplementary Table 2 for a complete gene list. (**B**) Clustering of the NeuMap with different levels of resolution. The clusters that best captured the functional areas were selected across the different resolutions to annotate the transcriptional hubs of the NeuMAP (as in Fig. 1). (**C**) Clustering tree of 151,960 neutrophils from R0.05 to R0.3, with clusters labeled according to their size. The arrow intensity reflects the proportion of cells and the color of the number of cells assigned to the other clusters. (**D**) Heatmap of the differentially expressed genes for each transcriptional hub. For a complete gene list see Supplementary Table 3. (**E**) Clustering of the NeuMap at resolution 0.2. (**F**) Transcriptional hubs from (**B**) and mRNA expression of the indicated genes. (**G**) Heatmap showing the enrichment scores of the functional signatures in the transcriptional hubs **(H)** Heatmap showing the proportion of cells in all the conditions included in the NeuMap that contribute to the top 5% expressing cells for each indicated functional gene signature. The number of cells per tissue was downsampled to 1000 prior to the calculation of the contribution proportion.

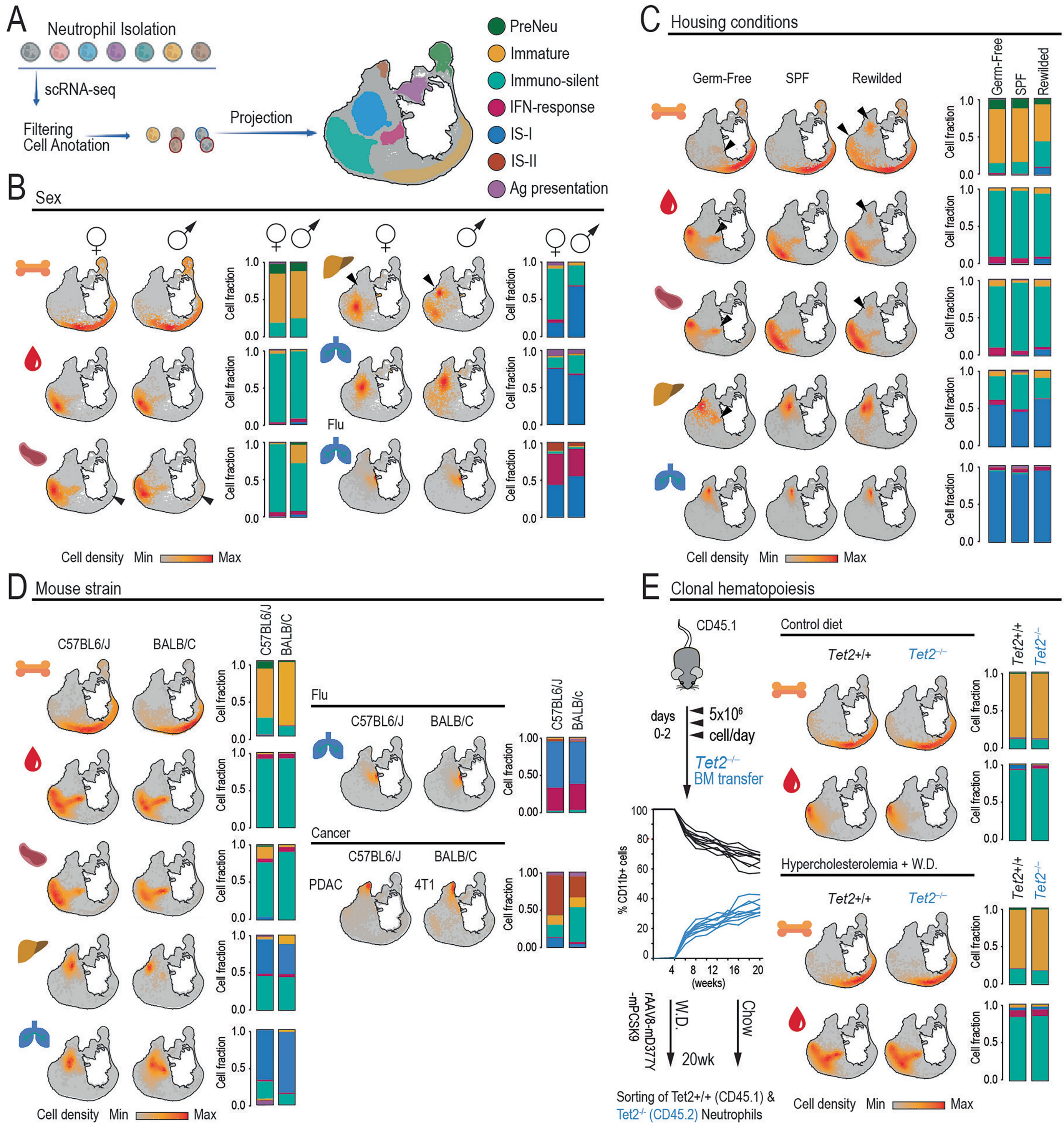

Extended Data Fig. 3 | Architecture of the NeuMap across sex, environmental conditions, mouse strains, and genetic alterations. (**A**) Experimental strategy and projection onto the NeuMap to assess neutrophil distribution across transcriptional hubs. (**B**) K-mass density plots and stacked bar graphs showing hub distribution of neutrophils from healthy tissues and influenza-infected lungs, separated by sex (male and female). (**C**) K-mass scores and hub distributions of neutrophils isolated from indicated tissues in naïve male mice housed under germ-free (GF), specific pathogen-free (SPF), or rewilded (RW) environmental conditions. (**D**) K-mass scores and hub distributions of neutrophils from healthy tissues, flu-infected lungs, and tumors in C57BL/6 J and BALB/c mice, showing conserved hub structure across mouse strains. (**E**) K-mass scores and hub distributions of wild-type and Tet2^{-}/$^{-}$ neutrophils isolated from non-irradiated bone marrow chimeras, under control (upper panels) or hypercholesterolemic (lower panels) conditions, illustrating hub preservation across genetic backgrounds. WD, Western diet.

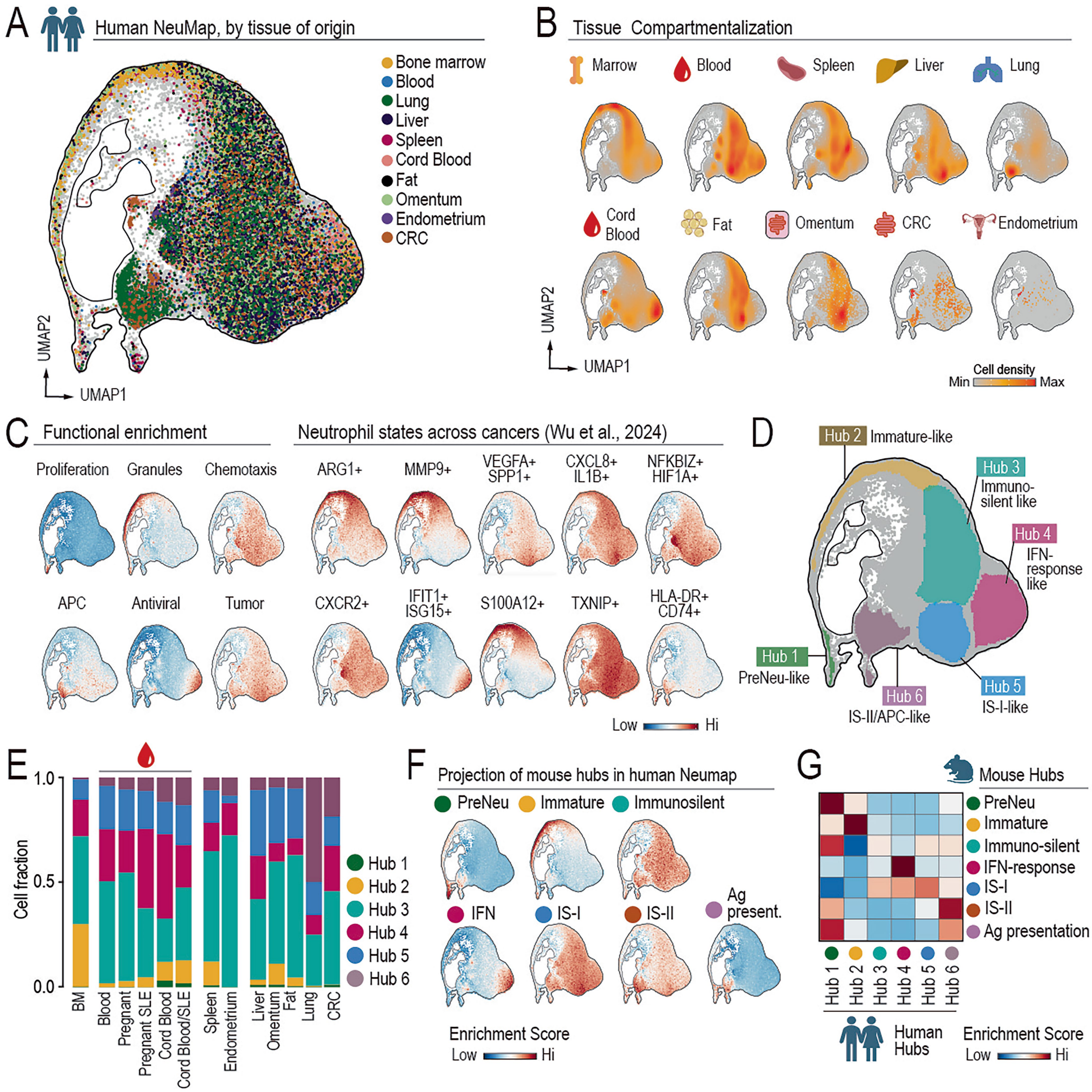

Extended Data Fig. 4 | Architecture of the human neutrophil compartment (human NeuMap). (**A**) UMAP visualization of human neutrophils colored by tissue of origin. Data were downsampled to 3,000 cells per cluster for visualization. A complete list of samples is provided in Supplementary Table 4. (**B**) Two-dimensional kernel density estimation showing cell density distributions across tissues. (**C**) Module scores for selected biological processes (left) and for human neutrophil signatures recently described in ref. 18 across 12 cancer types (right). Gene lists are provided in Supplementary Table 2. (**D**) Functional compartmentalization of the human NeuMap. Each hub is defined as the area containing the top 85% K-mass score. For a complete gene list of differentially expressed genes for each transcriptional hub see Supplementary Table 4. (**E**) Stacked bar plots showing the proportion of neutrophils across different organs and conditions within each hub, defined in (D). (**F**) Score values of murine hubs across the human NeuMap, showing preferential distributions matching the hubs defined in the human NeuMap. (**G**) Gene Module scores of murine hubs projected onto human neutrophil hubs, scaled by row. CRC, colorectal cancer; BM, bone marrow; SLE, systemic lupus erythematosus. Drawings in **b**,**g** were created in BioRender. Cerezo Wallis, D. (2025) https://BioRender.com/pfm336w.

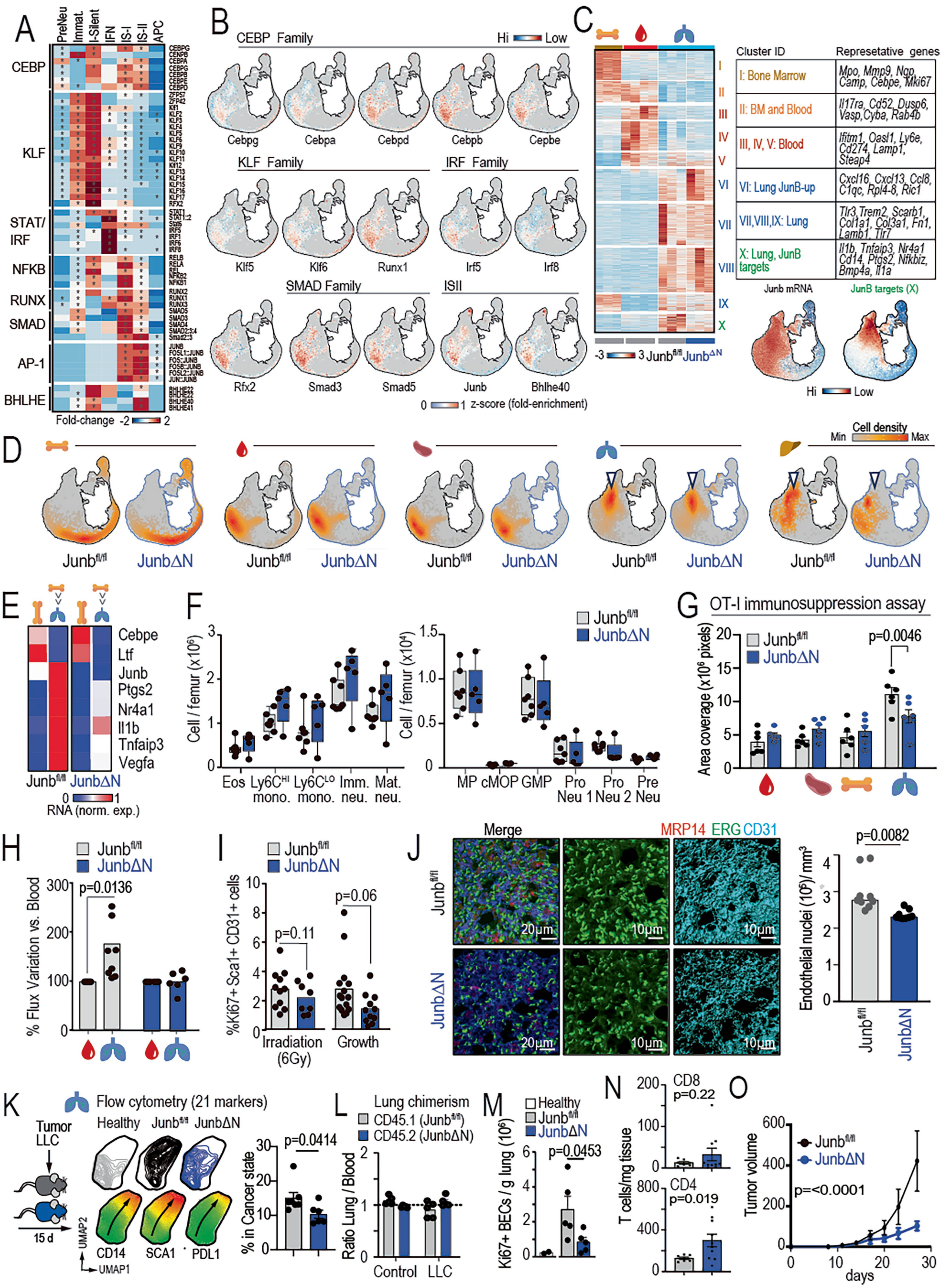

Extended Data Fig. 5 | See next page for caption.

Extended Data Fig. 5 | Characterization of JunbΔN mice. (**A**) Heatmap showing the fold enrichment in binding sites for the indicated transcriptional factors (TF) associated with each hub. *, statistically significant motif enrichment. (**B**) chromatin accessibility scores for the indicated TF projected onto the NeuMAP, as determined by scATAC-sequencing combined with scRNA-seq (Dogma-seq). For a complete list of enriched motifs see Supplementary Table 5. (**C**) Heatmap of differentially expressed genes obtained by bulk RNA-seq of neutrophils from the BM, blood, and lung of wildtype mice, and lung of JunBΔN mice, as indicated in the table at right. Bottom right, JunB mRNA levels and signature of JunB target genes are projected in the NeuMAPs. For a complete list of DEGs see Supplementary Table 6. (**D**) K-mass values of neutrophils obtained from BM, blood, lungs, spleen, and livers of control Junb$^{fl/fl}$ and JunBΔN mice. (**E**) Expression of the indicated genes by RT-PCR analysis of Junb$^{fl/fl}$ and JunBΔN BM neutrophils, before and after intratracheal transfer into the lungs of WT mice. (**F**) Quantification of immature and mature myeloid cell progenitors and mature populations in the BM of control Junb$^{fl/fl}$ and JunBΔN mice. Eo, eosinophils, Mono, monocytes, Imm. Neu, immature neutrophils, Mat.neu, mature neutrophils; CMP, common myeloid progenitor; cMoP, common monocyte progenitor; GMP, granulocyte-monocyte progenitor. Data is from 7 WT and 5 JunBΔN mice. No significant differences found as determined by two-tailed Student's t-test. Data are presented as mean ± SEM. Box plots represent median (center line), interquartile range (box limits, 25th–75th percentiles), whiskers (min–max), and all individual data points are shown. (**G**) Quantification of OT-1 T cell killing of B16OVA target cells in the presence of neutrophils from the indicated tissues of control Junb$^{fl/fl}$ and JunBΔN mice. Data is data are mean ± SEM 6 mice per group. Significant differences shown in figure, as determined by two-tailed Student's t-test (**H**) Quantification of the vascularization of Matrigel plugs co-injected with blood or lung neutrophils from control and JunBΔN mice, as assessed by Doppler analysis. Data are mean ± SEM from 9 WT and 6 JunBΔN mice. p = 0.0136 in control mice and p = 0.9541 in JunBΔN mice as determined by two-tailed Student's t-test (**I**) Percentage of proliferative endothelial cells (Ki67+ Sca1 + CD31 +) in lungs from control and JunBΔN mice after irradiation (left) or during organismal growth (4-week-old mice; right). Data are mean ± SEM from 11-8 mice irradiated, and 15-11 mice growth. p = 0.11 for irradiated or p = 0.06 for growing mice as determined by two-tailed Student's t-test. (**J**) Representative images and quantification of the density of CD31 + ERG+ endothelial cells (MRP14) in control and JunBΔN mice. Data are mean ± SEM from 3 regions from 3 independent mice per group. Differences determined by two-tailed Student's t-test. (**K**) Experimental setup and multiparametric cytometric analysis (21 markers) of lung neutrophils from LLC tumors implanted in Cre^{NEG} control and JunBΔN mice. The UMAP projections show the distribution of neutrophils from each mouse and the expression of CD14, Sca1 and PDL1. Right, percentage of control and JunB-deficient neutrophils that acquire the "Cancer" phenotype. Data are mean ± SEM from 6 JunBΔN, and −7 WT mice. p = 0.0414 as determined by two-tailed Student's t-test. (**L**) Ratio of Cre^{NEG} control and JunBΔN neutrophils that infiltrate the lungs relative to the numbers in blood, in naïve and LLC tumor-bearing mice, using transplantation chimeric mice. Data are mean ± SEM from 5 mice per group. (**M**) Number of proliferative endothelial cells (BECs) in the lungs of healthy and tumor-bearing mice 3 weeks after tumor implantation. BECs were analyzed by flow cytometry. Data mean ± SEM from 5 mice per the tumor-bearing group; p = 0.0453 as determined by by two-tailed Student's t-test. (**N**) Absolute number of CD4 or CD8 T cells infiltrating LLC tumors in control and JunBΔN mice; data are mean ± SEM from 7 WT and10 JunBΔN mice. (**O**) Volume of subcutaneous LLC implanted tumors in control versus JunBΔN mice over time; data are mean ± SEM from 6 WT and 5 JunBΔN. Differences determined by Two-way ANOVA with Tukey correction.

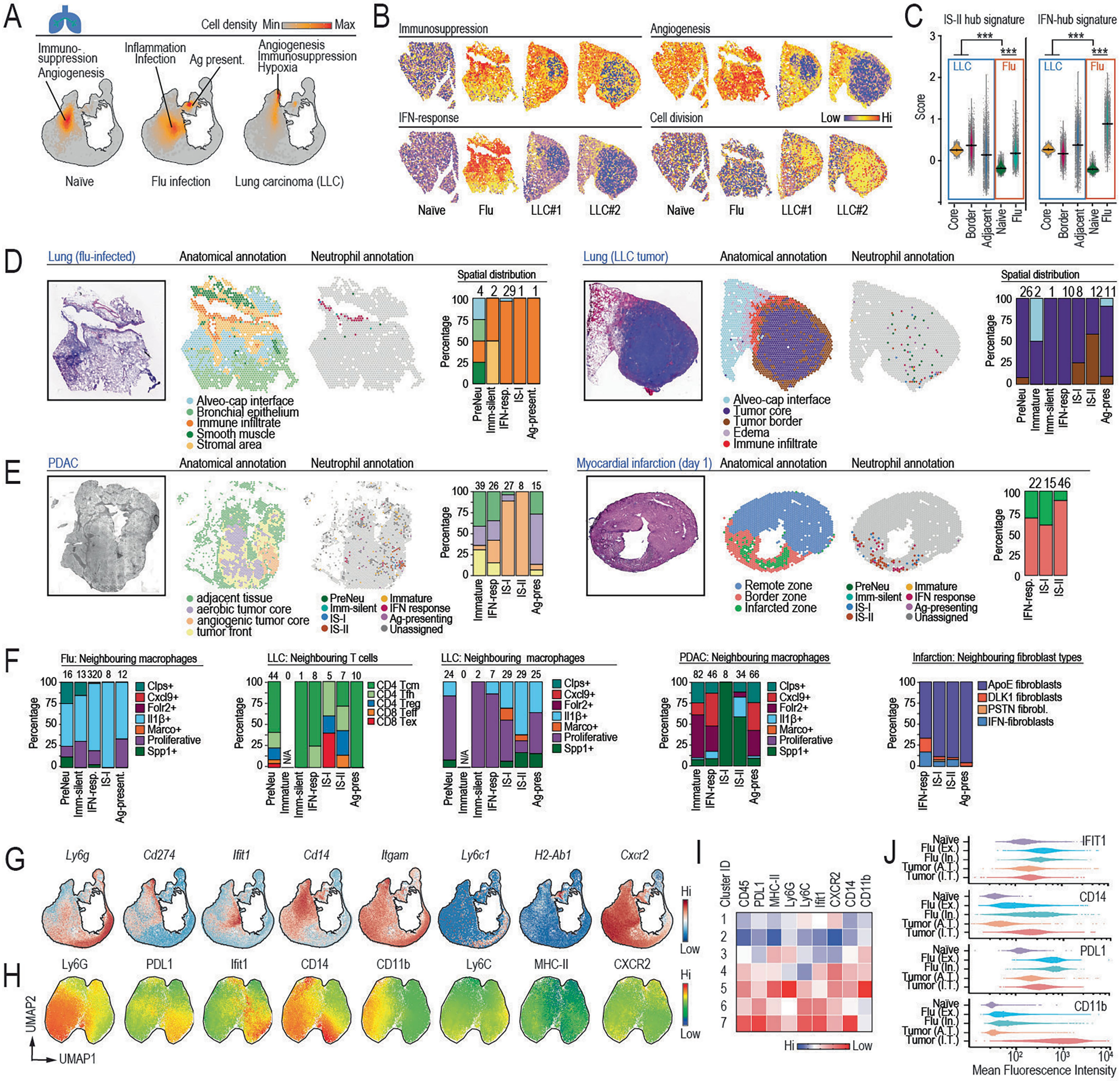

Extended Data Fig. 6 | Spatial characterization of neutrophils. (**A**) K-mass score of neutrophils from lungs of naïve, tumor-bearing, and flu-infected mice. (**B**) Score of the indicated signatures onto the spatial transcriptomic dataset in the naïve, tumor-bearing, and flu-infected lung sections. (**C**) Enrichment scores of neutrophils for the IS-II and IFN-response signatures. Statistics Wilcoxon pairwise Test; *** $p < 0.001$ (**D**) H/E staining of lungs from tumor-bearing (LLC), and flu-infected lung sections. Deconvolution using LungMap Project3 allows annotation of cells the tissues used for spatial transcriptomics. Right, bars show the percentage distribution of neutrophils assigned to the indicated hubs in the different annotated regions of the tissue. (**E**) Analyses as in (**D**) performed in a PDAC tumor (from ref. 7) and an infarcted myocardial tissue (one day after ischemia; from ref. 23). (**F**) Percent of closest neighbouring cells (macrophages, T cells or fibroblasts) featuring the indicated profiles to neutrophils from the different hubs. The numbers on top indicate the number of neighbouring cells around neutrophils from each hub, when available. (**G**) Expression of the indicated genes encoding for surface markers in the NeuMAP, and (**H**) expression of the respective proteins represented in the UMAP generated with neutrophils stained using the MACSima platform (see Methods). (**I**) Heatmap showing the expression of the indicated proteins in the neutrophil clusters identified using MACSima. (**J**) Mean fluorescence expression intensity of the indicated proteins in neutrophils in different regions of the tissues analyzed by multiparametric immunofluorescence. Ex, extravascular; In, intravascular; AT, adjacent tissue; IT, intratumoral.

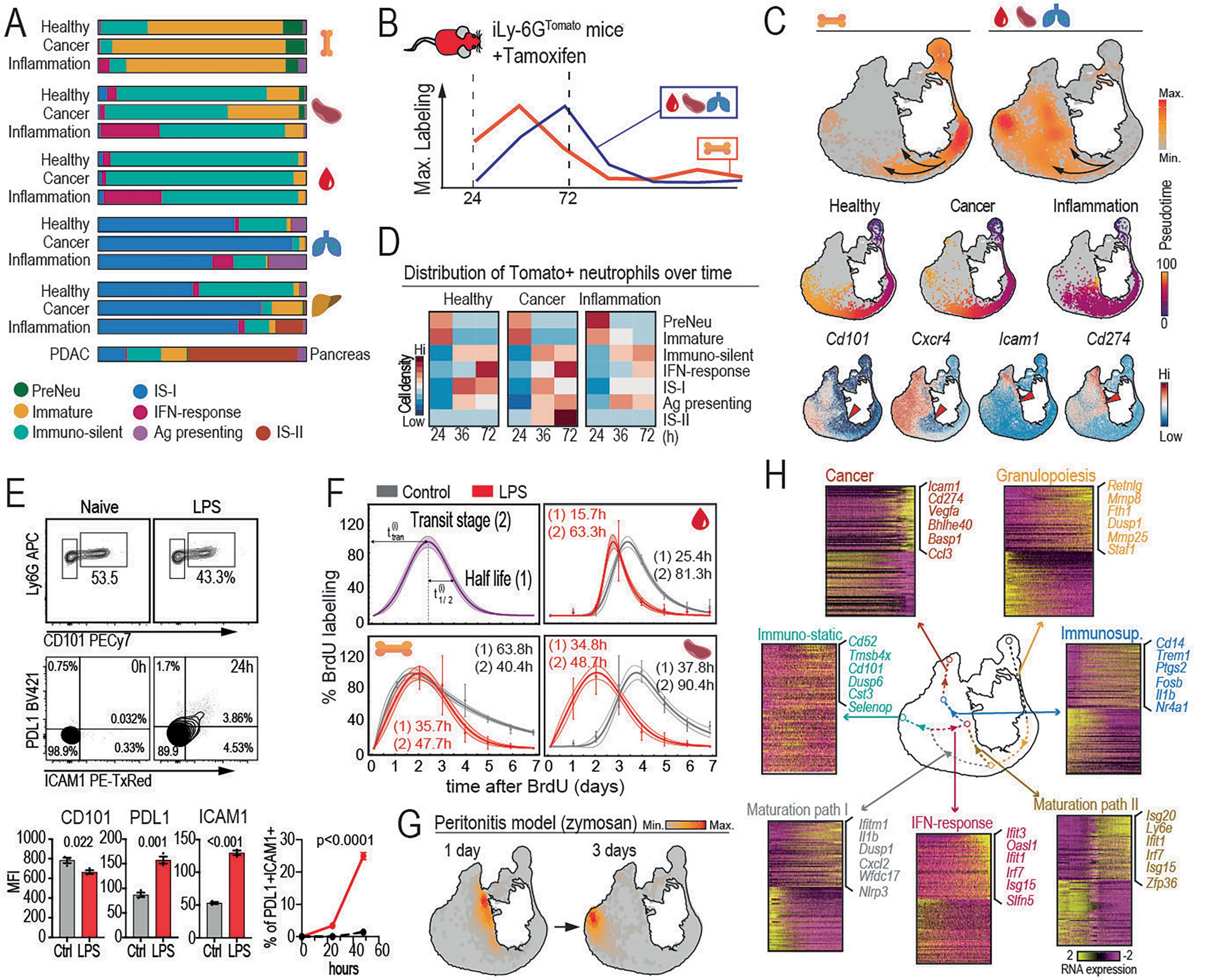

Extended Data Fig. 7 | Dynamics of neutrophil maturation. (**A**) Fraction of neutrophils in the different transcriptional hubs for the indicated tissues and conditions of naive, tumor-bearing or LPS treated mice (**B**) Experimental setup for the timestamp experiment in iLy6GtdTomato mice, showing the frequency of Tomato+ neutrophils in the indicated tissues at different times after tamoxifen administration. Neutrophils were collected from BM (24 h), and tissues (36 and 72 h). (**C**) Upper panels, cell density (K-mass) in the NeuMap of pulse-labelled neutrophils from the BM (left) or tissues (right) of naïve, tumor-bearing, and flu-infected mice. Middle panels, pseudotime scores of BM neutrophils from the three conditions. Lower panels, expression of relevant maturation and activation genes projected in the NeuMap. (**D**) Heatmap showing the distribution of Tomato+ neutrophils along the different transcriptional hubs over time, determined from the timestamp experiment. (**E**) Flow cytometric plots and quantification of mature blood neutrophils (CD101 + Ly6G +), and expression of PDL1 and ICAM1 in BM neutrophils in response to LPS treatment, and kinetics of the percentage of PDL1 + ICAM1+ cells over time after LPS treatment. Mean ± SEM from 3 replicates. Two-tailed unpaired T-test (bar graph) p = 0.022 (CD101), p = 0.001 (PDL1) and p = 0.000037. Two-way Anova with Šídák's multiple comparisons test (time-course) p < 0.00001 (**F**) In vivo kinetics of neutrophils from the indicated organs showing their transition from the BM to blood and to spleen of naïve or LPS-treated mice, determined by BrdU staining. Mean ± SD from 4 independent mice. (**G**) Transcriptional distribution in the NeuMAP of peritoneal-infiltrating neutrophils at 1 and 3 days of zymosan injection. (**H**) Representative genes that change along the trajectories defined in Fig. 3e. For the complete set see Supplementary Table 7.

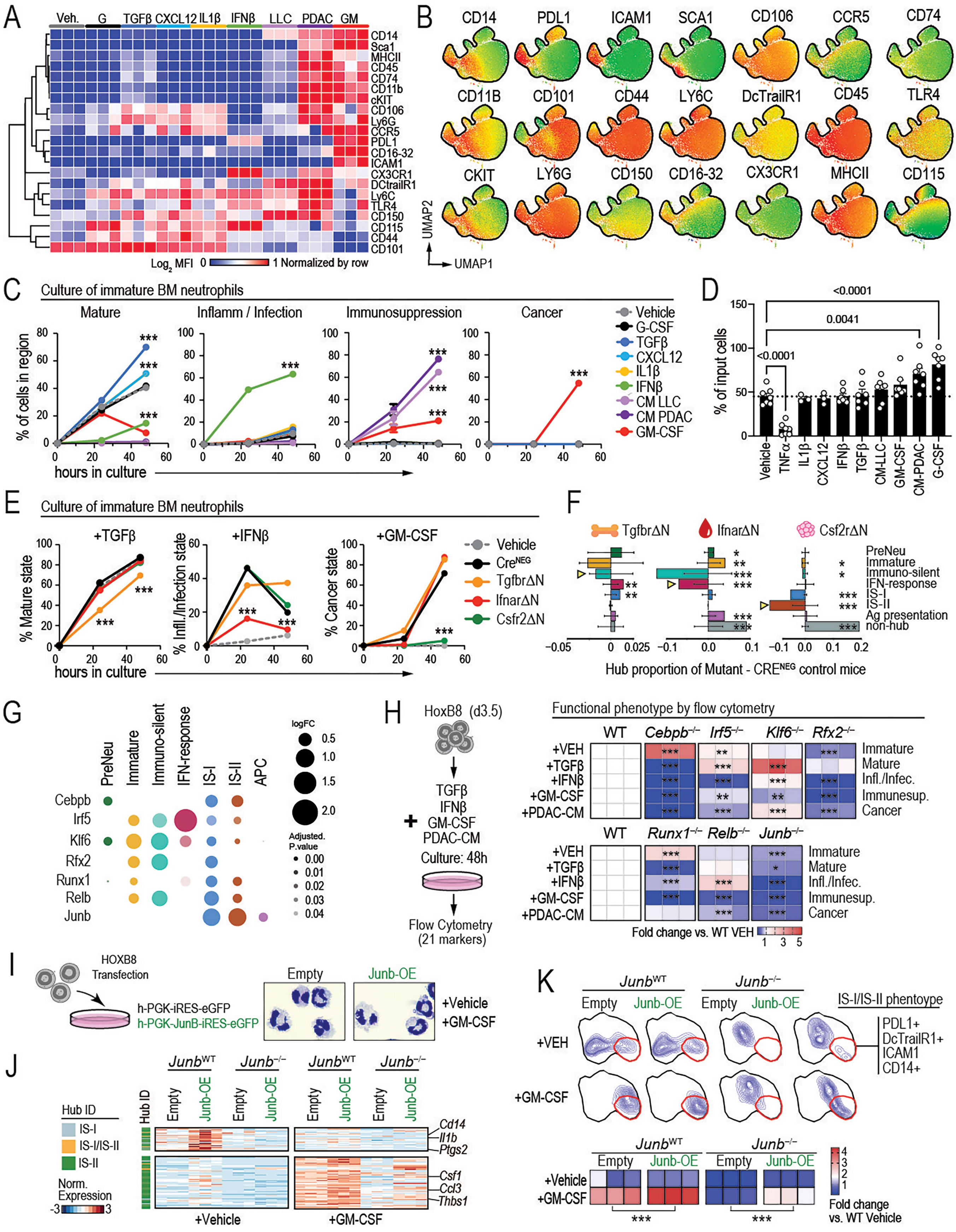

Extended Data Fig. 8 | See next page for caption.

Extended Data Fig. 8 | Analysis of ex vivo neutrophil cultures. (**A**) Heatmap showing expression of 21 markers in mature neutrophils treated with the indicated cytokines and conditioned media for 24 h. G, G-CSF, CM LLC, conditioned medium of LLC cells; CM PDAC, conditioned medium of FC1242 pancreatic cancer cells; GM, GM-CSF. (**B**) Projection of marker expression in the UMAP obtained by multiparametric flow cytometry. (**C**) Percentage of neutrophils classified as "Mature", "Inflammation/infection","immunosuppression", and "Cancer" after ex vivo culture for 24 and 48 h with the indicated cytokines and conditioned media. Data is from 4 independent experiments. ***, $p < 0.001$ compared with the vehicle group at the respective time point, as determined by Two-way ANOVA with Dunnett's multiple comparison test. Mature: Control vs. TGFβ, Cxcl12, IL1β, IFNβ, CM LLC, CM PDAC and GM-CSF $p < 0.000001$. Inflammation/Infec= Control vs. IFNβ $p < 0.000001$. Immunosuppression: Control vs. CM LLC, CM PDAC and GM-CSF $p < 0.000001$. Cancer: Control vs. GM-CSF $p < 0.000001$. (**D**) Percentage of viable cells after ex vivo culture of neutrophils for 48 h with the indicated treatments. Data are mean ± SEM from 3–7 individual experiments. One-way ANOVA with Dunnett's multiple comparison test. Vehicle vs. TNFα and G-CSF, $p < 0.000001$. Vehicle vs. CM PDAC $p = 0.0041$ (**E**) BM neutrophils from control Cre^{NEG}, TgfbrΔN, IfnarΔN and Csf2rΔN mice were cultured ex vivo for 24 and 48 h with TGFβ, IFNβ and GM-CSF. The plots show the percentage of neutrophils with a "Mature" phenotype after treatment with TGFβ, an "Inflammation/infection" phenotype after treatment with IFNβ, and a "Cancer" phenotype after treatment with GM-CSF. Data is from 3 independent experiments and statistics are as in (C). as determined by two-Way ANOVA with Tukey's multiple comparison test. + TGFβ: TgfbRΔN vs. Cre^{Neg}, IfnarΔN, and Csf2rΔN $p < 0.000001$. + IFNβ: IfnarΔN vs. Cre^{Neg}, Csf2rΔN, and TgfbRΔN $p < 0.000001$. + GM-CSF: Csf2rΔN vs. IfnarΔN, Cre^{Neg}, and TgfbRΔN $p < 0.000001$ (**F**) Changes in the distribution of neutrophils from TgfbRΔN, Ifnar1ΔN and Csf2rΔN mice across the transcriptional hubs of the NeuMap, determined by scRNA-sequencing relative to Cre^{NEG} control mice. The arrowheads indicate the more relevant hubs examined for each mutant, as determined from Fig. 4h. P values comparing the distribution of control vs. mutant cells were calculated using a bootstrap approach (see Methods). The figure shows the delta proportions of neutrophil hubs between the mutant and control mouse. Bars show confidence intervals of the random distributions. TgfbrΔN: IFN-resp $p = 0.0017$, IS-I $p = 0.0037$. IfnarΔN: PreNeus $p = 0.0137$, Immature $p = 0.0043$, Immune-Silent $p = <0.00001$, IFN-resp. $P = 0.0002$, Ag-Present. $P < 0.00001$. Csf2rΔN: Immature $p = 0.0239$, Immune-silent $p = 0.0252$, IS-I $p < 0.00001$, IS-II $p < 0.00001$ (**G**) Transcription factor (TF) enrichment across NeuMap transcriptional hubs, identified by DOGMA-seq. Dot size indicates odds ratio, and color intensity reflects the adjusted p-value. (**H**) Functional profiling of HoxB8-derived neutrophils lacking the indicated TFs (Cebpb, Irf5, Klf6, Rfx2, Runx1, Relb, JunB) or wild-type controls, after 48 h treatment with the indicated cytokines or PDAC-conditioned medium. Heatmaps show the proportion of cells in each phenotypic cluster (Immature, Mature, Inflammation/Infection, immunosuppression, Cancer), based on flow cytometry marker expression. Data are from three independent experiments. *$p < 0.05$, **$p < 0.01$, ***$p < 0.001$, One-way ANOVA with Dunnett's multiple comparison test. (**I**) Schematic representation of JunB overexpression in HoxB8 progenitors using lentiviral transduction. Representative cytospin images of control and JunB-overexpressing neutrophils at day 5 post-estrogen withdrawal confirm comparable polymorphonuclear morphology. (**J**) Heatmap showing differentially expressed IS-I/IS-II-associated genes identified by bulk RNA sequencing of HoxB8-derived neutrophils (wild-type; $\textit{Junb}^{\text{WT}}$, JunB knockout; $\textit{Junb}^{-/-}$, or JunB-overexpressing; OE) cultured for 48 h with vehicle or 10 ng/ml GM-CSF. (**K**) UMAP contour plots derived from multiparametric flow cytometry (21 markers) of HoxB8-derived neutrophils from the same experimental groups as in (J), after 48-hour culture with vehicle or GM-CSF. Heatmaps below indicate the proportion of cells within the IS-I/IS-II-associated gate for each condition. Data represent $n = 3$ independent experiments. ***$p < 0.001$, one-way ANOVA with Dunnett's multiple comparison test.

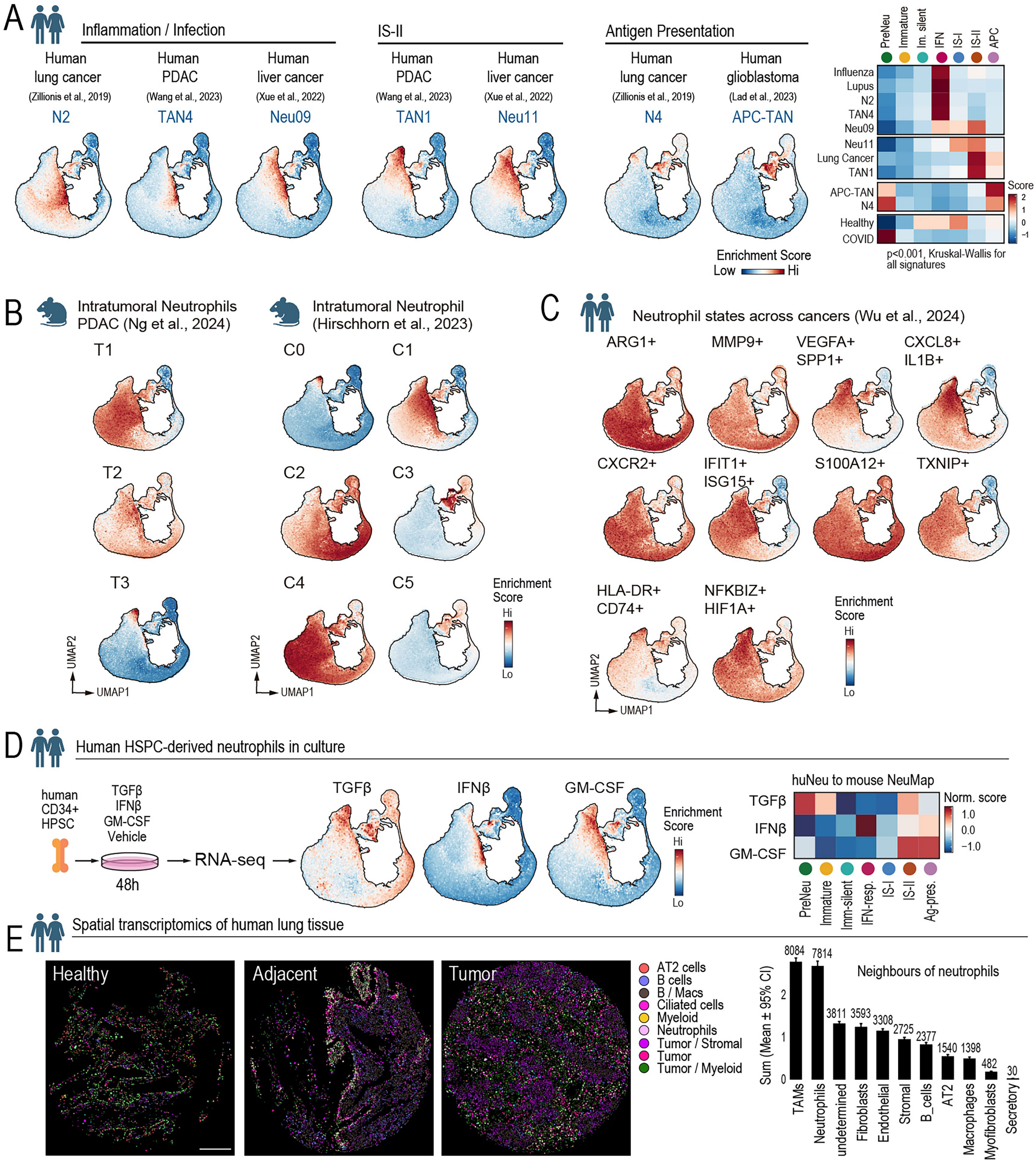

Extended Data Fig. 9 | See next page for caption.

Extended Data Fig. 9 | Predictive potential of the NeuMAP. (**A**) Enrichment score of signatures obtained from human neutrophils from four types of cancer (lung, liver and pancreas, and glioblastoma, GBM). Shown are the associations of different clusters of neutrophils from these human cancers with hubs of inflammation/Infection (left), Angiogenesis/Immunosuppression (middle), and Antigen presentation (right). Shown are the cluster names from the indicated studies. See also Fig. 5a for similar projections in infectious, autoimmune disease and lung cancer. Right, heatmap of average enrichment scores for each hub signature, scaled by signature. (**B**) Signature scores from intratumoral neutrophil populations (T1–T3) from ref. 7 (left), and from those described by ref. 92 (C1-C6) (Right). (**C**) Signature scores from intratumoral neutrophil identified by ref. 18 across 12 types of human cancers. (**D**) Human neutrophils derived from bone marrow CD34 + HSPC were cultured with the indicated cytokines and their RNA sequenced. Enrichment scores were computed for each cytokine-induced signature and mapped onto NeuMAP. Right, heatmap showing mean signature scores across hubs. Scale bar 200 µm (**E**) Spatial transcriptomic maps of lung tissue from patients with lung adenocarcinoma, comparing healthy, adjacent, and tumor regions. Cell types were annotated by deconvolution and overlaid as spatial coordinates. Right, neighbourhood composition using a curated cell annotation. The exact n value for each cell type is indicated next to the corresponding bar in the graph. Data are presented as mean ± SEM. Drawings in **a**–**e** were created in BioRender. Cerezo Wallis, D. (2025) https://BioRender.com/pfm336w.

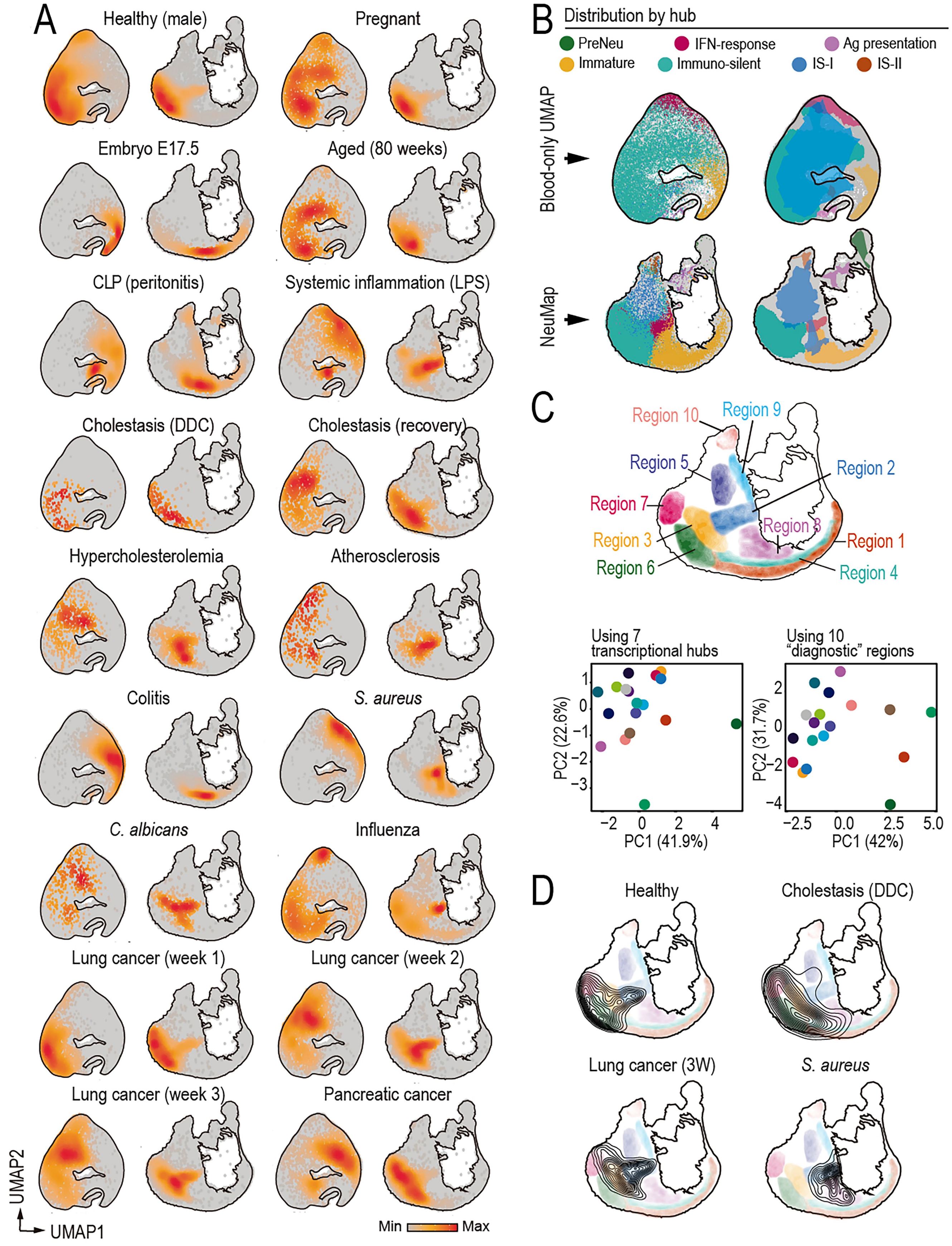

Extended Data Fig. 10 | See next page for caption.

Extended Data Fig. 10 | Diagnostic potential of blood neutrophils projected in the NeuMap. (**A**) Blood neutrophils from 18 conditions were projected onto the blood-only UMAP or the NeuMap based on their transcriptional profile and are shown as densities or K-mass. (**B**) Distribution of cells with their assigned transcriptional hub (by color) in the blood-only UMAP and in the NeuMAP (left), showing the overlapping areas of the different hubs. (**C**) PCA analysis of blood sample distribution based on the Bhattacharyya index obtained using the 7 transcriptional hubs or the 10 expanded diagnosis regions. (**D**) Representative examples of the distribution of the blood neutrophils from four conditions onto the expanded diagnostic regions that we used to calculate the Bhattacharyya indices.

nature portfolio

Corresponding author(s): Andrés Hidalgo: Iván Ballesteros

Last updated by author(s): Oct 5, 2025

Reporting Summary

Nature Portfolio wishes to improve the reproducibility of the work that we publish. This form provides structure for consistency and transparency in reporting. For further information on Nature Portfolio policies, see our Editorial Policies and the Editorial Policy Checklist.

Statistics

For all statistical analyses, confirm that the following items are present in the figure legend, table legend, main text, or Methods section.

n/a	Confirmed	
☐	☒	The exact sample size (*n*) for each experimental group/condition, given as a discrete number and unit of measurement
☐	☒	A statement on whether measurements were taken from distinct samples or whether the same sample was measured repeatedly
☐	☒	The statistical test(s) used AND whether they are one- or two-sided *Only common tests should be described solely by name; describe more complex techniques in the Methods section.*
☒	☐	A description of all covariates tested
☒	☐	A description of any assumptions or corrections, such as tests of normality and adjustment for multiple comparisons
☐	☒	A full description of the statistical parameters including central tendency (e.g. means) or other basic estimates (e.g. regression coefficient) AND variation (e.g. standard deviation) or associated estimates of uncertainty (e.g. confidence intervals)
☐	☒	For null hypothesis testing, the test statistic (e.g. *F*, *t*, *r*) with confidence intervals, effect sizes, degrees of freedom and *P* value noted *Give P values as exact values whenever suitable.*
☒	☐	For Bayesian analysis, information on the choice of priors and Markov chain Monte Carlo settings
☒	☐	For hierarchical and complex designs, identification of the appropriate level for tests and full reporting of outcomes
☒	☐	Estimates of effect sizes (e.g. Cohen's *d*, Pearson's *r*), indicating how they were calculated

Our web collection on statistics for biologists contains articles on many of the points above.

Software and code

Policy information about availability of computer code

Data collection	BD Aria Cell Sorter, BD Symphony A4 Flow cytometer — for single-cell sorting and acquisition of flow cytometry data Leica SP5 Confocal Microscope — for whole-slide Z-stack image acquisition Vevo Imaging Systems — for subcutaneous LLC tumor vascularization imaging MACSima Imaging System (Miltenyi Biotec) — for high-content multiplexed protein imaging HiSeq2500, NovaSeq 6000, and NovaSeq X Plus (Illumina) — for RNA-seq, ATAC-seq, and spatial transcriptomic sequencing Visium CytAssist HD slides (10x Genomics) — for spatial transcriptomics sample preparation Rhapsody single cell platform (BD) and Chromium Next GEM Single Cell Multiome ATAC + Gene Expression platform (10x Genomics) for multiomic library generation.
Data analysis	-ImageJ (v 2.3.0/153t, NIH) and Imaris (v.9.5, Bitplane) for imaging analysis -MACS iQ View Analysis Software (Version 1.3.2) (Miltenyi Biotec) — for MACSima image analysis -FlowJo v10 (BD Biosciences) — for analysis of flow cytometry data acquired on the Symphony A4 Flow Cytometer -GraphPad Prism v9 and 10.10— for data visualization and statistical tests -R v4.0.3 and R v5.2.1 — core statistical and computational environment -Seurat v4.0.5 and v4.3 — for single-cell and spatial transcriptomic analysis -CASAVA v1.8 for the processing and analysis of sequencing data generated by Illumina's next-generation sequencing platforms. -RTA v1.18.66.3 to perform image analysis and base calling on HiSeq sequencing Illumina's instruments. -bcl2fastq v2.20.0.422 to convert bcl files to FASTQ.

-BCL Convert v3.6.3 to convert the Binary Base Call (BCL) files produced by Illumina™ sequencing systems to FASTQ files.
- Cutadapt v4.9 to remove unwanted sequences.
-SpaceRanger v1.3.0 to detect Dual Index Kit TS Set A with spaceranger mkfastq
-Rhapsody analysis pipeline v1.9.1 for the processing and analysis of sequencing data generated by the Rhapsody BD system.

R packages:
-limma v3.32.2 and EdgeR v3.20.1 for processing of count data and differential gene expression analysis
-Batchelor (1.20.0) for single-cell batch correction
-RANN v.2.6.2-To find the k nearest neighbours
- SingleR v2.8.0 for cell annotation using the ImmGen database
-Monocle3 v.1.3.7 for pseudotime and trajectory inference
-SPOTlight v1.0.3 for deconvolution of spatial transcriptomic data using seeded NMF regression
-decoupleR v2.8.0 for gene signature enrichment scoring
- Signac 1.14.0 for single-cell ATAC-seq analysis
-chromVAR v1.28.0 for transcription factor motif deviation analysis
-FlowSOM, and MASS v7.3.61 & 7.3.64, graphics v4.4.3, stats v4.0.3 & v4.4.3., and vegas v2.1.4 for additional statistical and graphical analysis
-Igraph (2.1.4) for Network Analysis and Visualization.
-RSEM v1.3.1 to extract reference transcripts from a genome.
- DESeq2 v1.30.1 to perform differential gene expression analysis based on the negative binomial distribution
- TCGAbiolinks v2.34.1 for accessing, analyzing, and integrating data from The Cancer Genome Atlas (TCGA)
-GenomicRanges v1.58.0 to define general purpose containers for storing and manipulating genomic intervals and variables defined along a genome
-MACS2 v2.2.9.1 for Model-Based Analysis for ChIP-Seq data
-JASPAR2020 v.99.10 a database of curated, non-redundant transcription factor (TF)-binding profiles stored as position frequency matrices (PFMs) for TFs across multiple species in six taxonomic groups.
-chromVAR v1.28.0 to determine variation in chromatin accessibility across sets of annotations or peaks.
-celldex v1.14.0 a collection of reference cell type expression datasets for single-cell and bulk RNA-seq data analysis.
-concaveman v1.1.0 to compute the concave polygon for one set of points.
-h5ad2sce v0.0.1
-scuttle v1.16.0, msigdbr v7.5.1
-AUCell v1.28.0 AUCell to identify cells with active gene sets
-BSgenome.Mmusculus.UCSC.mm10 v1.4.3 Full genome sequences for Mus musculus (Mouse) as provided by UCSC

Python libraries:
-TBin2cell v0.3.2
-pandas v2.2.3
-velocyto v0.17.17 for estimating RNA velocity in single-cell RNA sequencing data.

For manuscripts utilizing custom algorithms or software that are central to the research but not yet described in published literature, software must be made available to editors and reviewers. We strongly encourage code deposition in a community repository (e.g. GitHub). See the Nature Portfolio guidelines for submitting code & software for further information.

Data

Policy information about availability of data

All manuscripts must include a data availability statement. This statement should provide the following information, where applicable:

- Accession codes, unique identifiers, or web links for publicly available datasets
- A description of any restrictions on data availability
- For clinical datasets or third party data, please ensure that the statement adheres to our policy

Processed data and interactive visualization of the NeuMAP atlas are accessible through the scDAVIS (Single-Cell Data Analysis and VISualization) platform at: https://bioinfo.cnic.es/scdavisr/

Data that support the findings of the present manuscript are available from the corresponding authors upon reasonable request. All the omics data used for the mNeuMap is available at Gene Expression Omnibus (GEO) as a Super-series GSE266680.

Data used for the hNeuMap is available at the Chinese Academy of Sciences, with accession number HRA013413.

For spatial transcriptomic of mouse PDAC and MI, we used a publicly available dataset GSE141017and GSE176092, respectively.

Research involving human participants, their data, or biological material

Policy information about studies with human participants or human data. See also policy information about sex, gender (identity/presentation), and sexual orientation and race, ethnicity and racism.

Reporting on sex and gender	sex or gender-specific analyses were not conducted for these datasets.
Reporting on race, ethnicity, or other socially relevant groupings	All samples were de-identified prior to analysis, and no clinical or demographic identifiers were used in downstream research. N/A

Population characteristics	Formalin-fixed paraffin-embedded (FFPE) samples were collected from eight patients diagnosed with pulmonary invasive adenocarcinoma. Tissue microarrays (TMAs) were generated by a certified pathologist based on intratumoural neutrophil abundance. Bone marrow samples were obtained from healthy adult donors following written informed consent. All procedures were approved by the ethics committee of the University Hospital Tübingen. Human participants were not compensated. Samples were anonymized prior to processing, and no identifiable information was retained. Samples used to generate the human NeuMap come from healthy individuals or from anonymous acute-death donors without chronic inflammation. Additionally, SLE patient samples (umbilical cord/peripheral blood) come from pregnant patients with an active disease state (SLEPDAI >5) and without other chronic inflammatory comorbidities.
Recruitment	Tumor specimens were obtained from our institutional biobank, which prospectively accrues samples from all eligible patients under approved protocols. For this study, a small subset of cases was randomly selected from the biobank. Because the biobank aims to systematically include all patients, no self-selection or recruitment bias is expected, and results are unlikely to be affected by sampling bias. Human bone marrow cells were obtained from healthy, anonymous adult donors. Human samples were collected from Renji Hospital, Shanghai, China. Healthy donor samples (bone marrow, peripheral blood, umbilical cord blood) were randomly collected without self-selection or recruitment bias. Other healthy tissues were obtained from anonymous acute-death donors without chronic inflammation to minimize the confounding effects of death shock on the organs. SLE patient samples (umbilical cord/peripheral blood) were randomly selected from pregnant patients with an active disease state (SLEPDAI >5) and without other chronic inflammatory co-morbidities.
Ethics oversight	Human tissue microarray (TMA) samples were used under protocol #2019-5253, which was reviewed and approved by the McGill University Health Centre (MUHC) Research Ethics Board, specifically by the MUHC co-Chair of the Comité d'éthique de la recherche du CTGQ panel. Human lung tissue specimens were obtained through protocols approved by the McGill University Health Centre Institutional Review Board (IRB #2014-1119). Bone marrow samples were obtained from healthy adult donors following written informed consent. All procedures were approved by the ethics committee of the University Hospital Tübingen. Human samples were collected from Renji Hospital, Shanghai, China, with ethical approval (Renji Hospital Ethics Committee Protocol KY2024-090-B) and in accordance with the Declaration of Helsinki, following informed consent from all participants.

Note that full information on the approval of the study protocol must also be provided in the manuscript.

Field-specific reporting

Please select the one below that is the best fit for your research. If you are not sure, read the appropriate sections before making your selection.

☒ Life sciences ☐ Behavioural & social sciences ☐ Ecological, evolutionary & environmental sciences

For a reference copy of the document with all sections, see nature.com/documents/nr-reporting-summary-flat.pdf

Life sciences study design

All studies must disclose on these points even when the disclosure is negative.

Sample size	For each experiment, a sample size was chosen to obtain sufficient number of experiments and samples to calculate statistical significance. No statistical test was performed to predetermine sample size.They were determined on pilot experiments or prior experience.
Data exclusions	No collected data were excluded from the analysis.
Replication	Data presented were replicated in at least 3 independent experiments
Randomization	Allocation to samples or mice to the experimental groups was random.
Blinding	Due to practical constraints, investigators were not blinded to treatment administration during in vivo mouse experiments. However, all subsequent analyses were performed on samples labeled with anonymized ID codes that did not reveal treatment group, ensuring blinding during data analysis. Mice were randomly assigned to treatment groups. Data collection for automated experiments (e.g., flow cytometry, sequencing) was conducted using standardized protocols, and data interpretation was guided by appropriate experimental controls.

Reporting for specific materials, systems and methods

We require information from authors about some types of materials, experimental systems and methods used in many studies. Here, indicate whether each material, system or method listed is relevant to your study. If you are not sure if a list item applies to your research, read the appropriate section before selecting a response.

Materials & experimental systems

n/a	Involved in the study	
☐	☒	Antibodies
☐	☒	Eukaryotic cell lines
☒	☐	Palaeontology and archaeology
☐	☒	Animals and other organisms
☒	☐	Clinical data
☒	☐	Dual use research of concern
☒	☐	Plants

Methods

n/a	Involved in the study	
☒	☐	ChIP-seq
☐	☒	Flow cytometry
☒	☐	MRI-based neuroimaging

Antibodies

Antibodies used

Species |Antibody |Supplier |Cat |Clone |Lot |Dilution
Human |CD19-PE-CY7 |Biolegend |302216 |HIB19 |B368441 |1:200
Human |CD3-PE-CY7 |Biolegend |300316 |HIT3a |B368934 |1:200
Human |CD45-APC-CY7 |Biolegend |304014 |HI30 |B355047 |1:200
Human |CD56 PE-CY7 |Biolegend |362510 |5.1H11 |B369452 |1:200
Mouse |CCR5-BUV615-P |BD Biosciences |752321 |C34-3448 |5023291 |1:200
Mouse |CD101-PE-Cy7 |eBioscience |25-1011-82 |MOUSHI 101 |3023969 |1:200
Mouse |CD106-BUV563 |BD Biosciences |741246 |429 |5199058 |1:200
Mouse |CD115-BUV737 |BD Biosciences |750948 |AFS98 |4096153 |1:200
Mouse |CD11b-APC |Miltenyi Biotec |130-113-239 |M1/70.15.11.5 |5250304726 |1:50
Mouse |CD11b-BV510 |Biolegend |101263 |M1/70 |B448781 |1:200
Mouse |CD11b-PE |Biolegend |101208 |M1/70 |B338668 |1:200
Mouse |CD14-APC-Cy7 |Biolegend |123318 |Sa14-2 |B422513 |1:200
Mouse |CD14-PE |Biolegend |150106 |Sa14-2 |B339202 |1:50
Mouse |CD150-PE-Cy5 |Biolegend |115911 |TC15-12F12.2 |B448511 |1:200
Mouse |CD16/32-PerCP-Cy5.5 |Biolegend |101324 |93 |B465412 |1:200
Mouse |CD274-BV421 |Biolegend |124315 |10F-9G2 |B447175 |1:200
Mouse |CD44-BV570 |Biolegend |103037 |IM7 |B446242 |1:200
Mouse |CD45-APC |Biolegend |103112 |30F11 |B417515 |1:200
Mouse |CD45-FITC |Miltenyi Biotec |130-110-658 |REA737 |5241106535 |1:50
Mouse |CD74-BUV661 |BD Biosciences |741572 |In-1 |5034863 |1:200
Mouse |cKit-BV605 |Biolegend |135121 |ACK2 |B430106 |1:200
Mouse |Cx3Cr1-FITC |Biolegend |149020 |SA011F11 |B464771 |1:200
Mouse |CXCR2-PE |Biolegend |149303 |SA044G4 |B374879 |1:50
Mouse |DC-Trail-R1 biotinylated |R&D Systems |BAF2378 |Polyclonal |UOS0124061 |1:200
Mouse |Goat anti-rabbit-FITC |Sigma-Aldrich |F9887 |Polyclonal |SLCN0577 |1:100
Mouse |I-A/I-E-BUV496 |BD Biosciences |750281 |M5/114.15.2 |4260638 |1:200
Mouse |ICAM1-PE-Dazzle 594 |Biolegend |1161130 |YN1/1.7.4 |B438642 |1:200
Mouse |Ly6C-BV711 |Biolegend |128037 |HK1.4 |B425511 |1:200
Mouse |Ly6C-PE |Miltenyi Biotec |130-111-916 |REA796 |5221102758 |1:50
Mouse |Ly6G-PE |Biolegend |127608 |1A8 |B360223 |1:200
Mouse |MHC-II-APC |Miltenyi Biotec |130-112-388 |REA813 |5221103758 |1:50
Mouse |PD-L1-APC |Biolegend |124312 |10F.9G2 |B277024 |1:50
Mouse |Podoplanin-PE |Biolegend |127408 |8.1.1 |B394979 |1:50
Mouse |Sca1-BUV395 |BD Biosciences |563990 |D7 |3319689 |1:200
Mouse |Streptavidin-BV650 |Biolegend |405231 | |2514174 |1:500
Mouse |TLR4-BV786 |BD Biosciences |741015 |MTS510 |5034859 |1:200

Validation

CD19-PE-CY7 302216 Validated for Human. Each lot of this antibody is quality control tested by immunofluorescent staining with flow cytometric analysis. Additional reported applications (for the relevant formats) include: immunohistochemical staining of acetone-fixed frozen tissue sections and blocking of B cell proliferation.
CD3-PE-CY7 300316 Validated for Human. Each lot of this antibody is quality control tested by immunofluorescent staining with flow cytometric analysis. Additional reported (for the relevant formats) applications include: immunohistochemical staining of acetone-fixed frozen sections, immunoprecipitation, and activation of T lymphocytes.
CD45-APC-CY7 304014 Validated for Human. Each lot of this antibody is quality control tested by immunofluorescent staining with flow cytometric analysis. Additional reported applications (for the relevant formats) include: immunohistochemical staining of acetone-fixed frozen tissue sections and formalin-fixed paraffin-embedded tissue sections, inhibition of CD45 functions, immunofluorescence, Western blotting, and spatial biology (IBEX).
CD56 PE-CY7 362510 Validated for Human. Each lot of this antibody is quality control tested by immunofluorescent staining with flow cytometric analysis.

CCR5-BUV615-P 752321 CD195 (CCR5) Monoclonal antibody specifically detects CD195 (CCR5) in Mouse samples. It is validated for Flow Cytometry.
CD101-PE-Cy7 25-1011-82 This Moushi101 antibody has been tested by flow cytometric analysis of mouse bone marrow cells.
CD106-BUV563 741246 This antibody was developed for use in flow cytometry. The production process underwent stringent testing and validation to assure that it generates a high-quality conjugate with consistent performance and specific binding activity. However, verification testing has not been performed on all conjugate lots.
CD115-BUV737 750948 This antibody was developed for use in flow cytometry. The production process underwent stringent testing and validation to assure that it generates a high-quality conjugate with consistent performance and specific binding activity. However, verification testing has not been performed on all conjugate lots.
CD11b-APC 130-113-239 Validated for mouse. Validated for Flow cytometry and MACSima Imaging Cyclic Staining,
CD11b-BV510 101263 Validated for mouse. Each lot of this antibody is quality control tested by immunofluorescent staining with flow cytometric analysis. Clone M1/70 has been verified for immunocytochemistry (ICC) and frozen immunohistochemistry (IHC-F).
CD11b-PE 101208 Validated for mouse. Each lot of this antibody is quality control tested by immunofluorescent staining with flow cytometric analysis. Clone M1/70 has been verified for immunocytochemistry (ICC) and frozen immunohistochemistry (IHC-F).
CD14-APC-Cy7 123318 Validated for mouse. Each lot of this antibody is quality control tested by immunofluorescent staining with flow cytometric analysis,
CD14-PE 150106 Validated for mouse. Each lot of this antibody is quality control tested by immunofluorescent staining with flow cytometric analysis,
CD150-PE-Cy5 115911 Validated for mouse. Each lot of this antibody is quality control tested by immunofluorescent staining with flow cytometric analysis. The TC15-12F12.2 antibody has been reported to enhance the production of IFN-? by Th1 cells stimulated through TCR. Additional reported applications (for the relevant formats) include: immunoprecipitaion, enhancing IFN-? production by Th1 cells when stimulated with CD31, and inhibiting CD3 induced T cell proliferation.
CD16/32-PerCP-Cy5.5 101324 Validated for mouse. Each lot of this antibody is quality control tested by immunofluorescent staining with flow cytometric analysis. The 93 mAb is specific to the common epitope of CD16/CD32. Additional reported applications (for the relevant formats) include: immunoprecipitation1 and blocking of Fc-mediated reactions in functional studies. It is useful for blocking non-specific binding of immunoglobulin to Fc receptors. For blocking of Fc receptors in flow cytometric analysis, pre-incubate the cells with purified anti-CD16/CD32 antibody (=1.0 µg per 106 cells in 100 µL volume) for 5-10 minutes on ice prior to immunostaining.
CD274-BV421 124315 Validated for mouse. Each lot of this antibody is quality control tested by immunofluorescent staining with flow cytometric analysis. Additional reported applications (for the relevant formats) include: immunofluorescence, blocking, and immunohistochemistry of acetone-fixed frozen sections.
CD44-BV570 103037 Validated for mouse. Each lot of this antibody is quality control tested by immunofluorescent staining with flow cytometric analysis. Clone IM7 has been reported to recognize an epitope common to alloantigens and all isoforms of CD44 that is located between amino acids 145 and 18620. This clone has been verified for immunocytochemistry (ICC) and frozen immunohistochemistry (IHC-F). Additional reported applications (for the relevant formats) include: immunohistochemistry of acetone-fixed frozen sections and formalin-fixed paraffin-embedded sections, complement-mediated cytotoxicity, immunoprecipitation, in vivo inhibition of DTH, and spatial biology (IBEX).
CD45-APC 103112 Validated for mouse. Each lot of this antibody is quality control tested by immunofluorescent staining with flow cytometric analysis. Additional reported applications (for relevant formats) include: immunoprecipitation, complement-dependent cytotoxicity, immunohistochemistry (acetone-fixed frozen sections, zinc-fixed paraffin-embedded sections and formalin-fixed paraffin-embedded sections), Western blotting, and spatial biology (IBEX)
CD45-FITC 130-110-658 Validated for mouse. Validated for Flow cytometry, MACSima Imaging Cyclic Staining, and 3D immunofluorescence.
CD74-BUV661 741572 Validated for mouse. Each lot of this antibody is quality control tested by immunofluorescent staining with flow cytometric analysis,
cKit-BV605 135121 Validated for mouse. Each lot of this antibody is quality control tested by immunofluorescent staining with flow cytometric analysis. ACK2 has been reported to block c-Kit function. The LEAF™ purified antibody (Endotoxin <0.1 EU/µg, Azide-Free, 0.2 µm filtered) is recommended for functional assays (Cat. No. 135103).
Cx3Cr1-FITC 149020 Validated for mouse. Each lot of this antibody is quality control tested by immunofluorescent staining with flow cytometric analysis
CXCR2-PE 149303 Validated for mouse. Each lot of this antibody is quality control tested by immunofluorescent staining with flow cytometric analysis.
DC-Trail-R1 biotinylated BAF2378 Detects mouse DcTRAIL R1/TNFRSF23 in Western blots. In Western blots, approximately 25% cross-reactivity with recombinant mouse (rm) DcTRAIL R2 is observed and less than 1% cross-reactivity with rmTRAIL R2, recombinant human (rh) TRAIL R3, and rhTRAIL R4 is observed.
Goat anti-rabbit-FITC F9887 Anti-Rabbit IgG (whole molecule)-FITC antibody produced in goat has been used in immunohistochemistry and indirect immunofluorescence.
I-A/I-E-BUV496 750281 Validated for mouse. This antibody was developed for use in flow cytometry. The production process underwent stringent testing and validation to assure that it generates a high-quality conjugate with consistent performance and specific binding activity. However, verification testing has not been performed on all conjugate lots.
ICAM1-PE-Dazzle 594 1161130 Validated for mouse. Each lot of this antibody is quality control tested by immunofluorescent staining with flow cytometric analysis. Additional reported applications (for the relevant formats) include: in vitro and in vivo blocking of cell-cell adhesion and CD54 functions, immunohistochemical staining of acetone-fixed frozen sections, immunoprecipitation, and Western blotting (non-reducing).
Ly6C-BV711 128037 Validated for mouse. Each lot of this antibody is quality control tested by immunofluorescent staining with flow cytometric analysis. Additional reported applications (for relevant formats of this clone) include: in vitro activation of T cells and immunohistochemistry of frozen sections.
Ly6C-PE 130-111-916 Validated for mouse. Validated for Flow cytometry and MACSima Imaging Cyclic Staining.
Ly6G-PE 127608 Validated for mouse. Each lot of this antibody is quality control tested by immunofluorescent staining with flow cytometric analysis. Additional reported applications (for the relevant formats) include: immunohistochemistry of frozen sections and paraffin-embedded sections, depletion, and spatial biology (IBEX).
MHC-II-APC 130-112-388 Validated for mouse. Validated for Flow cytometry and MACSima Imaging Cyclic Staining.
PD-L1-APC 124312 Validated for mouse. Validated for Flow cytometry, immunofluorescence, blocking, and immunohistochemistry of acetone-fixed frozen sections.
Podoplanin-PE 127408 Validated for mouse. Each lot of this antibody is quality control tested by immunofluorescent staining with flow cytometric analysis. Additional reported applications (for the relevant formats) include: immunohistochemistry, and spatial biology (IBEX).

Sca1-BUV395 563990 Validated for mouse. Flow cytometry Routinely Tested.
Streptavidin-BV650 405231 Each lot of this Streptavidin-Brilliant Violet 650™ is quality control tested by immunofluorescent staining with flow cytometric analysis.
TLR4-BV786 741015 Validated for mouse. This antibody was developed for use in flow cytometry. The production process underwent stringent testing and validation to assure that it generates a high-quality conjugate with consistent performance and specific binding activity. However, verification testing has not been performed on all conjugate lots.

Eukaryotic cell lines

Policy information about cell lines and Sex and Gender in Research

Cell line source(s)

The C57BL/6J-derived Lewis Lung Carcinoma (LLC), E0771 (luminal B breast cancer), and BALB/c-derived 4T1 (triple-negative breast cancer) cell lines were obtained from the American Type Culture Collection (ATCC). The FC1242 pancreatic adenocarcinoma cell line was a kind gift from Dr. Dannielle Engle (Tuveson Lab, Cold Spring Harbor Laboratory) and was originally derived from Pdx1-Cre; Kras^G12D/+; p53^null/+ (KPC) mice. B16-OVA cells were provided by D. Sancho Lab, (CNIC, Madrid, Spain)(doi:10.1158/2159-8290.CD-15-0510). HoxB8-immortalized myeloid progenitor cells were used for in vitro differentiation studies. CRISPR–Cas9-mediated knockout of selected transcription factors in HoxB8 progenitors was performed as previously described (doi: 10.1038/s41590-021-00968-4).

Authentication

HoxB8 were validated by morphology and surface marker phenotype. Lewis Lung Carcinoma (LLC), E0771 (luminal B breast cancer), and BALB/c-derived 4T1 (triple-negative breast cancer) were authenticated using GenePrint 10 Loci Service. The FC1242 pancreatic adenocarcinoma and B16-OVA melanoma cell lines were not further verified.

Mycoplasma contamination

All the cell lines were routinely tested for mycoplasma contamination by qPCR. All the results were always negative.

Commonly misidentified lines
(See ICLAC register)

No commonly misidentified cell lines were used in the study

Animals and other research organisms

Policy information about studies involving animals; ARRIVE guidelines recommended for reporting animal research, and Sex and Gender in Research

Laboratory animals

All experiments were performed in male and female C57BL/6 mice aged 6–24 weeks. Young mice were defined as 8–12 weeks old, and old mice as 22–24 months at the time of analysis. Mice were maintained under specific pathogen-free conditions with chow and water provided ad libitum. mouse lines used were on the C57B1/6J background and housed under specific pathogen-free conditions at the CNIC, SigN or Yale University. All mouse husbandry and experimentation was conducted using protocols approved by local animal ethics committees and authorities. Mice (mus musculus) were mantained in racks with individual ventilation cages according to current Spanish, Singapore and US legislation (RD 53/2013 and EU Directive 63/2010, respectively). Rodents have a dust/ pathogen-free bedding, sufficient nesting and environmental enrichment material for the development of species-specific behavior. All the animals have food and water "ad libitum" in environmental conditions of 45-65% of relative humidity, temperature of 21-24C and a light/ dark cycle of 12:12 hours. In addition and in order to preserve animal welfare, an animal health surveillance program is applied for health monitoring, which follows FELASA recommendations for Specific Pathogen Free facilities. All mice strains used are listed below and in the Mice section of the Methods.

Neutrophil-specific Tgfbr2-deficient mice (TGFβR ΔN) were generated by crossing MRP8 CRE mice with Tgfbr2 fl/fl mice. Similarly, Junbfl/fl, Csf2rfl/fl, and Ifnar1fl/fl mice were crossed with MRP8CRE to generate neutrophil-specific knockouts. Apoe–/– mice (B6.129P2-Apoe tm1Unc, Taconic M&B) were used in atherosclerosis models.

Ly6GCREERT2 mice were crossed with Rosa26tdTomato reporter mice to generate iLy6G tdTom mice for fate-mapping experiments. JAXBoy mice (Ptprc K302E) from Jackson Laboratories and Tet2–/– mice were used for adoptive bone marrow transfer experiments. Germ-free male C57BL/6 mice (8 weeks old) were kindly provided by Noah Palm's lab (Yale University) for microbiota-dependent studies.

For rewilding experiments, litters from multiple breeding pairs were randomly assigned to remain in the institutional vivarium (laboratory group) or released into controlled outdoor enclosures (rewilded group) to ensure microbiota equivalence at baseline.

Wild animals

No wild animals were used in these studies

Reporting on sex

For all single-cell sequencing experiments, the sex of the animals used is explicitly reported in the main text. Where applicable, computational analyses were performed to assess potential sex-biased differences in gene expression and cellular composition. For all other in vivo experiments, both male and female mice were included, and data from both sexes were pooled and analyzed together unless otherwise specified.

Field-collected samples

For the rewilding experiments, litters of mice were generated from multiple breeding pairs and randomly assigned to either remain in the institutional vivarium (laboratory mice) or be released into the outdoor enclosures (rewilded mice) to control for the microbiota at the onset of the experiment.

Ethics oversight

All protocols were reviewed and approved by the corresponding local authorities of Madrid, Singapore, Rutgers, Princeton, and Yale University. The protocols for releasing laboratory mice into the outdoor enclosure facility and then returning them to vivaria were approved by Princeton University (protocol #1982) and Rutgers University (protocol # PROTO999900794).

Note that full information on the approval of the study protocol must also be provided in the manuscript.

Plants

Seed stocks

Report on the source of all seed stocks or other plant material used. If applicable, state the seed stock centre and catalogue number. If plant specimens were collected from the field, describe the collection location, date and sampling procedures.

Novel plant genotypes

Describe the methods by which all novel plant genotypes were produced. This includes those generated by transgenic approaches, gene editing, chemical/radiation-based mutagenesis and hybridization. For transgenic lines, describe the transformation method, the number of independent lines analyzed and the generation upon which experiments were performed. For gene-edited lines, describe the editor used, the endogenous sequence targeted for editing, the targeting guide RNA sequence (if applicable) and how the editor was applied.

Authentication

Describe any authentication procedures for each seed stock used or novel genotype generated. Describe any experiments used to assess the effect of a mutation and, where applicable, how potential secondary effects (e.g. second site T-DNA insertions, mosiacism, off-target gene editing) were examined.

Flow Cytometry

Plots

Confirm that:

☒ The axis labels state the marker and fluorochrome used (e.g. CD4-FITC).

☒ The axis scales are clearly visible. Include numbers along axes only for bottom left plot of group (a 'group' is an analysis of identical markers).

☒ All plots are contour plots with outliers or pseudocolor plots.

☒ A numerical value for number of cells or percentage (with statistics) is provided.

Methodology

Sample preparation

Mice
Mice were euthanized, and blood was collected via cardiac puncture using a 1 mL syringe with a 26-gauge needle preloaded with 50 µL of 0.5 M EDTA. After blood collection, mice were perfused via the right ventricle with 10 mL PBS to flush circulating cells. Tissues (lung, tumors, muscle, heart, placenta, pancreas) were minced and digested with Liberase TM (Sigma) and DNase I (Sigma) at 37°C for 30 minutes. Digests were filtered through 70 µm nylon mesh sieves using syringe plungers to obtain single-cell suspensions.

Bone marrow was flushed from femurs using PBS with 2 mM EDTA and 2% FBS. Spleens were mechanically dissociated through 70 µm filters. Colon tissues were cleaned and incubated in 100 mM EDTA for 30 minutes at 37°C to remove epithelium, then enzymatically digested as above. Ear skin was separated into dorsal and ventral layers, chopped, and digested for 90 minutes at 37°C. For peritoneal lavage, 10 mL of cold PBS was injected into the cavity, followed by gentle massage and aspiration.

Meninges were isolated post-mortem by removing the brain and peeling the dura with fine forceps. Brain infarct tissue was dissected, digested with a cocktail (collagenase, dispase, TLCK, DNase I), ground in a glass-glass grinder, and filtered through 70 µm mesh. Leukocytes were isolated via 35% Percoll density centrifugation. All single-cell suspensions were treated with RBC lysis buffer (eBioscience), washed, and stained with antibody cocktails.

Primary Neutrophils and HoxB8 Cell Cultures
Primary mouse neutrophils were obtained from the femurs and tibias of C57BL/6J mice or relevant genetically modified strains. Bone marrow was centrifuged and erythrocytes were lysed using Red Blood Cell Lysis Solution (Qiagen, 79217). Cells were filtered and sorted on a BD Aria Cell Sorter into mature (DAPI$^-$ CD45$^+$ CD11b$^+$ Ly6G$^+$ CD101$^+$) and immature (DAPI$^-$ CD45$^+$ CD11b$^+$ Ly6G$^+$ CD101$^-$) neutrophils. Sorted cells were seeded into 96-well plates (50,000 cells/well) in complete DMEM and cultured under vehicle or treatment conditions.

HoxB8-immortalized myeloid progenitors were routinely screened for mycoplasma and cultured in RPMI 1640 supplemented with 10% fetal calf serum (FCS), 10 µM β-mercaptoethanol, 4% SCF-producing CHO cell supernatant, 1% penicillin/streptomycin, and 1 µM β-estradiol to maintain the progenitor state. Neutrophil differentiation was induced by β-estradiol withdrawal and continued in media with 4% SCF and 20 ng/mL G-CSF.

Human samples were collected in Renji Hospital, Shanghai, China, under the Renji Hospital Ethics Committee protocol KY2024-090-B, in accordance with the Declaration of Helsinki. Samples were collected from healthy donors, patients or perfused organ donors. Blood and bone marrow were collected in BD vacutainer K2E (EDTA) tubes (BD Healthcare, 367525) to prevent coagulation. Erythrocytes were lysed in 5-10 ml 1x red blood cells (RBC) lysis buffer (diluted from 10x BD Pharm Lyse, 555899) for 5 min for twice to deplete erythrocytes and then washed and re-suspension. Spleen, lung, omentum, mesentary fat, perirenal fat, liver, colon and rectum tissues were minced into small pieces and digested for 30 min at 37 ℃ in a mixture of collagenase IV (385U ml-1, Sigma) and DNaseI (2.5mg ml-1, Sigma) and the samples were homogenized into single-cell suspension using syringe plungers and passed through 70 µm cell strainers (15-1070, BIOLOGIX). Then the samples were lysed in 2 ml 1x RBC lysis buffer (diluted from 10x BD Pharm Lyse, 555899) for 3 min to deplete erythrocytes and then washed and resuspended. Endometrium was cut into small pieces and enzymatically digested with the Tumor Dissociation Kit (130-095-929, Miltenyi Biotec). After digestion, the cell suspension was filtered through 70 µm cell strainers and subjected to a 3-min erythrocyte lysis with 2 ml 1x RBC lysis buffer, followed by washing and re-suspension.All single-cell suspensions were

	incubated with Fc-blocker (Human TruStain FcXTM, 422302, Biolegend) for 30 min on ice, then stained for 30 min at 4 ℃ in the dark with Fixable Viability Stain 700 (564997, BD Biosciences) (1:1000), CD45 APC-CY7 (304014,Biolegend) (1:200), CD3 PE-CY7 (300316, Biolegend) (1:200), CD19 PE-CY7 (302216, Biolegend) (1:200) or CD56 PE-CY7 (362510, Biolegend) (1:200). After washing with FACS buffer, cells were sorted on a FACSAria III cell sorter (BD Biosciences).
Instrument	Samples were acquired on a BD Symphony A4 Flow Cytometer
Software	Data were analyzed with FlowJo software (BD). FlowAI (DOI: 10.1093/bioinformatics/btw191) was used for quality control. Dimensionality reduction was performed using the UMAP_R plugin. Clustering was conducted using FlowSOM and ClusterExplorer. UMAP parameters were embedded per sample to enable statistical comparisons of neutrophil phenotypes.
Cell population abundance	Typical post-sorting purity >98%
Gating strategy	Neutrophils were sorted as live (DAPI-negative), CD11b$^+$ Ly6G$^+$ cells using a FACS Aria sorter (BD Biosciences) at the CNIC Cytometry Unit. Bone marrow neutrophils were capture as Lineage negative (B220, CD18, NK.1.1, Ter119, CD3). Human leukocytes were sorted as CD45+CD3-CD19-CD56- cells

☒ Tick this box to confirm that a figure exemplifying the gating strategy is provided in the Supplementary Information.

Signed by BALLESTEROS MARTIN, IVAN JOSE (FIRMA) date 09/10/2025 certified by AC DNIE 004